UNIQUE GLASS FORMATION AND MECHANICAL PROPERTIES OF ZR-CU-BASED ALLOYS

WU WENFEI
(M. Eng, TsingHua Univ.)

A THESIS SUBMITTED

FOR THE DEGREE OF DOCTOR OF PHILOSOPHY

DEPARTMENT OF MATERIALS SCIENCE & ENGINEERING

NATIONAL UNIVERSITY OF SINGAPORE

2008

Acknowledgments

First of all, I would like to thank my supervisor, Associate Professor Yi Li. I would not be able to come to Singapore if Professor Li had not offered me the opportunity to further my study in NUS in the summer of 2004. He is a truly excellent teacher, dedicated scientist, and supportive person. I have received invaluable technical advice and constant encouragement from him, all of which have been essential to the completion of my Ph.D. project. His open and scholarly mind has made it possible for me to enjoy more or less independent research. With the past 4 years of working with him, I have been enlightened to be more analytic, logic and rational. I feel deeply indebted to him and would like to express my sincere gratitude to him.

I am grateful to Professor Christ A. Schuh in Massachusetts Institute of Technology, United States, for his precious discussion during the collaborative work presented in Chapter 3 and his valuable suggestions for the work presented in Chapter 5. His erudition, insights, and professional attitude have left me with a great impression. I would also like to thank Professor YongWei Zhang, and his student Dr. ChunYu Zhang in NUS, for

their fruitful discussion, suggestions and all the effort during the collaborative work presented in Chapter 4. I am grateful to Professor KaiYang Zeng in NUS, for valuable discussions on many issues of the mechanical testing.

I am indebted to the dedicated staff members in the Department of Materials Science & Engineering for their constant help in various ways, and the National University of Singapore for financial support.

To the group members of the Non-Equilibrium Materials Lab, former seniors Dr. Dong Ma, Dr. Shirley Meng, Dr. Yong Zhang, Dr. Hui Zi Kong, Dr. Hao Tan, Dr. Irene Lee, Dong Wang, Dr. Jie Zhang, Dr. XiaoLing Fu, CuiYang Wang, Dr. XiaoQiang Zhang, Kai Yang Lim, and the present collegues Dr. Hai Yang, Grace Lim, Zheng Han, Xiang Li, Qiang Guo, and Dr. ZhiYu Wang, I extend my very sincere thanks. The experience of working together with these talented guys was a wonderful memory in my life.

It is my great pleasure to acknowledge my friends in Singapore: Professor JunMin Xue, Jian He, Hua Ma, ZhongQiao Hu, HongYu Liu, YouSheng Zhang, Jian Zhang, Thongmee Sirikanjana and GuangXia Hu. I have enjoyed the great time that we have spent together.

Last but not least, I am deeply indebted to my family (my parents, younger sister and girlfriend) for their great love and understanding. Without their constant support I would not have had the strength to reach this stage.

August 2008 in Singapore, Wen Fei WU

Table of Contents

Summary

The research area of amorphous metals was replenished recently with the discovery of bulk-sized metallic glasses (BMGs) in various systems in the past decades. In this research field, the formation and mechanical behavior of BMGs are the two major sub-areas, which were the focuses of the present work.

The first significant finding of this work is the discovery of bulk Zr-Cu "intermetallic glass", which is a new group of glass formed in the vicinity of intermetallics of the phase diagram by rapid quenching. This finding is remarkable because in the conventional belief, metallic glass is either formed near deep-eutectics through liquid quenching or near the centre of phase diagram by solid-state reaction. This discovery is believed to open an otherwise overlooked arena for finding a new host of metallic glasses.

Upon mechanical loading, metallic glasses generally fail catastrophically by one dominant shear band with very limited plastic strain, similar to those of typical brittle materials. In view of this brittle fracture, to address the flaw sensitivity issue in BMGs thus becomes essential. The second

contribution of this work is to investigate systematically the strength variation of BMGs by applying Weibull statistics. The results showed surprisingly high Weibull moduli approaching the range for crystalline metals, despite their brittleness. These high Weibull moduli of the BMGs indicate that these materials are highly uniform in strength, and thus much more mechanically reliable than expected in light of their flaw sensitivity. Such reliability is encouraging for the potential use of BMGs as an engineering material.

The third part of this thesis is closely following the previous part. The high strength uniformity indicates that there is a small allowed variation range in stress for the shear band initiation. Therefore, if a large stress gradient could be introduced inside the sample, the propagation of shear band could be restricted, new shear bands might be encouraged to be formed, and thus the plasticity could be enhanced. We thus proposed a new concept - "stress gradient enhanced plasticity" - to alleviate the concern of catastrophic failure of monolithic BMG using non-orthogonal samples for illustration. It not only suggests that, the deformation of BMG could be much sensitive to the specimen geometry; but more importantly, it offers a new way to toughen the monolithic "brittle" glassy alloys with practical significance.

The fourth contribution of this thesis is to identify the existence of a "*malleable-to-brittle*" transition in BMG occurred at a critical sample size under both as-cast and annealed states. Contrary to the traditional view that the sample size dependence of malleability is attributed to free volume

differences, we proposed that this transition should be related to the geometrical size effect, which is later proven by the observation of such a transition even in the annealed BMG samples. In addition, a sample size dependence of strength accompanied with this transition was also identified. It is suggested that, to determine the critical sizes for the "malleable-to-brittle" transition in BMGs is extremely important and should provide valuable guidance for their component design.

List of Tables

List of Figures

List of Publication

1. **W. F. Wu**, Z. Han, and Y. Li. Size-dependent "malleable-to-brittle" transition in a bulk metallic glass. ***Applied Physics Letters,*** 2008, 93: 061908

2. **W. F. Wu**, C. Y. Zhang, Y. W. Zhang, K. Y. Zeng and Y. Li. Stress gradient enhanced plasticity in a monolithic bulk metallic glass. ***Intermetallics,*** 2008, 16: 1190

3. **W. F. Wu**, Y. Li. Geometry-sensitive plasticity of a monolithic bulk metallic glass. ***Mater. Res. Soc. Symp. Proc.,*** 2008, 1048: Z05-06

4. **W. F. Wu**, Y. Li and C. A. Schuh. Strength, plasticity and brittleness of bulk metallic glasses under compression: statistical and geometric effects. ***Philosophical Magazine,*** 2008, 88: 71

5. **W. F. Wu**, and Y. Li. Bulk "intermetallic glass" by rapid quenching. (Submitted)

6. Z. Han, **W. F. Wu**, Y. Li, Y. J. Wei and H. J. Gao. An instability index of shear band for plasticity in metallic glasses. ***Acta Materialia,*** 2009, 57: 1367

7. Z. Han, H. Yang, **W. F. Wu**, Y. Li. Invariant critical stress for shear banding in a bulk metallic glass. ***Applied Physics Letters,*** 2008, 93: 231912

Chapter 1

Introduction

Metallic Glass (MG) is a metal based amorphous solid. The research on MG has recently been revisited owing to the discovery of a number of bulk sized (i.e. ≥ 1 mm) MG samples, which are called "bulk metallic glasses" (BMGs). The BMGs are of great interest both in science and in engineering due to their superior properties such as high elastic limit, high strength, high toughness as well as high corrosion resistance [1]. They are very stable because of the large supercooled liquid region. Their superplastic behavior at elevated temperature makes them a good candidate for net shaping materials. They

have also been used as the material for fabricating golf club head, hand phone casing, and penetrators [2].

In the first chapter, a general introduction to BMGs will be given. The development, general properties and applications of BMGs will be briefly reviewed. After this, I will focus on the formation as well as the mechanical behavior of BMGs, which are the major concerns of this thesis, and the fundamental yet important knowledge such as Turnbull's kinetic theory on glass formation and Spaepen's deformation map of amorphous alloys will be reviewed in detail. The objectives for the current work will then be pointed out. The first chapter will end with an outline of the thesis.

1.1 Introduction to bulk metallic glasses (BMGs)

Metallic glasses are metals or metal alloys with no long range atomic order (LRO). They are prepared by rapid solidification of the alloying constituents from liquid phase. The solidification occurs so rapidly that the atoms are frozen in their liquid configuration (**Figure 1. 1**) [3].

The first metallic glass $Au_{75}Si_{25}$ was reported by Duwez [4] in 1960. He made this discovery by chilling metallic liquids at very high rates of 10^5-10^6 K/s. Using rapid solidification methods such as *splat quenching* and *melt*

spinning with characteristic cooling rates in the range of 10^3-10^6 K/s, metallic glasses were found in many binary and ternary alloy systems [3]. However, for a long time, the critical size for the known metallic glasses was in micron scale (usually < 0.2 mm), which has limited their use as engineering materials.

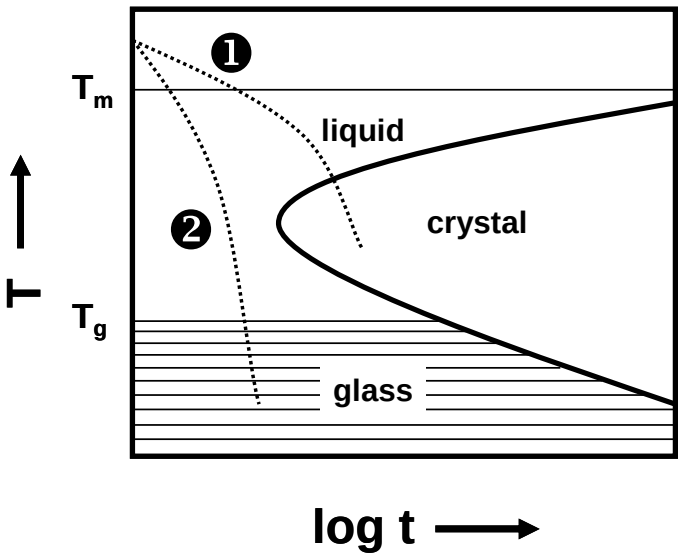

Figure 1. 1 Schematic diagram of glass formation by rapid quenching of a liquid without crystallization. Line 1 corresponds to crystallization at low cooling rate, and Line 2 corresponds to vitrification at high cooling rate.

In 1974, Chen [5] synthesized amorphous rods with diameter up to 3 mm among several ternary noble metal alloy systems such as Pd-Cu-Si and Pd-Ni-P by *water quenching* with cooling rates of 10^3 K/s or less. If one arbitrarily defines larger than 1 *mm* in the smallest dimension of the sample as "bulk", these ternary glasses were the first examples of "bulk" metallic glasses (BMGs) [1]. Till the late 1980s, Inoue and co-workers successfully

prepared the "first" BMG without noble metals $La_{55}Al_{25}Ni_{20}$ [6] by *copper mold casting*, which is the beginning of a new era for BMGs. Subsequently new BMGs have been discovered in many other systems such as Zr, Cu, Fe, Ni, Ti, Nd, Ca, Y, Ce, and Au based alloy systems [7-11]. To date, the largest critical size of the known BMGs is 72 mm for the $Pd_{40}Cu_{30}Ni_{10}P_{20}$ [12] alloy obtained by *fluxing method*. **Table 1. 1** summarizes the typical BMG systems with their critical sizes and the years in which they were first reported.

Table 1. 1 Typical BMG systems with their critical sizes and years in which they were developed.

BMG system	Year	Critical size *(mm)*	Ref.
Pd-(Cu, Ni)-Si	1974	3	[5]
(Pd, Pt)-Ni-P			
Pd–Ni–P	1982	10	[13]
La-Al-Ni	1990	3	[6]
Mg-Cu-Y	1991	4	[14]
Zr-Ti-Cu-Ni-Be	1993	>14	[15]
Zr-Al-Ni-Cu	1993	30	[16]
Ti-Zr-Cu-Ni	1995	4	[17]
Fe-Al-Ga-P-B-C	1995	1	[18]
Pd-Cu-Ni-P	1997	72	[12]
Nd-Al-(Fe, Co)	1997	15	[19]
Ti-Ni-Cu-Sn	1998	6	[20]
Ni-Nb-(Cr, Mo)-P-B	1999	1	[21]
Cu-(Zr, Hf)-Ti	2001	4	[22]
Fe-Cr-Mo-C-B-P	2002	3	[23]
Co-Fe-Ta-B	2003	2	[24]
Ni-Ti-Cu-Zr-Al	2004	5	[25]
Cu-Zr-Al-Y	2004	10	[26]
Cu-Zr	2004	2	[27-29]
Fe-Co-Cr-Mo-C-B-Y	2005	16	[30]
Ca-Mg-Ni	2005	13	[9]
Au-Ag-Pd-Cu-Si	2005	5	[10]
Mg-Cu-Ag-Gd	2005	25	[31]

Recently, the critical diameter D_c for glass formation (i.e., the maximum diameter of a rod that can be cast fully glassy) has exceeded 1 cm for a wider variety of alloy systems such as those based on Fe [32], Co [33], Ni [34] or Cu [35], resulting in significantly increased engineering importance for bulk metallic glasses (BMGs).

Table 1. 2 summarizes fields of application in which the bulk amorphous alloys have expected uses. Considering the recent significant extension of application fields, it is expected that the importance of bulk amorphous alloys as basic science and engineering materials will increase steadily in the 21st century.

Table 1. 2 Possible application fields for BMGs

Properties	Application field
High strength	Machinery structural materials
High hardness	Cutting materials
High fracture toughness	Die materials
High impact fracture energy	Tool materials
High fatigue strength	Bonding materials
High elastic energy	Sporting goods materials
High corrosion resistance	Corrosion resistance materials
High wear resistance	Writing appliance materials
High reflection ratio	Optical precision materials
High hydrogen storage	Hydrogen storage materials
Good soft magnetism	Soft magnetic materials
High frequency permeability	High magnetostrictive materials
Efficient electrode	Electrode materials
High viscous flowability	Composite materials
High acoustic attenuation	Acoustic absorption materials
Self-sharpening property	Penetrator
High wear resistance and manufacturability	Medical devices materials

The commercialization of BMG products has already succeeded [2] in the following areas: (1) tungsten-loaded composite BMGs [36] for defense applications such as armor and submunition components; (2) thinner forming technologies [37] for electronic casings such as mobile phones, handhelds (PDAs), and cameras; (3) medical devices such as reconstructive supports, surgical blades, fracture fixations, and spinal implants; and (4) fine jewelry such as watch casings, fountain pens, and finger rings.

1.2 Formation of BMGs

Understanding glass formation, particularly in multi-component systems, is a complex task involving multiple intertwined issues. Both qualitative and quantitative methods were developed during the past decades to analyze and predict glass-forming ability (GFA, expressed in terms of critical cooling rate) and glass-forming range (GFR, expressing the range of composition), and to search for new glass-formers. Typical considerations involve thermodynamic driving force for crystallization and kinetic constraints to prevent nucleation and/or growth of the competing crystalline phases.

1.2.1 Thermodynamics perspective

To avoid the crystallization, from thermodynamics consideration, it requires a low driving force for crystallization in the supercooled liquid to form a glass. The driving force for crystallization is the free-energy difference between the liquid state G_l and crystalline state G_s ($\Delta G_{l\text{-}s} = G_l - G_s$), which can be calculated by integrating the specific heat capacity difference $\Delta C_p^{l-s}(T)$ according to the Equation 1.1,

$$\Delta G_{l-s}(T) = \Delta H_f - \Delta S_f T - \int_T^{T_0} \Delta C_p^{l-s}(T)dT + T\int_T^{T_0} \frac{\Delta C_p^{l-s}(T)}{T} dT \qquad (1.1)$$

Where ΔH_f and ΔS_f are the enthalpy and entropy of fusion, respectively, at the temperature T_0, the temperature at which the crystal and the liquid are in equilibrium.

Based on the thermodynamic data, Busch et al. [38, 39] had systematically studied the thermodynamic functions of the typical bulk glass-forming undercooled liquid. **Figure 1. 2** shows the calculated Gibbs free energy of the supercooled liquid with respect to the crystal, $\Delta G(T)$, as a function of supercooling a selection of glass forming systems. The temperatures are normalized to the alloy melting temperatures. Qualitatively, the GFA, indicated by a low critical cooling rate, scales inversely with the driving force for crystallization, ΔG [40].

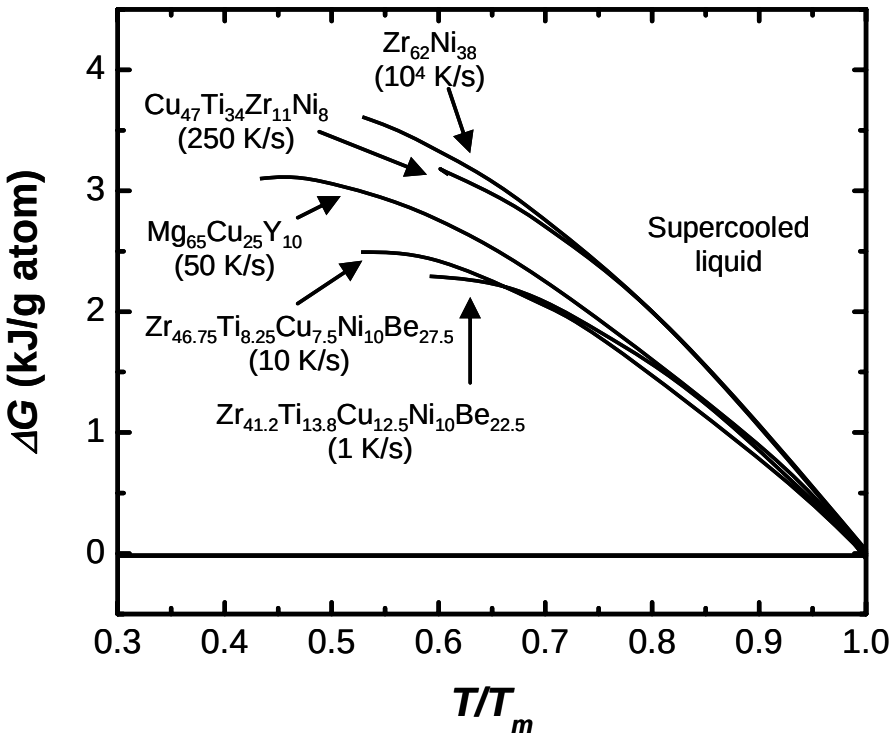

Figure 1. 2 Difference in Gibbs free energy between the liquid and the crystalline state for glass-forming liquids. The critical cooling rates for the alloys are indicated in the plot as K/s values beneath the composition labels, reproduced from [40].

1.2.2 Kinetics perspective

To better characterize the GFA of BMG systems, one needs to study the crystallization kinetics in these alloys. From the perspective of kinetics, the key parameter - *viscosity* has a significant influence on the GFA of an alloy system. A variety of techniques have been applied to measure viscosity from the equilibrium liquid down to the deeply undercooled liquid near T_g [41, 42].

Since the undercooled liquid alloys are relatively stable with respect to crystallization on laboratory time scales, viscosity can be measured in bulk glass-forming systems in much wider temperature and time scales than before. **Figure 1. 3** shows a "fragility plot" in the form proposed by Angell [43] in which the viscosities of different glass-forming liquids are compared in an Arrhenius plot for which the inverse temperature axis is normalized with respect to glass-transition temperature T_g. On this normalized scale, the melting point is at ~0.6. All the curves meet at 10^{12} Pa s, corresponding to the viscosity at T_g.

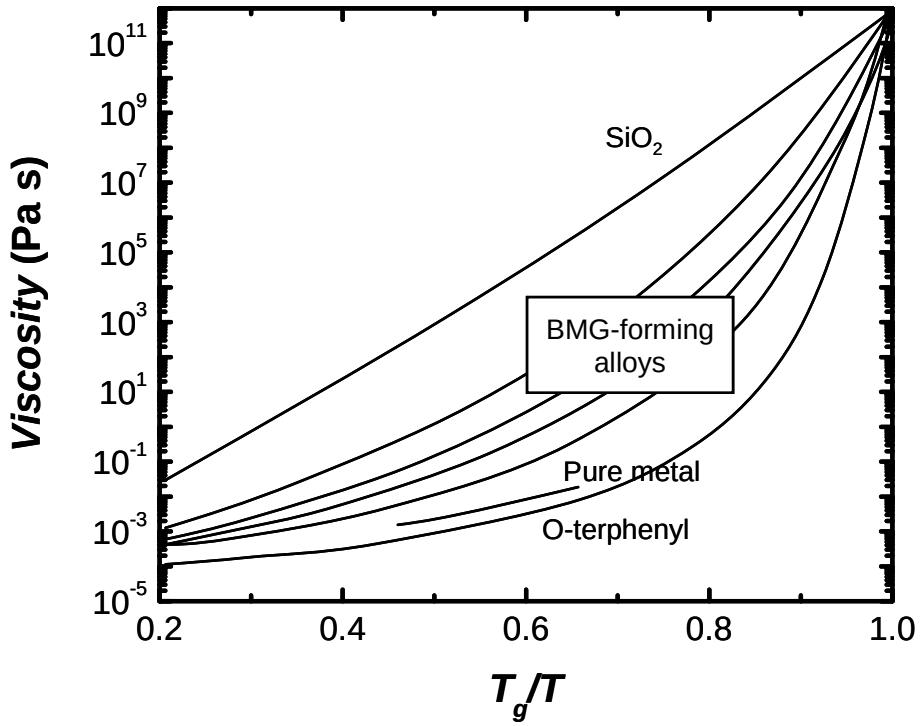

Figure 1. 3 Angell plot comparing the viscosities of different types of glass-forming liquids, reproduced from [43].

Two extreme cases are distinguished: kinetically "strong" liquids such as SiO_2 show near-Arrhenius behavior (straight line) [43] and have high viscosities. On the other hand, kinetically "fragile" liquids such as o-terphenyl exhibit a dramatic temperature-dependence of viscosity just above T_g and viscosities that are up to eight orders of magnitude lower than those of the strongest liquids [43]. Among typical BMG-forming alloys, the strongest have viscosities more than four orders of magnitude higher than the pure metals, which are kinetically very fragile and have liquid viscosities at the melting point of ~10^{-3} Pa s [44].

The strong liquid behavior is the single most important contribution to the high GFA of BMG-forming alloys, because it drastically retards crystal nucleation and especially growth kinetics [41, 45, 46].

1.2.3 Frequently used indicators and rules

Glass forming ability (GFA) can manifest itself by the critical cooling rate, R_C, for glass formation. However, only a few of these cooling rates had been reported so far and the measurements were usually not trivial [47-53]. The theoretical calculation approach for R_C proposed by Uhlmann [54] requires prior knowledge of a great number of parameters as well as information of

the viscosity over a wide temperature range, which are too difficult or impossible to obtain. To date, several GFA indicators have been proposed. In this section, they will be reviewed briefly.

1.2.3.1 T_{rg} criterion

It was generally known that if the melt can be quenched fast enough, avoiding nucleation, to a temperature below the glass transition temperature T_g, amorphous phase will be formed. If the heterogeneous nucleation is avoided, the minimum cooling rate for glass formation is determined by the homogeneous nucleation rate. Turnbull had used the classical nucleation theory to calculate the homogeneous nucleation rate in an undercooled melt [55]. He proposed that when the reduced glass transition temperature, T_{rg} (=T_g/T_l, T_l refers to the melting point of pure metal, or liquidus temperature of an alloy), was larger than 2/3, the homogeneous nucleation of crystals in the undercooled melt should become so sluggish that glass will be formed (**Figure 1. 4**). This is known as the Turnbull's T_{rg} criterion.

Subsequent work on the Au-Si, Pd-Si, and Pd-Cu-Si alloys confirmed this prediction [5]. This T_{rg} criterion for the suppression of nucleation in undercooled melts remains today one of the best "rules of thumb" for predicting the glass forming ability (GFA) of alloy systems. The significance of this criterion is that it implies that the good glass formers should be located around eutectic composition since generally T_{rg} value reaches maximum at the

eutectic point (**Figure 1. 5**).

Indeed it has been experimentally observed that high GFA usually appears around eutectics in many binary systems [3]. However, it cannot explain the observations over the years that in many systems the best glass formers are at off-eutectic compositions [32, 56, 57]. Moreover, the contribution from crystal growth to crystallization has not yet been considered in this rule.

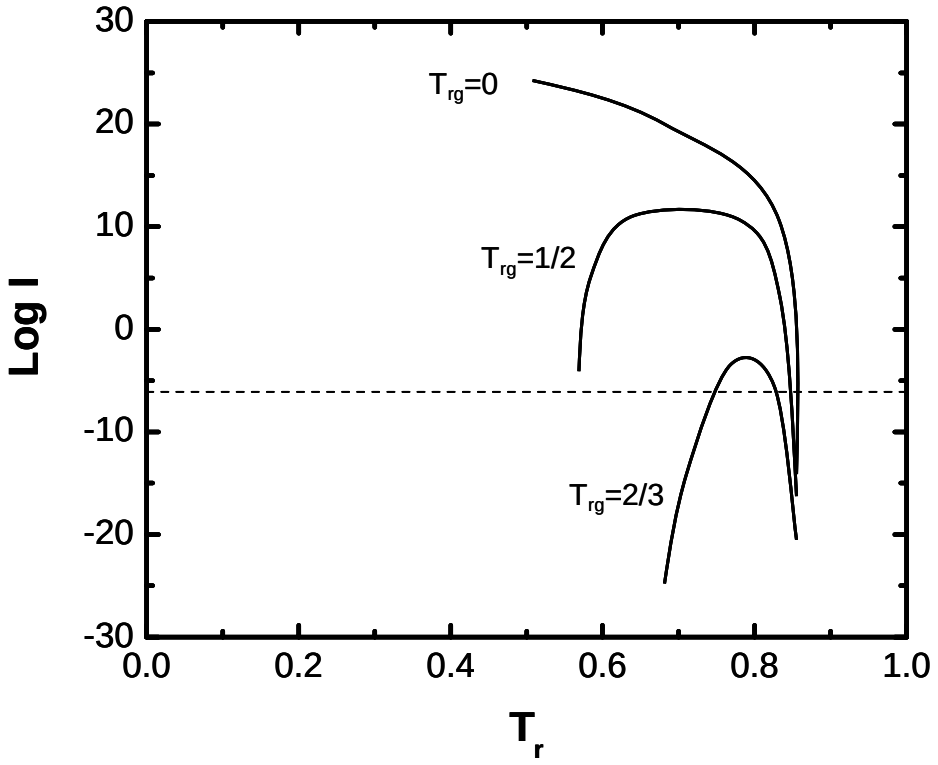

Figure 1. 4 Variation of logarithm of homogeneous nucleation rate I with reduced glass transition temperature T_r. $T_r=T/T_m$, $T_{rg}=T_g/T_m$. T, T_g, T_m are, respectively, the actual absolute temperature, the glass transition temperature, and the melting temperature of alloys, reproduced from [55].

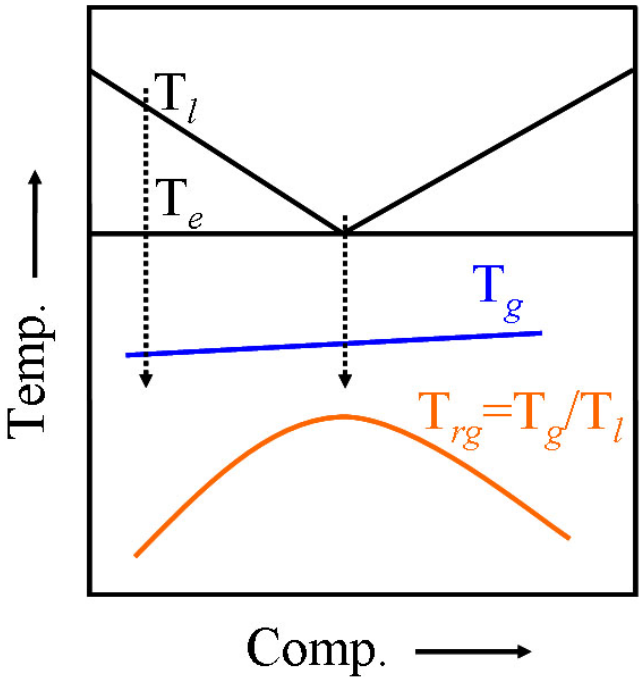

Figure 1. 5 Schematic diagram shows T_{rg} reaches maximum value around the eutectic point for a typical binary eutectic alloy phase diagram.

1.2.3.2 ΔT_x criterion

The ΔT_x criterion proposed by Inoue [7] indicates that good glass formers should exhibit a large supercooled liquid region ΔT_x, which is the difference between the onset crystallization temperature T_x and glass transition temperature T_g. For example, $Zr_{65}Al_{7.5}Ni_{10}Cu_{17.5}$ BMG with a large ΔT_x value of 127 K [58] was found to have a large critical size of 16 *mm* under water quenching [16].

Figure 1. 6 shows the GFA, which is evaluated by critical cooling rate R_c or critical size t_{max} (the smaller the R_c, the larger the t_{max}, and the better the GFA), as a function of ΔT_x for various types of metallic glasses. The linear

relationship between R_c and $\triangle T_x$ directly shows that the larger the $\triangle T_x$, the better the GFA. However, It does not provide a real description of GFA upon melt solidification, since T_x is obtained from calorimetric experiments of the glass and does not correspond to any specific cooling parameter [59].

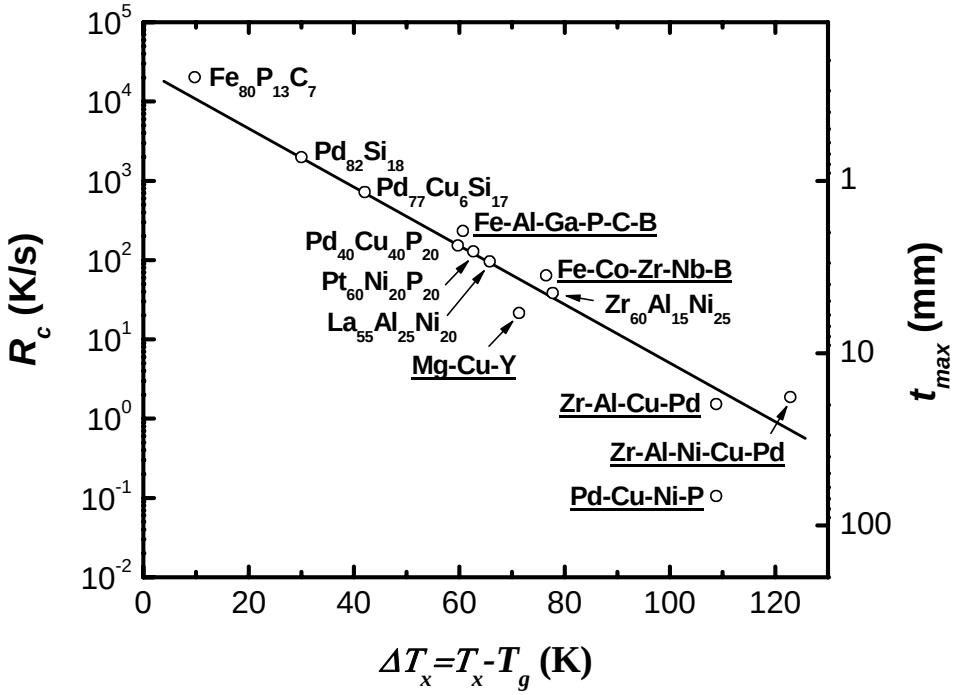

Figure 1. 6 Relationship between critical cooling rate R_c, critical size t_{max}, and the interval of supercooled liquid region $\triangle T_x$ for various BMGs, reproduced from [7].

1.2.3.3 Three empirical rules

Based on their works on the GFA of La-, Mg- and Zr-based BMGs [60-62], Inoue et al. noticed that there were a few common characteristics among them and summarized the following three empirical rules [50] for favoring the formation of bulk metallic glass: 1) multi-component systems consisting of

more than three elements; 2) significant difference in atomic size ratios above 12% among the main elements and 3) negative heat of mixing among the main elements. He argued that these factors will contribute to a densely packed structure in the undercooled liquid, which will limit the atomic mobility and hence favor the glass formation. Enlightened by these rules, an important progress made by Peker and Johnson was to design the Zr-Ti-Cu-Ni-Be [15] glass-forming alloy family (as commercially named with *Vitreloy*). These quinary glass-formers have distinct glass transition, very high stability of the supercooled liquid state, and high thermal stability against crystallization [1]. However, due to their qualitative nature, the guidance of these empirical rules in searching for new good glass formers is limited.

1.2.3.4 Pinpoint strategy

A more quantitative and explicit method called "pinpoint strategy" was recently proposed by Ma et al. [59] by applying the "competitive growth principle" [63] and treating the amorphous phase as another competing phase in an undercooled liquid. It argues that the competition between glass formation and crystalline phase growth controls the GFA, and a glass will form if its T_g isotherm is higher than the growth temperature of any of the possible crystalline phases. Practically, by monitoring the microstructure variation from a composite structure with one primary phase α to fully amorphous structure then to a composite structure with another primary

phase β (note: α and β are the two competing crystalline phases) as a function of alloy composition in a eutectic system. It is this phase switch that allows locating the best glass former in a given binary eutectic system (**Figure 1. 7**). Further, this strategy has been extended to a ternary eutectic system by treating binary eutectics as primary phases and the ternary eutectic as *the* "real" eutectic phase. This strategy had been successfully applied in finding the best glass formers in Cu-Zr [28], Cu-Zr-Al [64], La-Al-Ni [57], and Fe-Y-B [65] alloy systems. It is worthy of noting that this strategy is also valid in an asymmetric binary eutectic system, since the analysis results have shown the similar microstructure evolution as a function of alloy composition [59].

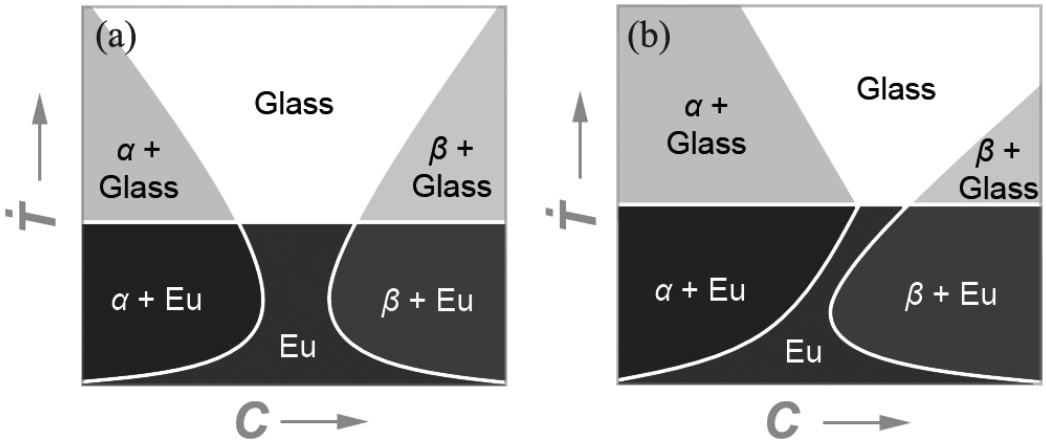

Figure 1. 7 Phase-formation maps including the glass- and composite-forming regions for the two kinds of eutectic system. (a) In a regular eutectic system, the best glass-forming range includes the eutectic (Eu) composition. (b) In an irregular eutectic system, the easy glass-forming range would be outside the eutectic composition. $\dot{T}$ is the cooling rate and C is the composition, reproduced from [59].

1.3 Mechanical behavior of BMGs

1.3.1 Inhomogeneous deformation

Along with the development of BMGs, their mechanical properties have been studied extensively. According to the deformation map first developed by Spaepen in 1977 [66] based on the free volume theory, there are two modes of deformation for BMGs depending on the temperature, the applied strain rate and the glass condition (**Figure 1. 8**): 1) ***Inhomogeneous deformation***, in which bulk metallic glass deforms at relatively low temperature and high strain rate. Deformation is localized in discrete, thin shear bands, leaving the rest of the material plastically undeformed. Upon yielding, metallic glasses often show plastic flow without work hardening, and tend to show work softening which leads to shear localization. 2) ***Homogeneous deformation***, in which bulk metallic glass deforms at relatively high temperature and low strain rate, and each element of bulk metallic glass is able to contribute to the deformation. In this thesis, we will *only* focus on the region of inhomogeneous deformation. This deformation map was later revisited by Argon [67, 68]. Recently, Lu [69] and Schuh [70] updated this map in terms of "bulk" metallic glass instead of amorphous ribbons.

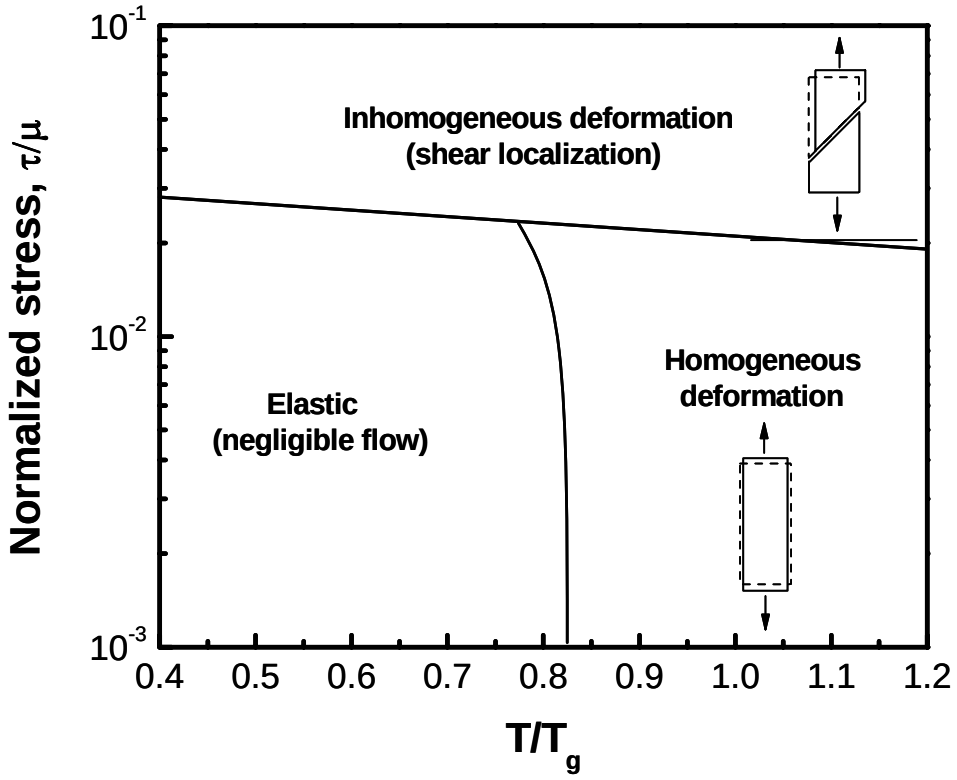

Figure 1. 8 Schematic deformation map for an amorphous metal illustrating the temperature and stress regions for homogeneous and inhomogeneous plastic flow, reproduced from [66].

In many cases, the mechanical properties of bulk metallic glasses are superior to those of their crystalline counterparts as shown in **Figure 1. 9**. In tensile loading, bulk metallic glasses exhibit elastic limits as high as 2%, while crystalline metals normally display 1% as their highest elastic limit. Due to the lack of crystalline defects e.g. dislocations and grain boundaries, bulk metallic glasses display unusually high strength approaching the theoretical limit of solids, under both tension and compression [24, 71, 72].

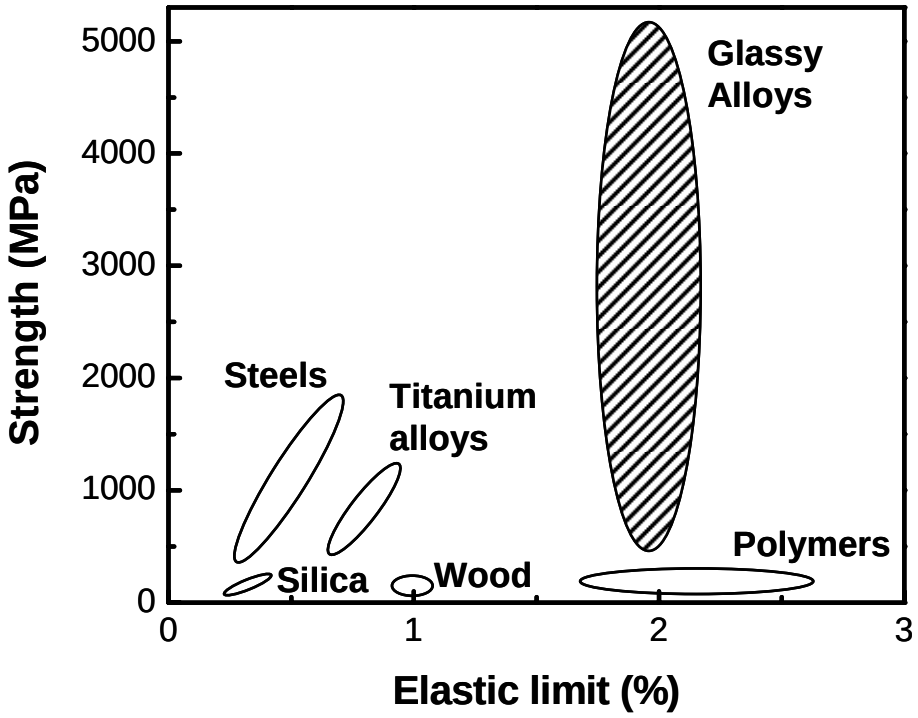

Figure 1. 9 Schematic illustration of typical strengths and elastic limits for various materials. Metallic glasses are unique with high strength and high elastic limit.

At ambient temperature, the plastic deformation of metallic glasses is accompanied with localization processes. The localization usually occurs in a shear mode through the formation of shear bands, which operate very rapidly and can accommodate displacements apparently up to nearly the millimeter scale [73]. Typical experimentally observed "slip steps" associated with the formation of shear bands in BMGs are shown in **Figure 1. 10**.

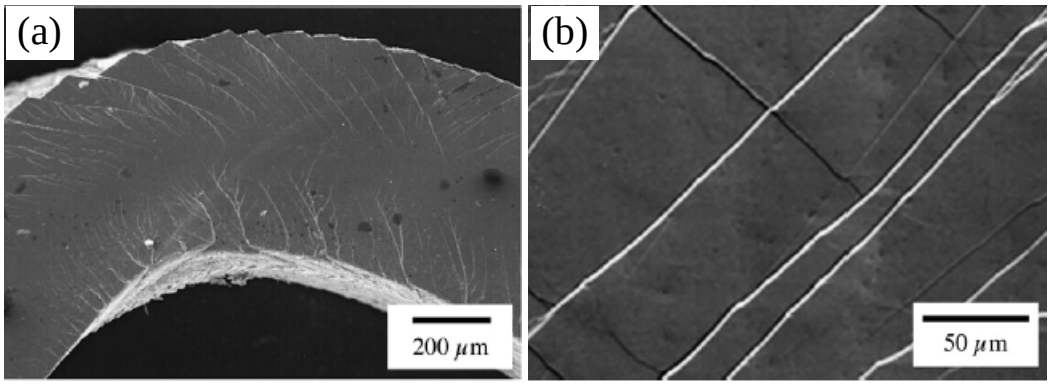

Figure 1. 10 SEM micrographs illustrating the "slip steps" or surface offsets associated with shear bands in deformed metallic glasses. (a) a strip of $Zr_{57}Nb_5Al_{10}Cu_{15.4}Ni_{12.6}$ BMG under bending test, adapted from [74], and (b) a $Zr_{52.5}Cu_{17.9}Ni_{14.6}Al_{10}Ti_5$ BMG under compression test, adapted from [75].

Shear localization or shear band formation is generally recognized as a direct consequence of strain softening – an increment of strain applied to a local volume element softens that element, allowing continued local deformation at ever-higher rates [76]. In metallic glasses, the dominant contributor to localization is generally believed to be a local change in the state of the glass (i.e. a local increase in free volume or evolution of structural order).

Simulation works have suggest that the basic sequence of events upon loading a metallic glass in the inhomogeneous regime is that, as stress is increased, strains are first accommodated elastically, until the stress level increases to the point where it can activate flow in a locally perturbed region. Owing to the perturbation, there is a mismatch in strain rate between the perturbed and unperturbed regions. The increased rate of strain accumulation

in the perturbed region is accompanied by strain softening, which further exacerbates the strain rate mismatch in a runaway growth process. The partitioning of strain rate into a shear band occurs over a finite range of applied macroscopic strain, and the strain in the band quickly becomes very large, exceeding unity in most cases [76].

Plastic shearing within a mature shear band stops when the driving force for shear decreases below certain threshold value, i.e. when the applied strain is fully accommodated by the shear accumulated within the band, relaxing the stress. This situation occurs commonly in constrained modes of loading, such as indentation [77-79], crack opening or crack tearing [80-83] , or compression of low-aspect-ratio specimens [84-86]. In these cases shear bands form exclusively to accommodate the imposed shape change, and strain only to the extent required for this purpose. The result is that, after a single shear band operates and arrests, the material can be deformed further through successive shear banding operations that occur upon continued straining. Load–displacement responses from such experiments exhibit characteristic patterns of "flow serration", as shown in **Figure 1. 11** (a) and (b) for constrained compression and indentation loading. Here each serration is a relaxation event associated with the formation of a shear band, registered as a load drop when the experiment is displacement-controlled (**Figure 1. 11** (a)), or a displacement burst under load-control (**Figure 1. 11** (b)).

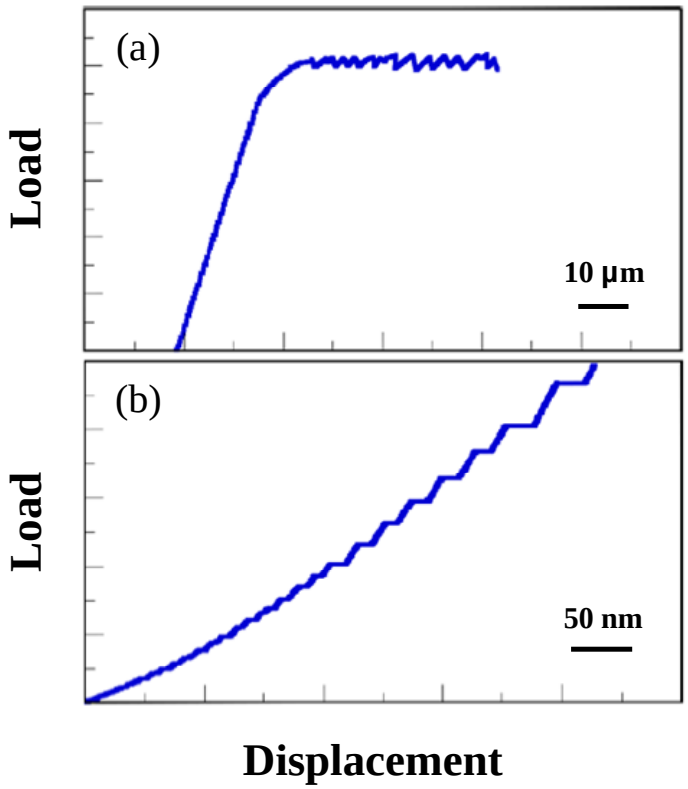

Figure 1. 11 Serrated flow of metallic glasses, through repeated shear band operation in confined loading. In (a), a $Pd_{77.5}Cu_6Si_{16.5}$ specimen with low aspect ratio under compression, adapted from [84], and (b) $Pd_{40}Cu_{30}Ni_{10}P_{20}$ glass under an load-control instrumented indentation, adapted from [87].

Upon yielding, most bulk metallic glasses display elastic-perfectly plastic mechanical behavior with no strain hardening. Shear bands play an important role in the deformation and fracture behavior of bulk metallic glasses. On the microscopic level, bulk metallic glasses are capable of legitimate plastic flow. However, in a macroscopic sense, most of the bulk metallic glasses tend to deform through shear localization process, and fail catastrophically on one dominant shear band [72] with very limited overall plasticity, which limits their potential application as an engineering material.

Very recently, a few bulk metallic glasses have been reported to exhibit attractive compressive plastic flow [88-94]. Lewandowski and co-workers demonstrated a correlation between the fracture energy G_c of metallic glasses and their elastic properties [90]. As shown in **Figure 1. 12**, amorphous alloys with $\mu/B < 0.41$ are tough, while those with $\mu/B > 0.43$ are brittle. This correlation can also be expressed in terms of Poisson's ratio, ν. For instance, Schroers and Johnson [89] reported that amorphous $Pt_{57.5}Cu_{14.7}Ni_{5.3}P_{22.5}$, which has a particularly large Poisson's ratio of $\nu = 0.42$ (and thus small μ/B), can show large plastic strains in compression and bending, and has a large fracture toughness ($K_c \approx 80$ MPa $m^{1/2}$) as well. Lewandowski and co-workers [90] interpreted the correlation between μ/B (or ν) and fracture energy in terms of a competition between plastic flow on the one hand and fracture on the other, followed Kelly et al.'s [95] interpretation of the similar correlation [96] in crystalline materials.

An significant point about these correlations is that it appears possible to predict, at least approximately, the elastic properties of a metallic glass based on an appropriately weighted average of the properties of its constituent elements [97] (although recent work [92] suggests that this may not always be true). Thus, as Lewandowski and co-workers pointed out [90], it might be possible to design a metallic glass composition (at least in terms of the majority elements) with the appropriate elastic constants and thus enhanced plasticity in mind. This idea was later supported by the discovery of

super plastic BMGs in Zr-Cu-Ni-Al system [94]. Through the appropriate choice of the composition by controlling elastic moduli, super plasticity with true compressive plastic strain over 160% is achieved at room temperature in Zr-Cu-Ni-Al alloy system.

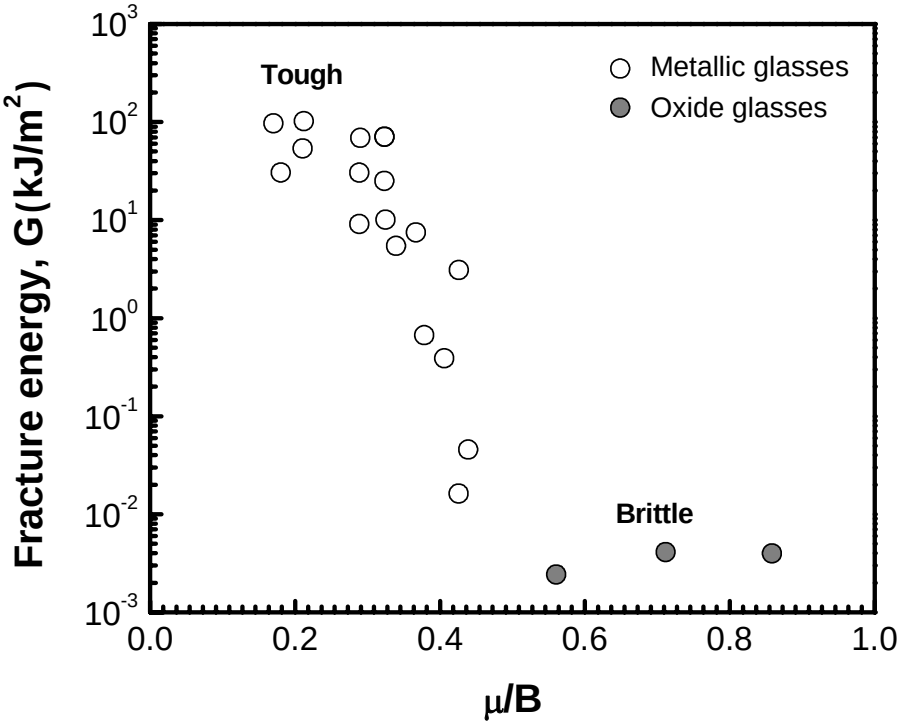

Figure 1. 12 Effect of the dimensionless ratio of shear and bulk moduli (μ/B) on the toughness of various glasses, expressed in terms of the fracture energy G_c, reproduced from [90].

1.3.2 Deformation mechanisms

The exact nature of the atomic motion of bulk metallic glass under deformation has not been fully resolved, although it is generally accepted that

the fundamental unit process underlying the deformation must be a local atomic rearrangement that can accommodate shear strain. The two most acknowledged deformation mechanisms for BMGs are the "shear transformation zone" (STZ) model and the free volume model, as illustrated with the two-dimensional schematics in **Figure 1. 13** (a) and (b), respectively.

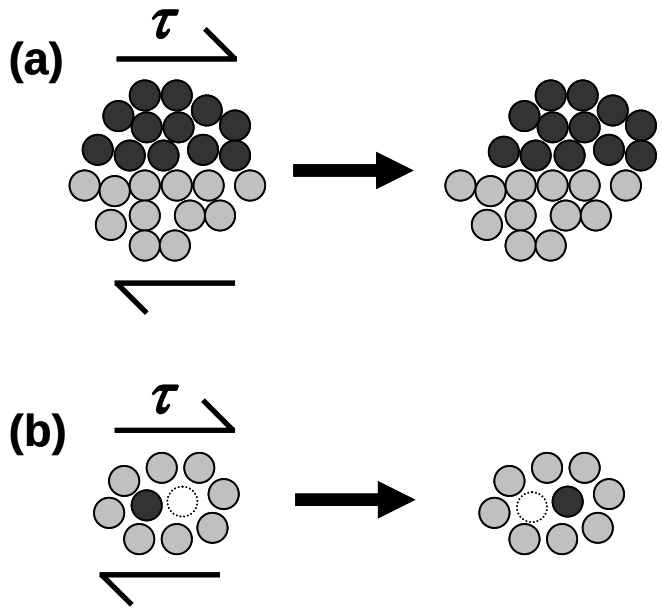

Figure 1. 13 Two-dimensional schematics of the atomistic deformation mechanisms proposed for amorphous metals (a) shear transformation zone model [67] (b) free volume model [66], reproduced from [76].

1.3.2.1 Shear transformation zone model

Originally proposed by Argon and Kuo [98], a shear transformation zone is essentially a local cluster of atoms that undergoes an inelastic shear distortion from one relatively low energy configuration to a second such configuration, crossing an activated configuration of higher energy and volume (**Figure 1. 13** (a)).

The shear transformation zone model has been successfully applied in explaining the steady state deformation behavior of BMGs [99, 100]. More complicated models [83, 101-105] based on STZ viewpoints have been developed, and suggest that STZs are common to deformation of all amorphous metals, although details of the structure, size and energy scales of STZs may vary from one glass to the next.

1.3.2.2 Free volume model

A hypothesis on the existence of free volume in glassy materials was first proposed by Cohen and Turnbull [106] and was subsequently adapted for deformation of metallic glasses by Spaepen [66]. This model essentially views deformation as a series of discrete atomic jumps in the glass, as shown in **Figure 1. 13** (b); these jumps are obviously favored near sites of high free volume which can more readily accommodate them.

The free volume model describes the deformation process in metallic glass as the net result of two competing processes: a shear-induced disordering and a diffusion-controlled reordering process. When some of the atoms experience a non-equilibrium situation (e.g. a shear stress is applied), they will make a series of diffusional jumps to make structural rearrangements (**Figure 1. 13** (b)). The free volume model has successfully explained the homogeneous deformation behavior [69, 107, 108] and some

aspects of inhomogeneous deformation behavior in bulk metallic glass [109-113].

The above two models shared many common features that are crucial to understanding the macroscopic deformation of metallic glasses, e.g. both mechanisms are thermally activated, and exhibit similar energy scales [76]. The major difference is in the fundamental unit event to accommodate the shear strain: in STZ model it is a collective motion of a cluster of atoms while in free volume model it is a more highly localized atomic jump.

1.3.3 BMG matrix composites

A major drawback of BMGs for engineering application is the low ductility (usually < 1%) [89] under tensile or compressive loading at ambient temperature. Metallic glasses deform by highly localized shear flow, which often leads to catastrophic failure without much macroscopic plasticity. Although the local plastic strain in a single shear band is quite large, the overall strain is determined by the number of activated shear bands. In a tensile or compression test, only a few shear bands are active, which makes the stress-strain curve appear similar to those of brittle materials [114].

The introduction of a second phase into the glass matrix has been utilized to improve the ductility of the composite material by both promoting

initiation of a large number of shear bands (distributing the macroscopic plastic strain over as large a volume as possible) and inhibiting shear band propagation (reducing the shear strain on any one band and thus delay fracture). The synthesis of second phase reinforced BMGs composites can be roughly grouped into three categories: ex-situ induced hard particles or fibers [36, 114-117]; devitrification induced crystalline phase [118-120]; and in-situ formation of ductile crystalline phase [99, 121, 122]. Among these methods, the last in-situ method has considerable advantages such as simple technique (i.e. low cost) and strong reinforcing phase-matrix bonding produced by low energy interfaces [121]. This method succeeded in significantly enhancing ductility of BMG matrix composites even under uniaxial tensile mode. Johnson *et al.* first prepared ductile metal (Nb) reinforced $Zr_{41.2}Ti_{13.8}Cu_{12.5}Ni_{10}Be_{22.5}$ BMG matrix composite via the in-situ processing. The material exhibits total strain of over 8% with an apparent strain hardening behavior under quasistatic compressive loading [122] (**Figure 1. 14**).

With this strategy, Lee et al. [99] reported 5% of plastic strain in $La_{74}Al_{14}(Cu,Ni)_{12}$ BMG matrix composites with large volume fraction of hcp α-La phases under tension (**Figure 1. 15**). With similar approach, very recently, Hofmann et al. [123] developed Ti–Zr-based BMG "designed composites" with room-temperature tensile ductility exceeding 10%, high K_{1C} up to 170 MPa $m^{1/2}$, and fracture energy for crack propagation as high as G_{1C}<340 kJ m^{-2}. The K_{1C} and G_{1C} values equal or surpass those achievable in the toughest

titanium or steel alloys, placing BMG composites among the toughest known materials. An obvious necking was observed in the deformed composite sample, which is in great contrast to the brittle fracture of monolithic glass sample (**Figure 1. 16**).

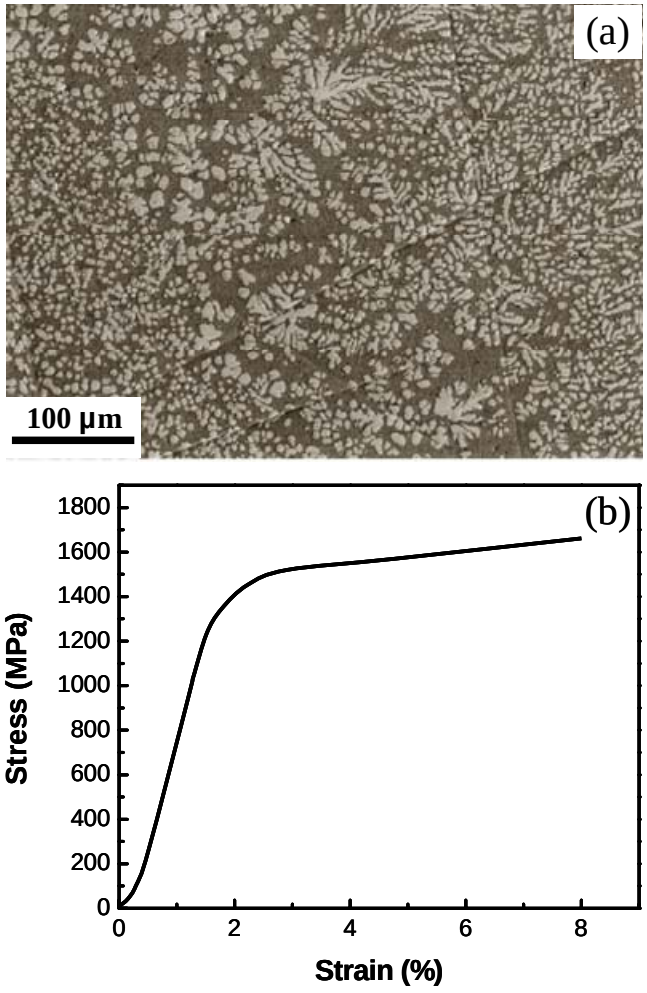

Figure 1. 14 (a) Microstructures of Nb reinforced $Zr_{41.2}Ti_{13.8}Cu_{12.5}Ni_{10}Be_{22.5}$ BMG matrix composite and (b) its compressive stress-strain curve for cylindrical specimen, adapted from [122].

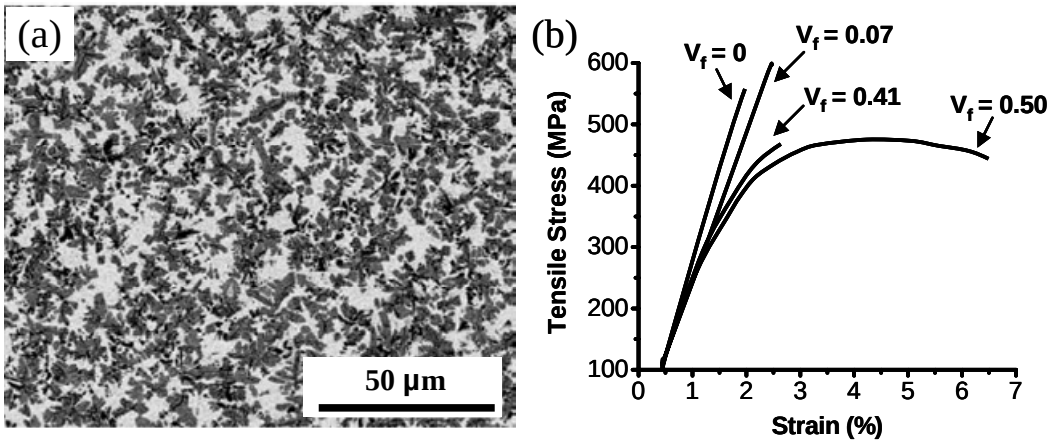

Figure 1. 15 Backscattering SEM image (a) of cross-section of $La_{74}Al_{14}(Cu,Ni)_{12}$ BMG matrix composites with 50% in volume fraction of crystalline phase and representative tensile stress-strain curves of monolithic amorphous alloy and composite samples, adapted from [99].

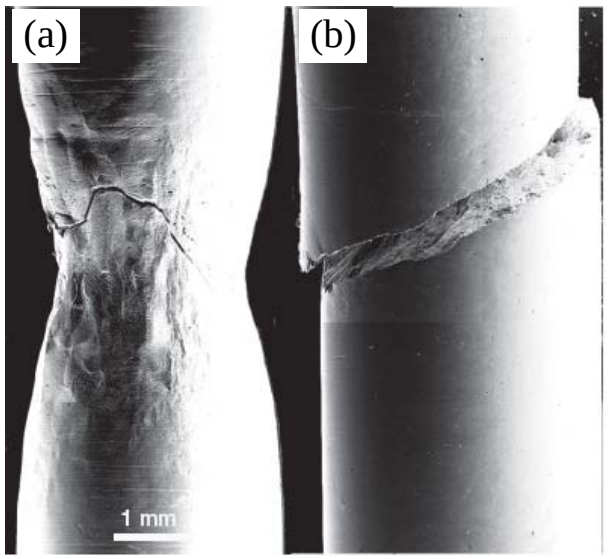

Figure 1. 16 (a) SEM micrograph of necking in $Zr_{39.6}Ti_{33.9}Nb_{7.6}Cu_{6.4}Be_{12.5}$ BMG matrix composites, and (b) Brittle fracture representative of all monolithic BMGs, adapted from [123].

1.4 Objective and outline of this thesis

The purpose of this study was to have an in-depth understanding of the nature of the *formation* and *mechanical behavior* of Zr-Cu-based BMGs. To achieve this, systematic investigations on the glass formation, strength, plasticity, as well as "malleable-to-brittle" transition of Zr-Cu-based BMGs have been carried out.

There are five chapters in this thesis.

In Chapter 1 (this chapter), the general knowledge of BMGs was introduced. The glass formation and mechanical behavior of BMGs were reviewed in detail, followed by the objective and outline of the present study.

In Chapter 2, the discovery of a new group of glass - "intermetallic glass" in the Zr-Cu binary system was demonstrated. The formation mechanism was discussed in terms of both kinetics and thermodynamics. The mechanical properties of Zr-Cu intermetallic glass and glass matrix composites were investigated.

In Chapter 3, the flaw sensitivity issue was studied on three ($Zr_{51}Cu_{49}$)-based BMGs from the strength perspective. Weibull statistics was applied to characterize the strength variability of these BMGs. The relationship between the Weibull modulus, plasticity, as well as the glass forming ability is discussed.

In Chapter 4, the effect of sample geometry on the plasticity of Zr-Cu-Al BMG was investigated systematically, and a "stress gradient enhanced plasticity" concept has been established. The mechanism was discussed with Finite element analysis through collaborative work.

In Chapter 5, the sample size dependence of mechanical properties of Zr-Cu-Al BMG was investigated. A "malleable-to-brittle" transition that occurred at a critical sample size, was observed in both as-cast and annealed BMG samples. The significance of identifying the critical size in a specific BMG system was discussed.

Finally in Chapter 6, the salient results of this thesis were summarized and the topics for future research were suggested.

Chapter 2

Bulk “intermetallic glass” by rapid quenching

2.1 Introduction

Ever since its discovery, formation of metallic glass *through cooling a liquid* is commonly believed to be at or near eutectic composition [4, 124]. This is based on the traditional Turnbull’s kinetics T_{rg} criterion ($T_{rg} = T_g / T_l$, where T_g is the glass transition temperature and T_l is the liquidus temperature) [55, 125] which was established when considering bypassing the nucleation and/or

growth of crystalline phases. This criterion has led to the general practice of locating glass formers specifically in the deep-eutectics, as denoted by the shaded region in **Figure 2. 1** (b).

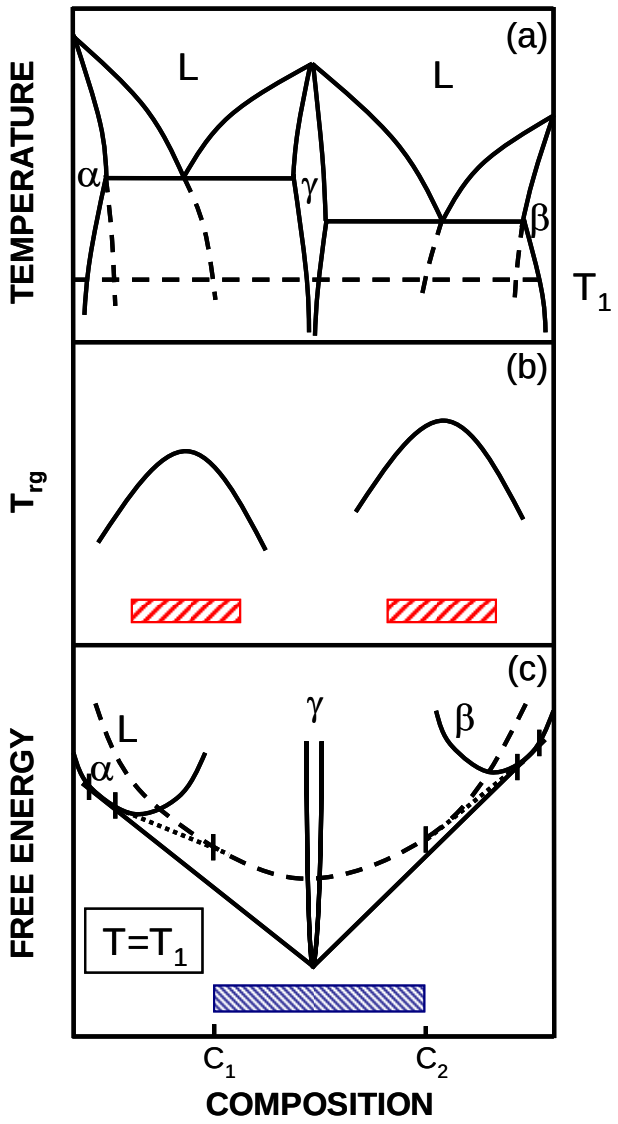

Figure 2. 1 Two conventional glass forming regions. (a) A schematic phase diagram of a binary alloy system consisted of two eutectics separated by an intermetallic phase. Two distinct glass forming regions (shaded area) based on Turnbull's kinetics T_{rg} criterion for quenched glass (b) and thermodynamics consideration for solid-state reacted glass (c).

On the other hand, Schwarz and Johnson have reported the formation of amorphous phase between thin films of two pure crystalline metals *through solid-state reaction* under isothermal conditions [126]. They attributed this glass formation to the large negative heat of mixing of the two base metals which led to a large negative free energy of mixing, and the low reaction temperature which suppressed the formation of possible thermodynamically stable intermetallic phases (γ) (**Figure 2. 1** (c)). This has lead to the glass formation over a substantial range of compositions centered in the phase diagram i.e. over the intermetallics (shaded region in **Figure 2. 1** (c)), rather than near the deep-eutectics for liquid-quenched glass. Besides the fact that most of the products through solid-state reaction are in the form of thin films (as in thermal inter-diffusion) [126, 127] or of powders (as in mechanically milling) [128, 129], the reaction is often incomplete, retarding their practical applications.

When examining closely the free energy diagram as shown in **Figure 2. 1** (c), since the free energy of the intermetallic phase (γ) is rising sharply it is conceivable that thermodynamically the free energy of the amorphous phase is much lower than that of intermetallic phase when away from the stoichiometric composition. If the kinetic condition is met to suppress the formation of the two stable primary α and β phases, e.g. under the rapid quenching with limited atomic diffusion, it is therefore possible to form glass

at these two thermodynamically favored composition regions separated by the intermetallic composition. Our above analysis points out the possibility of forming a new group of glasses through quenching near the intermetallics, which is distinguishably different from the traditional “eutectic glass”. The alloys which meet both the thermodynamic and kinetic conditions are not only in extremely narrow composition ranges, but also exist as a pair close to but separated by the intermetallic composition.

In this chapter, we demonstrated this possibility by discovery of two bulk optimum glass formers $Zr_{48.5}Cu_{51.5}$ and $Zr_{51}Cu_{49}$ in the vicinity of the stoichiometric ZrCu intermetallics in Zr-Cu binary system. Since they are close to the intermetallics, we designate these glasses as quenched “intermetallic glass”, distinguishing it from the conventional quenched “eutectic glass” obtained near deep-eutectics.

2.2 Experimental procedure

The alloy ingots were prepared by arc melting mixtures of pure Zr and Cu in a Ti-gettered high-purity argon atmosphere. Each ingot was remelted at least five times in order to obtain chemical homogeneity. The Zr-Cu alloys in rod

with 2 mm in diameter were prepared from the ingot by water-cooled copper mold suction casting.

The longitudinal cross sections of as-cast samples were analyzed by Scanning Electronic Microscopy (SEM) and X-ray diffraction (XRD). The corresponding melt-spun samples were prepared by a single roller melt spinning technique in a purified argon atmosphere with a wheel speed of 20 ms^{-1}. Differential scanning calorimetry (DSC) was undertaken to measure the thermal properties of melt-spun glassy ribbons and bulk samples.

Uniaxial compression testing was conducted at room temperature with a constant engineering strain rate of 10^{-4} s^{-1}. The test specimens were about 4 mm in length and 2 mm in diameter, providing a nominal aspect ratio of ~2:1 as recommended by ASTM E9-89a (2000) for testing high strength materials.

2.3 Results and Discussion

2.3.1 Glass formation

The representative XRD spectrums of as-cast Zr_xCu_{100-x} (x=45-56) 2 mm alloys were shown in **Figure 2. 2**.

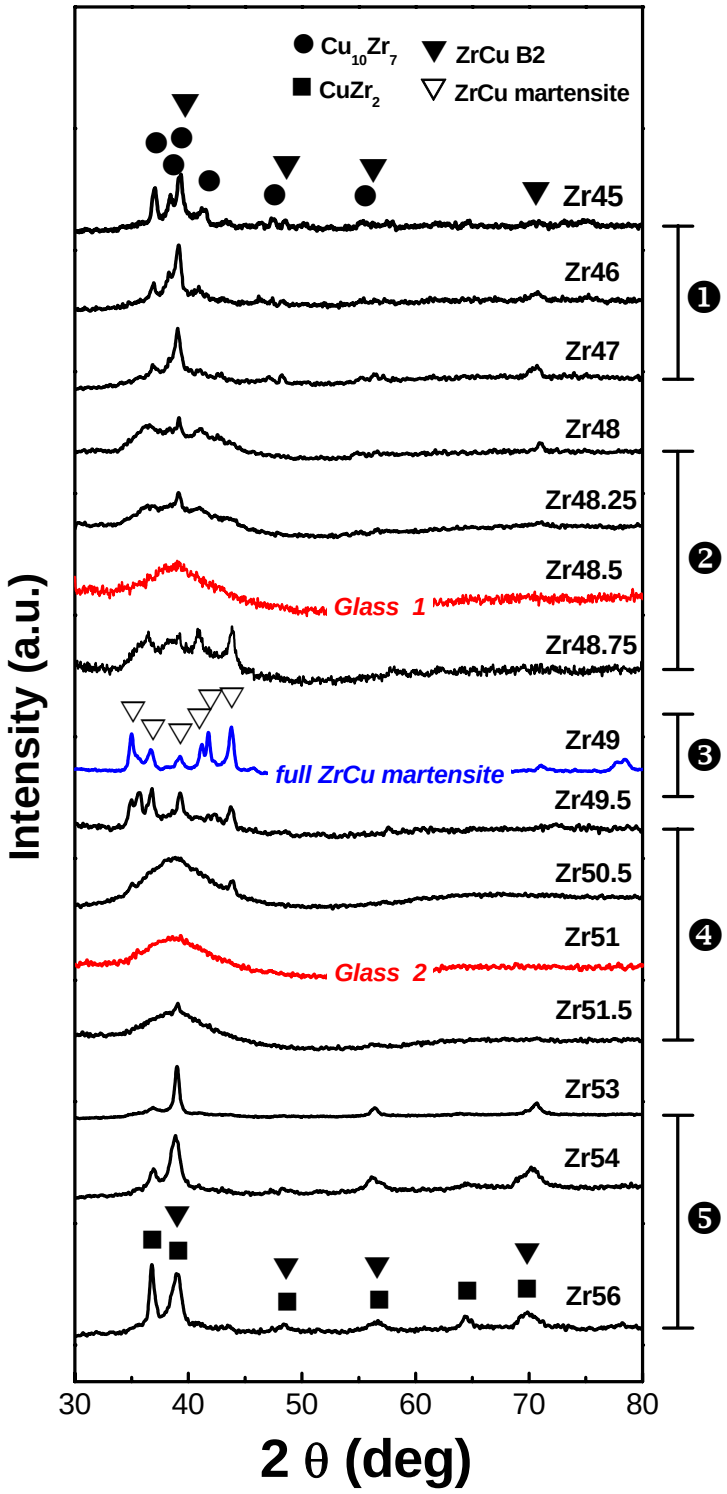

Figure 2. 2 The representative XRD spectrums of Zr_xCu_{100-x} (x=45-56) as-cast 2 mm alloys. Five regions with distinct microstructures are observed.

With increasing Zr content x, these spectrums can be divided into five distinct regions defined by the as-cast microstructure: (1) a fully crystalline two-phase region containing $Cu_{10}Zr_7$ and ZrCu B2 phases for alloys with x from 45 to 47 , (2) an amorphous phase containing region for x from 48 to 48.75, inclusive of a single-phase amorphous microstructure at $Zr_{48.5}Cu_{51.5}$, (3) an almost full ZrCu martensite structure at $Zr_{49}Cu_{51}$, (4) an amorphous phase containing region for x from 49.5 to 51.5 , inclusive of a single-phase amorphous microstructure again at $Zr_{51}Cu_{49}$, and (5) a fully crystalline two-phase region containing $CuZr_2$ and ZrCu B2 phases for x from 53 to 56. The XRD results clearly indicate two optimum glass formers, one at $Zr_{48.5}Cu_{51.5}$ and the other at $Zr_{51}Cu_{49}$, with a fully crystalline phase of ZrCu martensitic structure at $Zr_{49}Cu_{51}$ in between. The corresponding SEM micrographs are shown in **Figure 2. 3** further confirming the microstructural evolution of these alloys.

Figure 2. 4 shows the DSC curves of the Zr_xCu_{100-x} (x from 48.5 to 51) melt spun ribbons and as-cast bulk samples. With increasing of Zr content, both the glass transition temperature (T_g) and the onset crystallization temperature (T_x) decreased only slightly, which yields almost a constant T_{rg} value among this compositional range. However, the distinct crystallization profiles of the two intermetallic glasses signify their different crystallization products and behavior.

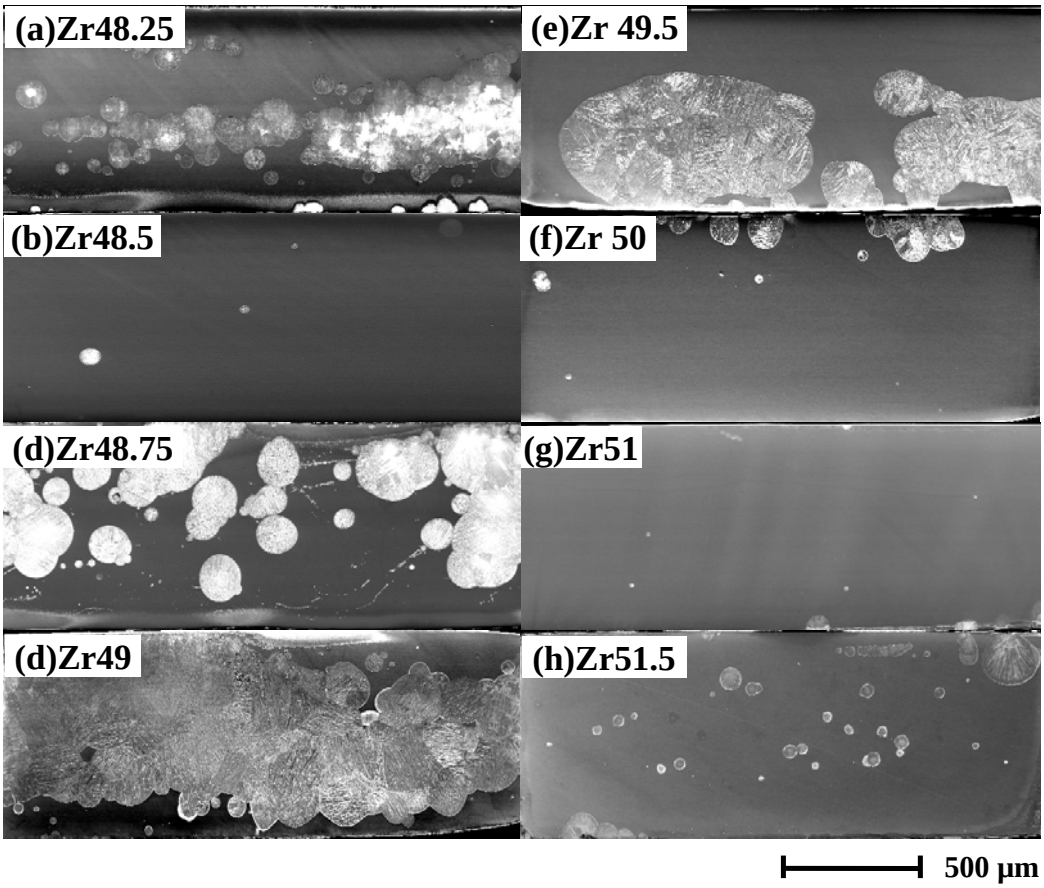

Figure 2. 3 The representative SEM micrographs of Zr_xCu_{100-x} (x=45-56) as-cast 2 mm alloys.

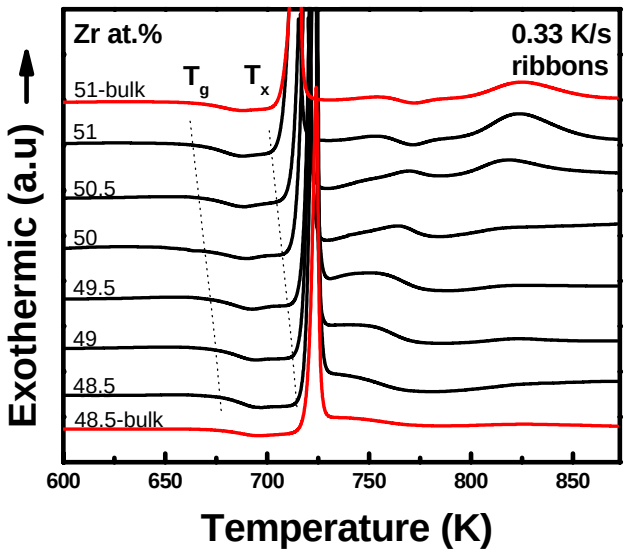

Figure 2. 4 The representative DSC curves of Zr_xCu_{100-x} (x from 48.5 to 51) melt spun ribbons and as-cast bulk samples.

The hypothetic free energy curves and the corresponding portion of Zr-Cu phase diagram with Zr content from 45% to 56% are shown in **Figure 2. 5**. At the centre of the phase diagram, the intermetallic phase ZrCu B2 has the lowest Gibbs free energy (G_i) and thus it is favored to be formed thermodynamically (denoted by blue solid line in **Figure 2. 5**). This explains why even under liquid quenching condition a full ZrCu martensitic structure, originated from ZrCu B2 parent phase through martensitic transformation [130-132], was obtained in the as-cast $Zr_{49}Cu_{51}$ alloy. As the composition was moved slightly away from $Zr_{49}Cu_{51}$ towards both sides, the two eutectic reactions $L \rightarrow Cu_{10}Zr_7$ + ZrCu and $L \rightarrow$ ZrCu + $CuZr_2$ were kinetically suppressed due to the fact that these alloys are far away from equilibrium phases. Therefore, the microstructures of the alloys were determined thermodynamically by the relative values of the Gibbs free energy of ZrCu B2 intermetallic phase (G_i) and the undercooled liquid/glass (G_L). Due to the sharp profile of G_i, the undercooled liquid has now the lowest Gibbs free energy (red solid line in **Figure 2. 5**), and hence a pair of glasses should be formed with the equiatomic composition in between centered in the phase diagram. As the alloy composition was moved further away from the central region, the two eutectic reactions $L \rightarrow Cu_{10}Zr_7$ + ZrCu and $L \rightarrow$ ZrCu + $CuZr_2$ could start to become feasible in kinetics and thus two-phase microstructures of $Cu_{10}Zr_7$ + ZrCu B2 and ZrCu B2 + $CuZr_2$ were formed at the both sides further away from the centre (green part in **Figure 2. 5**).

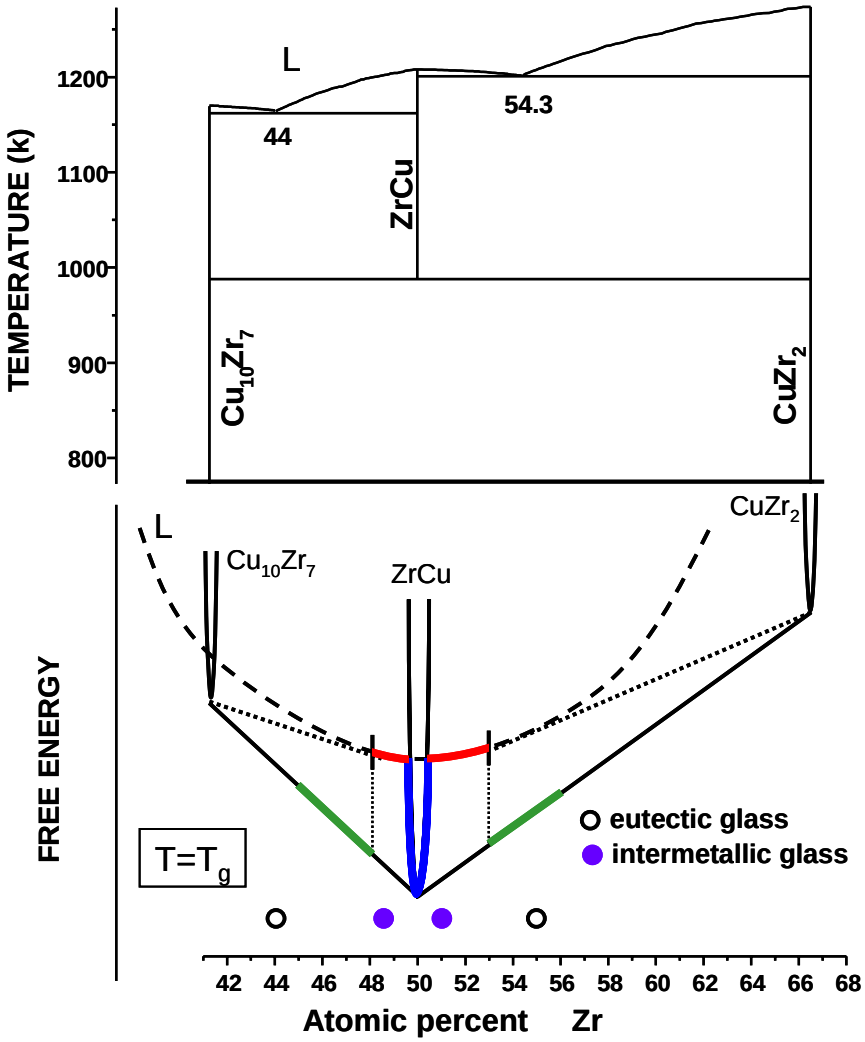

Figure 2. 5 Hypothetic free energy curves and forming region of "intermetallic glass" under quenching. The "intermetallic glass" forming region (red solid line) with two optimum "intermetallic glass" formers (purple solid circle) were located close to but separated by the equiatomic composition in the corresponding portion of Zr-Cu phase diagram. The two "eutectic glasses" at $Zr_{44}Cu_{56}$ [133] and $Zr_{55}Cu_{45}$ [134] were marked in black open circle for comparison.

We have noticed that, the martensitic transformation [130-132] around the Zr-Cu equiatomic composition should not affect the current glass formation in that the glass transition temperatures (T_g over 660 K, see

Figure 2. 4) are substantially higher than the martensitic transformation temperature (M_s=440 K). Therefore, the observed martensitic structure at $Zr_{49}Cu_{51}$ is the final product of this martensitic transformation from ZrCu B2 phase and the ZrCu martensite should not be considered as any competing phase to the “intermetallic glass” pair.

As demonstrated above, the formation of “intermetallic glass” exhibited highly compositional dependence, which makes it non-trivial to be discovered. However, understanding of the underlying “intermetallic glass” formation mechanism in both thermodynamics and kinetics (**Figure 2. 5**) has guided us to pinpoint them through monitoring the detailed microstructural evolution. Similar to the strategy [4, 124] developed for locating traditional “eutectic glass” in deep-eutectics, the new group of “intermetallic glasses” can be effectively pinpointed near intermetallic compositions.

These results matched well with our predictions in that a new group of glass adjacent to the intermetallic composition was obtained through quenching. It is worthy of pointing out that, the current two glass formers are unquestionably not and far away from the two optimum $Zr_{44}Cu_{56}$ [133] and $Zr_{55}Cu_{45}$ [134] amorphous alloys, associated with the two corresponding eutectic compositions i.e. $Zr_{44}Cu_{56}$ and $Zr_{54.3}Cu_{45.7}$ respectively (**Figure 2. 5**). Thus our two glasses should not be regarded as the “eutectic glasses”. Furthermore, intrinsically distinguished it from the glasses made by solid-state reaction, the Zr-Cu “intermetallic glass” can be synthesized in bulk size

i.e. 2 mm in diameter, which makes it more promising in the consideration of engineering applications.

It is clear that this finding provides a fertile field for future research. Firstly, it points out that the feasible system for forming “intermetallic glass” pair might have the following characteristics as in Zr-Cu system: (1) the system is known to readily form glass by both rapid quenching [27-29, 134] and solid-state reaction [135, 136]. (2) any two of the base elements exhibit a large negative heat of mixing [137], which provides the driving force for the glass formation in thermodynamics. (3) in the centre of the phase diagram there exists a intermetallic compound phase, which has a sharp profile of Gibbs free energy. The qualified candidates by our speculation are ETM-LTM systems (ETM=Zr, Ti, Hf, etc., LTM=Ni, Cu, Co, etc.). Secondly, it offers a new prototype for future atomic modeling of glass formation. Historically, several atomic models [138, 139] have correlated the optimum glass formers with highly dense-packed structure, which can be characterized quantitatively by physical parameters such as density and viscosity. However, these considerations may not play a determined role in the formation of “intermetallic glass” as these parameters are hardly expected to follow such a highly compositional dependence. Thirdly, the structure of glasses made by solid-state reaction and rapid quenching are reported to be indeed very similar, both topologically and chemically [140]. However, whether the structure of the “intermetallic glass” is also similar to those of traditional ones

is remained to be studied. Fourthly, with the composition among the current “intermetallic glass” forming region, $Zr_{50}Cu_{50}$ BMG has shown outstanding mechanical properties with good plasticity [88, 141-143]. This may provide a hint for the distinct structure and deformation behavior of the “intermetallic glass”. Finally, the “confusion principle” [144] has been employed successfully in most of current BMG systems. It could be anticipated that, with more components being involved, the primary phases like α, β, will be more difficult to form and thus the glass forming region (GFR) may be broadened and the glass forming ability (GFA) may be improved as well. It is worthy of noting that, in a multi-component system the GFR will be characterized by a 3-D space rather than the 2-D space and therefore should yield more potential optimum glass formers.

2.3.2 Mechanical properties

2.3.2.1 Composition induced microstructural inhomogeneity in Zr_xCu_{100-x} (x from 48.5 to 51) as-cast alloys

The previous detailed microstructural analysis allows examining the mechanical properties of the newly discovered intermetallic glasses and the amorphous matrix composites with controlled volume fraction of ZrCu

martensite, which was regarded as a key microstructural feature to enhance the plasticity of several Zr-Cu-based BMGs and their composites [141, 145-147].

The two fully amorphous alloys $Zr_{48.5}Cu_{51.5}$, and $Zr_{51}Cu_{49}$, and two composites $Zr_{49.5}Cu_{50.5}$, and $Zr_{49}Cu_{51}$ were chosen as the examples with representative microstructures. The volume fraction (V_f) of ZrCu martensite in the amorphous matrix was estimated to be 77% for $Zr_{49}Cu_{51}$, and 40% for $Zr_{49.5}Cu_{50.5}$, by quantitative image analysis of the SEM micrograph shown in **Figure 2. 3** (d) and (e). The stress-strain curves of the four Zr-Cu alloys are shown in **Figure 2. 6**. The data of the typical mechanical properties are summarized in **Table 2. 1**.

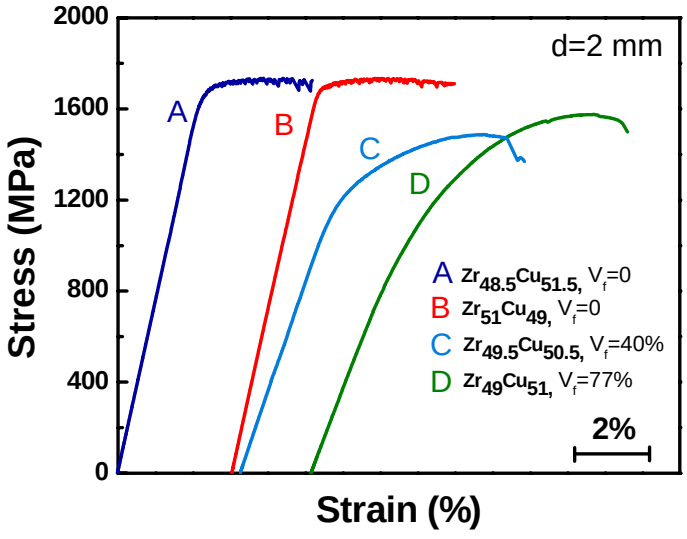

Figure 2. 6 The engineering compressive stress-strain curves of Zr-Cu amorphous matrix composites with varied volume fraction of ZrCu martensite. A- $Zr_{48.5}Cu_{51.5}$ and B- $Zr_{51}Cu_{49}$ alloy with fully amorphous structure; C- $Zr_{49.5}Cu_{50.5}$ alloy with 40% of ZrCu martensite, and D- $Zr_{49}Cu_{51}$ alloy with 77% of ZrCu martensite in the amorphous matrix.

Table 2. 1 Mechanical properties of $Zr_{48.5}Cu_{51.5}$, $Zr_{51}Cu_{49}$, $Zr_{49.5}Cu_{50.5}$, and $Zr_{49}Cu_{51}$ as-cast alloys, with various volume fraction of ZrCu martensite in the amorphous matrix, under compression at room temperature.

Alloy (d=2 mm)	**$Zr_{48.5}Cu_{51.5}$**	**$Zr_{51}Cu_{49}$**	**$Zr_{49.5}Cu_{50.5}$**	**$Zr_{49}Cu_{51}$**
Volume fraction, V_f	0%	0%	40%	77%
0.2% Yield strength (MPa)	1680	1700	1180	970
Young's Modulus (GPa)	75	75	70	50
Plastic Strain	3.0%	3.6%	4.7%	5%

The two intermetallic glasses $Zr_{48.5}Cu_{51.5}$ and $Zr_{51}Cu_{49}$ exhibited typical behavior of BMG with similar plastic strain of ~3% prior to failure, same Young's Modulus of 75 GPa, similar strength of ~1700 MPa with visibly serrated flow characterized stress-strain profile. Note that there is no strain-hardening observed from the stress-strain curve of the monolithic glassy alloys. In great contrast, the composite alloy $Zr_{49.5}Cu_{50.5}$ with 40% of ZrCu martensite exhibited a noticeable strain-hardening with 4.7% of plastic strain. Clearly, the strain-hardening should be attributed to the interaction of ZrCu martensite phase with shear bands. The similar phenomenon was observed in the $Zr_{49}Cu_{51}$ alloy with a higher volume fraction (77%) of ZrCu martensite.

The yield stress and Young's modulus was found to be decreased monotonically as the volume fraction of ZrCu martensite increases. This trend suggests that the yield stress and Young's modulus of the composites can be reasonably described by the rule-of-mixtures based on load transfer. Different from monolithic glass, no evident serrations were observed in the stress-strain

profiles of composites ($Zr_{49.5}Cu_{50.5}$ and $Zr_{49}Cu_{51}$). This is due to the formation of multiple shear bands, induced by the crystalline phase to distribute the deformation more homogeneously.

The above results thus reinforce the statement that strain-hardening can only be achieved in a composite structure. For a monolithic glass with a general lack of intrinsic structural inhomogeneities, the highly localized shearing deformation weakens the material and often leads to the catastrophic failure. While for a composite structure with crystalline phase(s) reinforced, the evoked strain-hardening mechanism can overcome the instability of shear banding by multiplication of shear bands.

2.3.2.2 Cooling history induced microstructural inhomogeneity in $Zr_{48.5}Cu_{51.5}$ as-cast alloy

The previous section discussed the mechanical properties of fully glassy alloys and composites, in which the microstructures were governed by the glass forming ability of the master alloys with specific compositions. However, The microstructural inhomogeneities can also be induced in a single-cast rod along the longitudinal direction because of the uneven cooling rates in the casting process [148]. This issue becomes extremely important for those alloys with sample size approaching the critical thickness for glass formation.

In this section, we will focus on the microstructure inhomogeneities along the longitudinal direction of $Zr_{48.5}Cu_{51.5}$ rod sample and the corresponding mechanical properties.

Figure 2. 7 shows a representative microstructure of the 2 mm as-cast $Zr_{48.5}Cu_{51.5}$ rod. From the top (i.e. the last solidified part) to the bottom (i.e. the first solidified part), the microstructure was highly inhomogeneous and changed from fully crystalline structure to ring-type composite structure (i.e. large crystalline particles exist in the center and amorphous phase only in the periphery) then to regular composite (i.e. fine crystallites are distributed uniformly in the amorphous matrix) and finally to fully amorphous structure. This longitudinally microstructural inhomogeneity thus provide a nice example for exploring the mechanical properties of BMG and BMG matrix composites with varied volume fractions of secondary phase in one single as-cast rod.

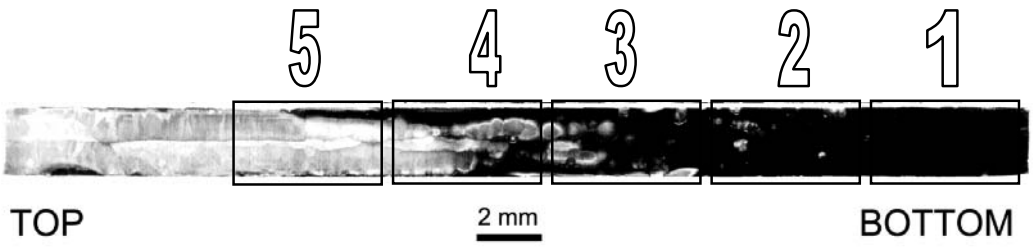

Figure 2. 7 Scanned micrograph of longitudinal cross section of a whole 2 mm as-cast $Zr_{48.5}Cu_{51.5}$ rod. The microstructural inhomogeneity in the longitudinal direction was observed. Sample 1-5 are representatives of various microstructures.

To investigate the mechanical properties of different parts of this single as-cast rod, samples with 4 mm in length each were cut from the rod for compression tests. The samples were named as sample 1 - for the one closer to the bottom, to sample 5 – for the one closer to the top (**Figure 2. 7**). Based on quantitative image analysis, the volume fraction of crystalline phases (i.e. ZrCu martensite) was estimated to increase from 0% (Sample 1) to 93% (Sample 5) as summarized in **Table 2. 2**.

Figure 2. 8 shows representative uniaxial compressive stress-strain curves for the samples 1-5. All the test results are summarized in **Table 2. 2**.

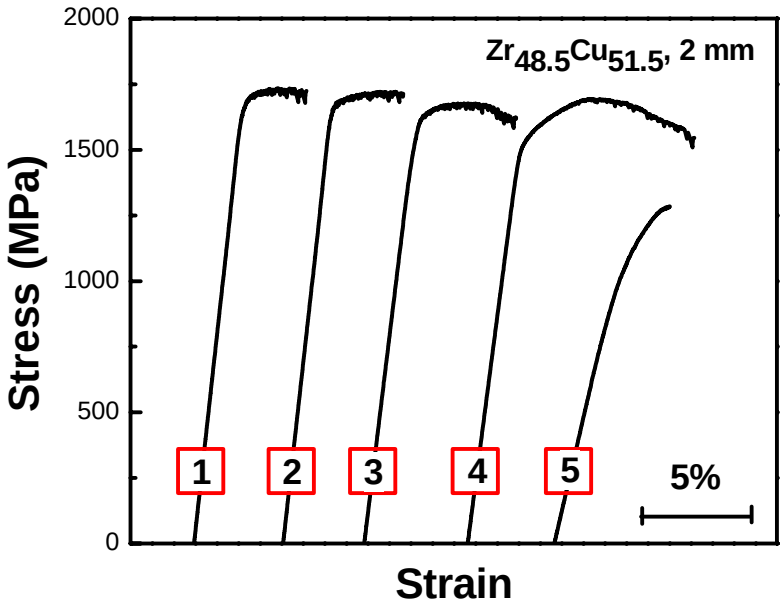

Figure 2. 8 The compressive stress-strain curves of the samples 1-5, which were cut from the different part of one single $Zr_{48.5}Cu_{51.5}$ as-cast 2 mm rod.

Table 2. 2 Mechanical properties of the samples 1-5, which were cut from the different part of one single $Zr_{48.5}Cu_{51.5}$ as-cast 2 mm rod, with various volume fractions of ZrCu martensite phase in the amorphous matrix.

Sample cut from $Zr_{48.5}Cu_{51.5}$ as-cast rod	**1**	**2**	**3**	**4**	**5**
Volume fraction, V_f	0%	15%	39%	64%	93%
0.2% Yield strength (MPa)	1680	1670	1610	1520	990
Young's Modulus (GPa)	75	74	67	63	36
Plastic Strain	3.0%	3.4%	4.8%	8.3%	1.8%

The monolithic glassy sample 1 exhibited an elastic-perfectly plastic behavior with limited plastic strain of 3% and yield strength of 1680 MPa. With a low volume fraction of reinforcement (15% in sample 2), the composites showed similar behavior to the monolithic glass, with no significant enhancement of plasticity as well as deterioration of yielding strength. For the samples with higher values of V_f (39% in sample 3 and 64% in sample 4), their stress-strain curves start to show some evidence of more extensive plastic flow (4.8% for sample 3 and 8.3% for sample 4) and work hardening behavior. However, as V_f reached 93% for sample 5, the stress strain profile is much like that of a typical brittle material since the crystalline phase became to dominate the deformation in such a case (**Figure 2. 8**). The results show that moderately higher volume fraction of the reinforcement leads to enhanced compressive plasticity but lowered yield strength, consistent with previous reports [99].

The results also showed that, even in a single as-cast rod, depending on the different cooling history, the different part of the rod will show distinct mechanical behavior upon compression. We note that the optimum plasticity is achieved in Sample 4, with so-called ring-type composite microstructure. Therefore, it suggests that, the ring-typed composite structure is also eligible for stabilizing the shear banding and allows the extensive plastic flow, which is usually achieved in a regular composite structure.

2.4 Conclusions

The unique glass formation around the equiatomic composition in Zr-Cu binary system has been studied. The most salient conclusions have been drawn as follows:

(1) In contrary to the conventional belief that metallic glass is either formed near deep-eutectics through liquid quenching or near the centre of phase diagram by solid-state reaction, we discovered a completely new glass (“intermetallic glass”) formation close to intermetallic composition in the Zr-Cu binary system through liquid quenching. Such unique glass formation becomes feasible because both

the kinetic and thermodynamic conditions for the amorphous formation are favored in the vicinity of the intermetallic composition.

(2) The so-called “intermetallic glasses” were located in a pair, and close to but separated by the intermetallic compound in the centre of the phase diagram. Since almost all the effort in discovering (bulk) metallic glasses through liquid quenching so far is centered around eutectic composition, our finding implies that there are many potential bulk glass formers yet to be discovered in different compositional spaces, particularly near the intermetallics in the centre of phase diagrams. This finding opens an otherwise overlooked arena for locating a new host of metallic glasses (systems) that have potentials for application.

(3) The intermetallic glasses exhibited similar features (e.g. strain softening and serrated flow) in the mechanical responses to the conventional BMGs. The composites with two types of microstructural inhomogeneity induced by varying compositions and cooling history were used as examples to understand the mechanical behavior of glass matrix composites. It is showed that, strain hardening was only achieved in a composite structure with moderately high volume fraction of the reinforcing phases. In addition, the ring-typed composites have shown an enhanced plasticity, similar to the regular composites.

Chapter 3

Statistical effect on strength of BMGs

3.1 Introduction

Because amorphous metals have no long-range structural order, they exhibit different mechanisms of plastic deformation as compared to the typical dislocation-mediated flow mechanisms common in crystalline metals [3]. At room temperature, metallic glasses generally deform through a process of highly localized shearing in narrow bands, as a consequence of their tendency

for strain-softening [86, 149-151]. It is frequently observed that metallic glasses or bulk metallic glasses (BMGs) tend to fail along one dominant shear band under either uniaxial compressive or tensile conditions, exhibiting very little macroscopic plasticity [66]. In the engineering sense, their stress-strain curves resemble those of conventional brittle materials, and so BMGs are often referred to as "brittle", or at least "macroscopically brittle", materials. What is tacitly implied by these labels is the concept of *flaw sensitivity*, where the size of the "flaw" in a homogeneous glass can be in the conventional micron range (as for a pore or inclusion), or may even be intrinsic to the glass structure on the sub-nanometer range. In an unconstrained geometry, once shear localization has begun, the shear softening nature of the glass accelerates deformation through very large strains, and ultimately, failure, particularly under tension. Any flaw in the glass volume (or on its surface) can in principle serve as a facilitator to the process of runaway shear failure. Such strength-limiting flaws may include any stress-concentrators (i.e. voids, inclusions, surface irregularities), or possibly local fluctuations in the chemistry or density (free volume) of the glass structure itself.

The acknowledged flaw sensitivity of BMGs represents a significant problem for their application, and there is a natural approach to address this problem - one that has received virtually no attention to date - is to understand and manage variability in the mechanical properties. As potential structural materials flaw sensitive enough to be termed "macroscopically

brittle", BMGs should display scatter and variability in their mechanical properties, based upon the statistical distribution of flaws. There are many ways to describe the effects of statistically-distributed flaws or defects, such as the Weibull approach commonly used to describe the fracture strength when fracture initiates from a single critical flaw [152, 153]. Weibull analysis has historically been applied to ceramics and brittle metals, and, interestingly, was applied over a decade ago to some metallic glass ribbons [154-157]. There are generally two assumptions [152, 153] on which the Weibull theory is based: (1) fracture will occur at the weakest point within the specimen, and (2) the material is statistically homogeneous at a sufficiently large length scale, i.e. the probability to find a critical flaw in a given volume element is the same as in the overall volume.

Given a relatively consistent casting process, the statistical homogeneity of cast BMGs is expected to be reasonable. Furthermore, because BMGs are flaw sensitive and yield discretely as a shear band is formed, they may be amenable to the weakest link assumption; if there exists a weaker band of material in the specimen, then a shear band should form preferentially there. In these regards, the scatter and variability in the strength of BMG should be describable within the classical Weibull statistics framework. Thus, the problem of flaw sensitivity could in principle be handled by understanding statistical variations in the strength of BMGs. One important aspect of such statistical approaches is the volume scaling effect,

which has not yet been studied in BMGs. Unfortunately, it is not trivial to conduct such studies, because in casting differently sized amorphous ingots, different structures are produced at the sub-nanometer scale, and very different properties result. In this sense, it would be intrinsically difficult to distinguish between a statistical size effect and a latent structural effect on the strength statistics. In this study, we therefore focus only on the statistic effect in single sized samples. The sample size effect on the mechanical properties of BMG will be demonstrated in Chapter 5 of this thesis.

In this chapter, we consider the above approach to address "flaw sensitivity" in BMGs. We begin by first measuring the strength distribution of three Zr-Cu-based BMGs, using Weibull statistics on specimens tested in uniaxial compression. We show that despite their "macroscopically brittle" character, these BMGs exhibit remarkable strength uniformity, comparable to conventional polycrystalline metals. Further, the close correlations between the Weibull modulus, glass forming ability (GFA), and intrinsic plasticity of BMGs will be discussed.

3.2 Experimental procedure

Three glass compositions were chosen for this work: $Zr_{51}Cu_{49}$, $Zr_{48}Cu_{45}Al_7$ ($\approx(Zr_{51}Cu_{49})_{93}Al_7$) and $(Zr_{48}Cu_{45}Al_7)_{98}Y_2$. The former two, Y-free alloys were selected as representatives of nominally "malleable" glasses; they have been reported to form glass in rods with 2 mm (see Chapter 2) and 8 mm [64] in diameter, respectively. The last alloy, containing an additional 2 at.% Y, was selected as representative of nominally "brittle" glasses; the Y addition has been shown to embrittle the $Zr_{48}Cu_{45}Al_7$ alloy without deteriorating the glass forming ability [26].

The three alloys were prepared by arc-melting mixtures of high purity metals in a Ti-gettered high-purity argon atmosphere. Each ingot was remelted at least five times in order to obtain chemical homogeneity. The ingots were then cast into rods (30 mm in length, 1.5 mm in diameter) by water-cooled copper mold suction casting. Because the present study focuses on statistics, many nominally identical samples of the same compositions were required. Accordingly, at least 7 rods of each composition were prepared using the procedures described above. It is important to remember that the data reported below probes uniformity not only within a single casting, but from one batch to the next.

Longitudinal cross-sections of the rods were examined by X-ray diffraction (XRD) using a Bruker AXS instrument with Cu-Kα radiation at 40 kV and scanning electronic microscopy (SEM). The thermal properties were measured by differential scanning calorimetry (DSC, 2920 TA instruments) at a heating rate of 0.33 Ks^{-1}. **Figure 3. 1** shows the XRD patterns of these samples confirming that all these alloys are fully amorphous, at least at XRD resolution. The inset DSC curves show that they have the typical thermal behavior of BMGs such as a distinct glass transition with a large supercooled liquid region (42 K for $Zr_{51}Cu_{49,}$ 63 K for $Zr_{48}Cu_{45}Al_7$ and 72 K for $(Zr_{48}Cu_{45}Al_7)_{98}Y_2$). All have total heats of crystallization of around 56 $J{\cdot}g^{-1}$, similar to the values for their corresponding fully glassy ribbons, which further confirms the fully amorphous nature of these as-cast samples. To reduce the potential effect of structural inhomogeneity (see Chapter 2, section 2.3.2.2), the upper third of each as-cast rod was removed and discarded, and the data were obtained on specimens from the remaining lower portion of the cast rods.

Uniaxial compression testing was conducted at room temperature with a constant engineering strain rate of 10^{-4} s^{-1}. The test specimens were 3.1~3.3 mm in length and 1.5 mm in diameter, providing a nominal aspect ratio of ~2:1 as recommended by ASTM E9-89a (2000) for testing high strength materials. The compression specimens were first sectioned from the cast rods using a Struers diamond cutter, followed by grinding process with a

customized specimen jig to carefully grind the sample into "orthogonal" shape. This sample preparation process not only ensures parallelism of two ends of the specimen to within 10 μm or better, but also guarantees that the ends were exactly perpendicular to the longitudinal axis of the specimen. This process is extremely important to the mechanical tests of BMG samples as will be revealed in the Chapter 4 of this thesis.

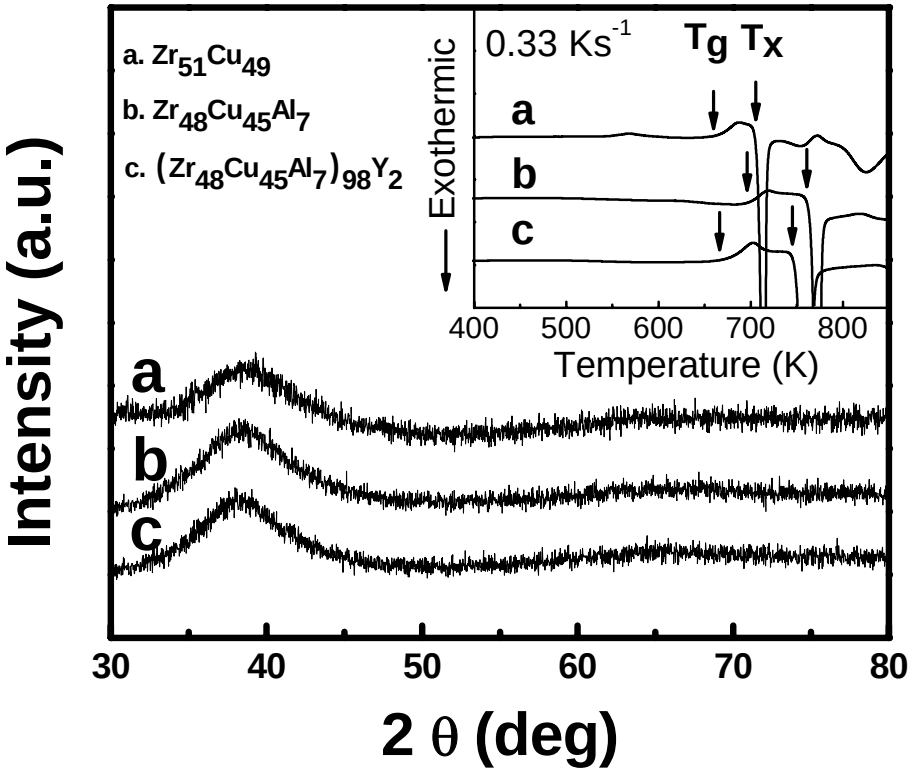

Figure 3. 1 XRD patterns of representative $Zr_{51}Cu_{49}$, $Zr_{48}Cu_{45}Al_7$ and $(Zr_{48}Cu_{45}Al_7)_{98}Y_2$ as-cast rods. The inset shows their corresponding DSC curves, with the glass transition (T_g) and onset crystallization temperature (T_x).

A large number of specimens were tested in compression in order to insure a reliable statistical analysis [158]. The compression samples were sandwiched between two WC bearing blocks and their ends were lubricated by Black MOLY (molybdenum disulfide in a premium grease). Each sample was carefully centered on the loading axis to ensure uniaxial loading, and true applied strains were calculated from the crosshead displacement after correction for machine compliance.

With no strain hardening behavior in BMGs, in this chapter we use the ultimate strength to approximate the yielding strength using for the Weibull analysis.

3.3 Results and Discussion

3.3.1 Weibull statistics of strength

A total of 18 orthogonal samples of the malleable $Zr_{51}Cu_{49}$ BMG were tested, and all the stress-strain curves of $Zr_{51}Cu_{49}$ BMG specimens are shown in **Figure 3. 2**. It was observed that the ultimate compressive strength was quite consistent from one sample to another. All of the values lay within a

remarkably narrow range, from 1630 to 1680 MPa—a variation of only ±1.5% about the mean strength.

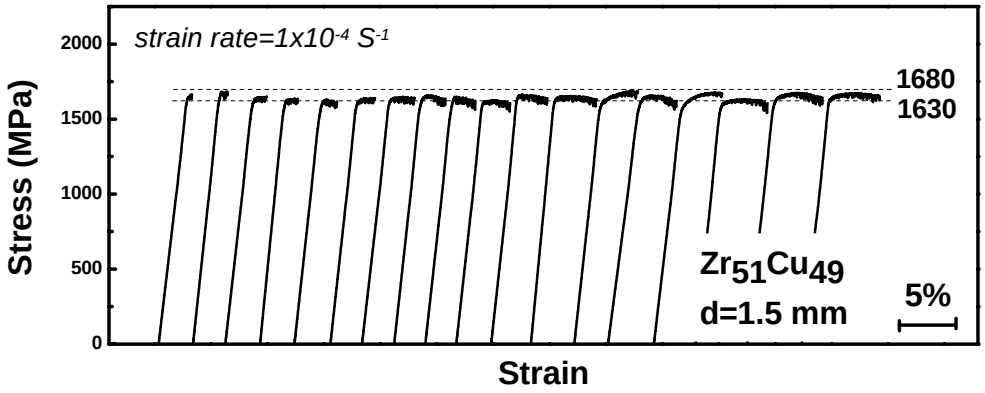

Figure 3. 2 Compressive stress–strain curves of 18 orthogonal $Zr_{51}Cu_{49}$ BMG specimens, offset from one another on the strain axis for clarity of presentation.

Similarly, **Figure 3. 3** shows the stress-strain curves of all the 24 tested samples of $Zr_{48}Cu_{45}Al_7$ BMG. Their ultimate strength variation is still very limited at only ±3% about the mean strength with strength value from 1790 to 1900 MPa. **Figure 3. 4** shows the stress-strain curves of all the 47 tested samples of the more brittle $(Zr_{48}Cu_{45}Al_7)_{98}Y_2$ BMG. Their ultimate strength has a somewhat wider range from 1430 to 1780 MPa—a variation of ±11% from the mean. These measurements as well as some additional properties of the samples are summarized in **Table 3. 1**.

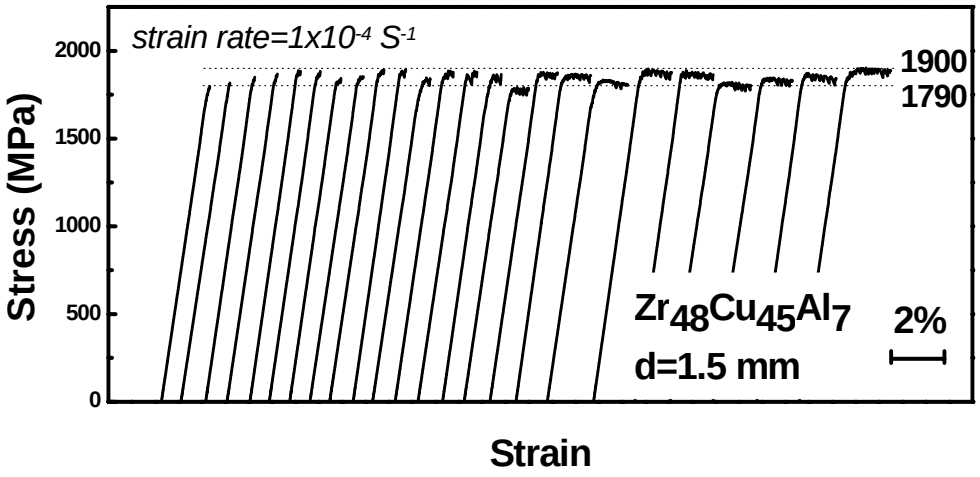

Figure 3. 3 Compressive stress–strain curves of 24 orthogonal $Zr_{48}Cu_{45}Al_7$ BMG specimens, offset from one another on the strain axis for clarity of presentation.

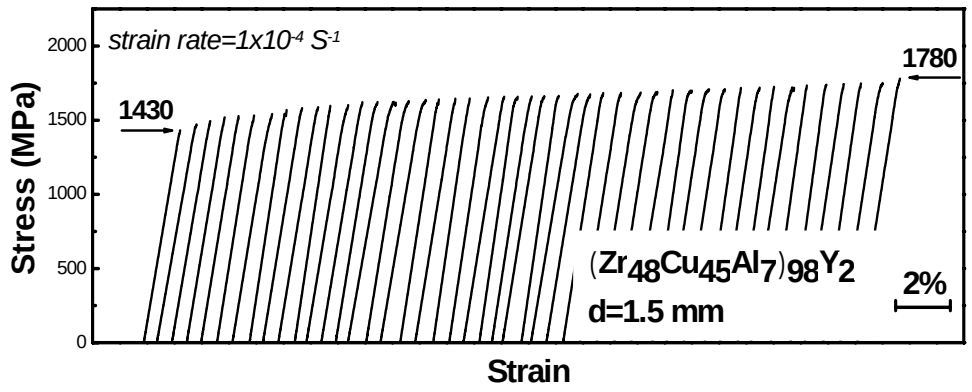

Figure 3. 4 Compressive stress–strain curves of 47 orthogonal $(Zr_{48}Cu_{45}Al_7)_{98}Y_2$ BMG specimens, again displaced on the strain axis for clarity.

Table 3. 1 Summary of the measured mechanical properties of orthogonal $Zr_{51}Cu_{49}$, $Zr_{48}Cu_{45}Al_7$ and $(Zr_{48}Cu_{45}Al_7)_{98}Y_2$ BMG specimens under compression testing.

BMGs	Compressive strength (MPa)	Weibull modulus	Plastic strain	No. of tested specimens
A-$Zr_{51}Cu_{49}$	1630-1680	112	0.5%-4.5%	18
B-$Zr_{48}Cu_{45}Al_7$	1790-1900	73.4	0-1.7%	24
C-$(Zr_{48}Cu_{45}Al_7)Y_2$	1430-1780	25.5	0-0.3%	47

As mentioned in the introduction, the variability of strength in our BMG specimens is expected based on their flaw sensitivity, and may be analyzed in the framework of Weibull statistics. The Weibull equation describes the fracture probability P_f for a given uniaxial stress σ. The so-called "three-parameter" Weibull equation is:

$$P_f = 1 - \exp\left\{-V\left[\frac{(\sigma - \sigma_u)}{\sigma_0}\right]^m\right\} \tag{3.1}$$

where σ_0 is a scaling parameter, m is the Weibull modulus and V is a normalized volume of the tested sample. The parameter σ_u denotes the stress at which there is a zero failure probability, and is usually taken to be zero, allowing a "two-parameter" analysis [159]. For n nominally identical specimens of the same volume, the failure probability P_f of the *i*th one is calculated using the following estimator [160], which is preferred among the various estimators used in the literature [158, 161]:

$$P_{f,i} = \frac{i - 0.5}{n} \tag{3.2}$$

Weibull analysis usually proceeds by linearizing Equation (3.1) as

$$\ln\left[\ln\left(\frac{1}{1-P_f}\right)\right] = \ln V + m\ln\sigma - m\ln\sigma_0 \tag{3.3}$$

Figure 3. 5 (a) shows Weibull plots in the fashion suggested by Equation (3.3) for the $Zr_{51}Cu_{49}$ (line A), $Zr_{48}Cu_{45}Al_7$ (line B) and $(Zr_{48}Cu_{45}Al_7)_{98}Y_2$ (line C) BMGs. In all cases the data is reasonably linear, indicating that the Weibull equation describes the data adequately. Linear least-squares fitting of Equation (3.3) to these data give the Weibull modulus m as 112 for $Zr_{51}Cu_{49}$ (line A), 73.4 for $Zr_{48}Cu_{45}Al_7$ (line B) and 25.5 for $(Zr_{48}Cu_{45}Al_7)_{98}Y_2$ (line C). The corresponding compressive strength-distribution function ($p_f = \partial P_f / \partial\sigma$) is shown in **Figure 3. 5** (b).

The Weibull modulus, m, reflects the degree of variation in the strength of the samples tested, and can theoretically range from 0 to ∞. Weibull moduli for ductile crystalline metals and for brittle engineering ceramic materials are typically of order ~100 and ~5 [162] respectively, where 100 represents a very narrow (and 5 a very wide) dispersion in strength (see **Table 3. 2** for the Weibull modulus data for various materials). Although BMGs are often regarded as macroscopically brittle materials, it is interesting to observe in **Figure 3. 5** that their Weibull moduli are very high—much larger

than those for brittle ceramic materials, and indeed approaching the range for conventional ductile metals.

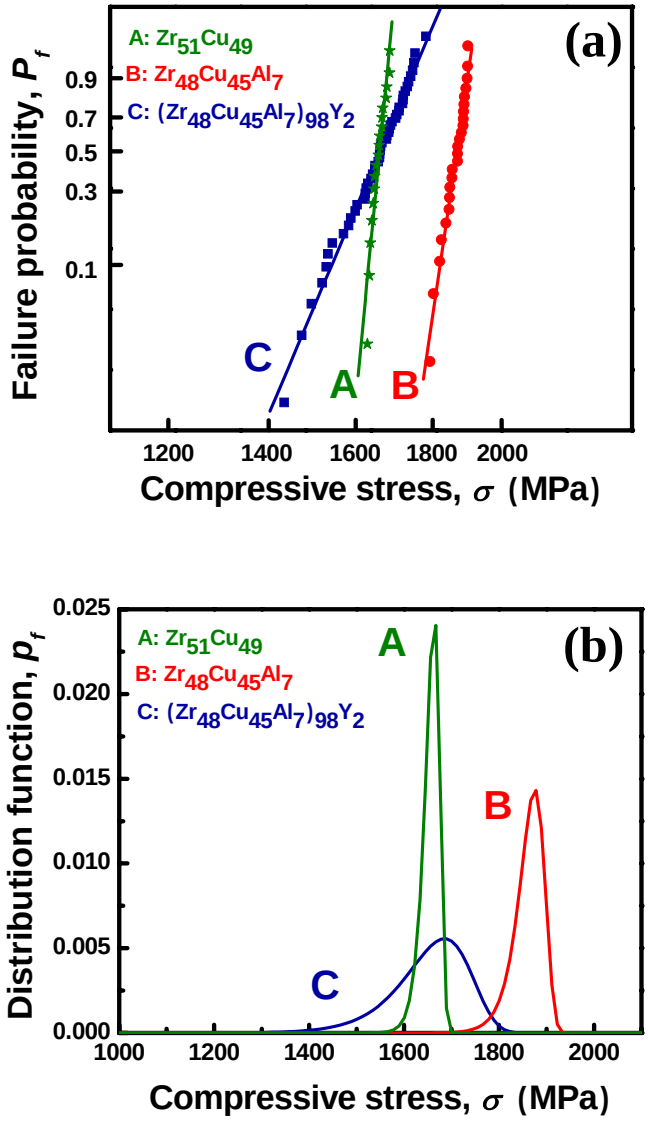

Figure 3. 5 (a) Weibull plots of Zr-Cu-based BMGs under compression. Their Weibull moduli are: (A) 112 for $Zr_{51}Cu_{49}$; (B) 73.4 for $Zr_{48}Cu_{45}Al_7$; and (C) 25.5 for $(Zr_{48}Cu_{45}Al_7)_{98}Y_2$. (b) The corresponding Weibull strength distribution function describes the fraction of the samples that fail at any given compressive stress; note the left hand skew of these distributions.

Table 3. 2 Summary of the Weibull moduli for various materials

Materials	Weibull modulus (m)	Ref.
Low alloy steel (CLA11)	20 - above186	[163]
$Zr_{51}Cu_{49}$ BMG	112	This work
0.2% carbon steel	100	[164]
TiAl alloys	19-95	[165]
$Zr_{48}Cu_{45}Al_7$ BMG (compression)	73.4	This work
$Mg_{71}Zn_{25}Ca_4$	41	[166]
$Zr_{48}Cu_{45}Al_7$ BMG (tension)	36.5	[167]
$Mg_{65}Cu_{25}Gd_{10}$ micropillar	35	[168]
$Mg_{66}Zn_{30}Ca_4$	26	[166]
$(Zr_{48}Cu_{45}Al_7)_{98}Y_2$ BMG	25.5	This work
nanolayer-grained ceramic Ti_3SiC_2	25-29	[169]
light-cured composites	6-14	[170]
engineering ceramics (e.g. SiC, Al_2O_3,Si_3N_4)	10	[171]
flax fibres	3-8	[172]
glass beads	8	[173]
$Ni_{67.5}Cr_{14.4}B_{18.1}$ glass ribbon	8	[155]
$Fe_{40}Ni_{40}B_{20}$ glass ribbon	7.5	[157]
conventional ceramics, chalk, brick, pottery, cement	~5	[174]
$Co_{62.6}Cr_{21.2}W_{1.3}B_{11.6}Si_3C_{0.3}$ glass ribbon	4.5	[155]
rock aggregates	3-4	[175]
railway ballast	2-4	[176]
carbon nanotube	3	[177]
silica sands	3	[178]
quartz sands	2-3	[173]
rice krispies	3.1	[179]
pasta	2.5	[179]

The high Weibull moduli of these BMGs imply good homogeneity and uniformity in the structure of our samples. As amorphous materials, metallic glasses are naturally homogeneous in the sense that they lack microstructure. Furthermore, the processing method used to synthesize the BMG specimens also has some benefits in terms of homogeneity. For example, the amorphous structure "frozen-in" from the liquid requires less volume change, and thus

may sustain fewer solidification defects (such as pores), as compared to solidification of the crystalline counterparts. Additionally, the one-step direct casting process minimizes the possibility of inducing other (non-casting) flaws during processing. These various factors lead to a highly homogeneous structure in our samples and are likely responsible for the high values of Weibull modulus. Such homogeneity may also be promoted by the relatively small size of our castings.

One additional contributor to the high strength uniformity we have measured may be the nature of the experiments: our tests were conducted in compression, in which state only shear flow is initiated. The present statistical data thus speaks only to the sensitivity of these BMGs to *shear band formation*, and do not explicitly allow for the possibility of a competing Mode I (or mixed mode) fracture event. For an intrinsically brittle glass in particular, fracture might be triggered in tensile loading without significant shear banding. In this case it seems possible that the flaw sensitivity may exhibit asymmetry between states of compression and tension, as shear bands and cracks might be differently influenced by the flaw population. This would present an interesting corollary of the documented strength [180, 181], fracture [182, 183], and shear path asymmetries [102] already known in BMGs; we leave this as an interesting topic for future work. Nonetheless, for an inherently malleable glass, where shear localization precedes failure, it seems reasonable to speculate that the same degree of strength uniformity we see

here in compression will also be seen in other modes of loading (including tension).

It is worthy of noting that, followed the present work, the Weibull modulus of $Zr_{48}Cu_{45}Al_7$ BMG under tension has been measured to be 36.5 [167], which is lower than the counterpart value under compression but still noticeably higher compared to those of typical brittle materials. On the other hand, even the typically brittle Mg-based BMG and micro-pillars showed relatively high Weibull moduli of 26 to 41, suggesting good strength uniformity of the BMG material.

The above results on strength statistics also have some important practical implications. For example, the high Weibull moduli of these BMGs indicate that these materials are relatively mechanically reliable, perhaps more so than might be expected in light of their flaw sensitivity. Such reliability is encouraging for the potential use of BMGs as engineering materials. What is more, although our present samples have relatively small diameters (1.5 mm), the Weibull modulus is generally intended to be a size-independent parameter [152, 153]. Thus, absent any size-dependence in the nature of the flaw population due to processing, the same m value would describe the strength variability of large-sized specimens.

3.3.2 Correlations between Weibull modulus, GFA and malleability

In this section, we draw attention to the interesting differences between the currently used three BMGs by first investigating the relationship between their Weibull moduli and the malleability.

These three BMGs are representatives of binary, ternary and quaternary Zr-Cu-based alloys, respectively. As the constituent number increased from two to four in this system, it is of interest to observe that, the Weibull modulus m decreased from 112 to 25.5 monotonically, and the average plastic strain also decreased from 2.5% for $Zr_{51}Cu_{49}$ (**Figure 3. 2**) to about zero for $(Zr_{48}Cu_{45}Al_7)_{98}Y_2$ (**Figure 3. 4**). Therefore, the results suggest a strong correlation between the malleability and the Weibull modulus (and/or strength uniformity) of BMGs. The malleable glasses ($Zr_{51}Cu_{49}$ and $Zr_{48}Cu_{45}Al_7$) exhibit markedly narrower strength dispersion and Weibull moduli higher by a factor of more than three compared to the brittle glass ($(Zr_{48}Cu_{45}Al_7)_{98}Y_2$). The nature of malleable glasses is such that they are capable of distributing shear localization somewhat, and are generally less prone to catastrophic failure [89, 90]. The present results suggest an interesting corollary of this behavior: the malleable glasses may in fact be generally less flaw sensitive than the brittle ones. The plastic characteristics of BMGs are now known to

correlate strongly with their elastic constants (notably the value of the Poisson's ratio [89, 90, 92]); here we propose that Weibull modulus should correlate in a systematic way with Poisson's ratio, and measurements of m are in fact a natural index for the flaw sensitivity of various BMGs with different Poisson's ratios.

The above proposal indicates that a lower m could be obtained for extremely brittle glasses such as Mg- [90, 184] or Fe- [185] based BMGs. It is thus not surprising to observe relatively lower Weibull moduli in Mg-Zn-Ca BMGs [166].

Next we investigated the relationship between the m and GFA in current Zr-Cu-based BMGs. **Figure 3. 6** shows the XRD results for GFA comparison study in three BMGs. The critical size, which is an indicator of GFA, increased from 2 mm for binary glass to 5 mm for ternary glass then to 8 mm for quaternary glass.

The results showed that the GFA of $Zr_{51}Cu_{49}$-based BMGs increased as the constituent number increases, which is in accordance with the confusion principle [186]: the more the element involved, the less the chance of crystallization will occur. Especially in the present system, a reasonably large atomic size mismatch (>12%) between any two constituents is expected with their Goldschmidt atomic radii of 0.128 (Cu), 0.143 (Al), 0.160 (Zr), 0.181 (Y) nm, respectively. This atomic size mismatch is believed to enhance the packing density of the alloys in liquid states and thus benefit the GFA.

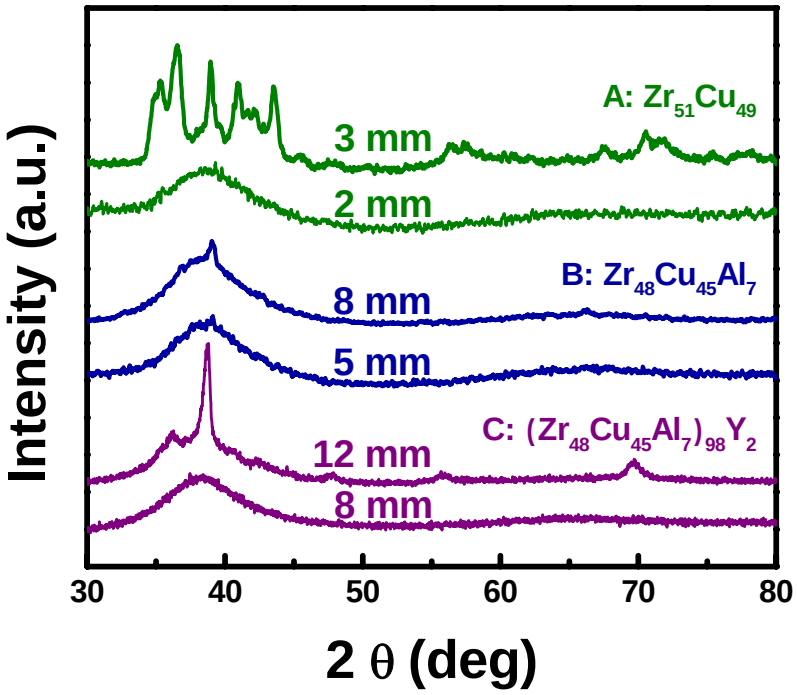

Figure 3. 6 The XRD patterns of three as-cast Zr-Cu-based alloys with different sizes. The critical sizes were found to be 2 mm, 5 mm and 8 mm for $Zr_{51}Cu_{49}$, $Zr_{48}Cu_{45}Al_7$, and $(Zr_{48}Cu_{45}Al_7)Y_2$, respectively.

Figure 3. 7 summarizes the GFA (in terms of critical size), *m* and malleability (in terms of plastic strain) for the three Zr-Cu-based alloys. It was found that m and malleability scales inversely with GFA in this system. The data for conventional oxide glass is added for comparison and further confirmation of such a relationship.

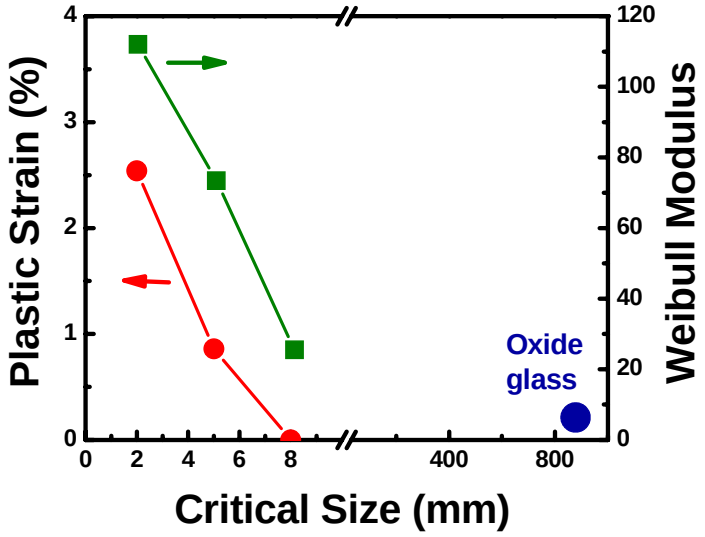

Figure 3. 7 The correlation between GFA (critical size), the plastic strain prior to failure, and Weibull modulus for the three Zr-Cu-based BMGs. The data for oxide glass is also plotted for comparison.

The close correlation between the GFA and the Weibull modulus (and/or malleability) is not unexpected considering that both of them are known to be influenced by the local structural differences (e.g. free volume concentration) and chemical bonding states. For example, a lower GFA usually indicates a lower packing density and higher free volume concentration of the alloy. While the plastic deformation of BMGs is often associated with the free volume [66] in that, at a site with higher free volume content, the individual atomic jumps associated with the macroscopic flow of metallic glass will be favored thus the plastic deformation can be enhanced.

3.4 Conclusions

The flaw sensitivity and mechanical reliability of BMGs have been systematically investigated by performing a statistically significant number of compressive tests on three Zr-Cu-based BMGs. The most salient conclusions have been drawn as follows:

(1) Despite the fact that BMGs exhibit little or no macroscopic plasticity before failure (similar to other brittle materials), we observe surprisingly high uniformity in their compressive strength. Weibull analysis was employed to study the statistical dispersion in strength, giving very high Weibull moduli of about 25 for an intrinsically brittle glass $(Zr_{48}Cu_{45}Al_7)_{98}Y_2$, and near 75 and 112 for two intrinsically malleable glass $Zr_{48}Cu_{45}Al_7$ and $Zr_{51}Cu_{49}$. This high uniformity is encouraging for the use of BMGs in structural applications.

(2) Close correlations between the Weibull modulus, malleability and GFA of BMGs were verified in this system. The results suggested that Weibull modulus should be a natural quantity to distinguish more or less flaw sensitive (i.e. brittle vs. malleable) glasses and should correlate in a systematic way with Poisson's ratio. In addition, the results showed that the GFA scaled inversely with the Weibull modulus and/or malleability in the current Zr-Cu-based system.

Chapter 4

Stress gradient enhanced plasticity in a monolithic BMG

4.1 Introduction

Bulk metallic glasses (BMGs) are of interest due to their superior properties such as high strength and high corrosion resistance. The mechanical behavior of metallic glasses has been extensively studied in recent years. Similar to the amorphous ribbons, flow in BMGs is extremely inhomogeneous at high stresses and low temperatures [66]. The plastic deformation of BMGs is highly

localized into thin shear bands as a result of strain softening, followed by rapid propagation of these shear bands due to lack of structural inhomogeneities [66, 86, 149-151]. As a consequence, the BMGs often exhibited a catastrophic failure along one dominant shear band without macroscopic plasticity both under tension and compression that limits their applications. How to avoid the rapid propagation of shear bands and to generate multiple shear bands thus became a key issue in toughening the BMGs.

Generally, there are two methods to address it. The first one is to introduce a second phase to the monolithic amorphous structure to make a composite material [36, 99, 114-116, 121, 122, 187-195]. The introduction of second phase can induce stress concentration around itself thus promote the initiation of shear bands. The second phase can also act as a constraint to arrest the catastrophic shear failure through the interaction with the initially formed shear bands. The plasticity of BMGs can thus be improved. In this case the second phase can be crystalline phases, metal particles, glassy fibers or even another glass structure. The second approach is to apply a lateral or geometrical confinement to produce a multi-axial stress state in the BMGs, under which the shear band propagation becomes sluggish and multiple shear bands can be triggered [72, 85, 86, 183, 196]. For instance, Bei *et al.* have reported an up to 80% plastic strain in a Zr-based BMG with an aspect ratio of ~0.5 [86].

However, it remains of interest to toughen a monolithic BMG without any lateral confinement despite that a few works have recently focused on the enhanced plasticity in BMGs with high Poisson ratios [89-94]. In this chapter, we will demonstrate that plasticity of BMG can be enhanced by introduction of stress gradient inside sample. This was achieved by specially designing of specimen geometry while maintaining the large aspect ratio of two. Under such designs, multiple shear bands were generated in a Zr-Cu-based monolithic BMG consistently with a large displacement prior to failure. The mechanism for this geometry dependence of deformation in BMG is discussed with finite element analysis (FEA) incorporating the free volume concept through collaborative work.

4.2 Experimental procedure

The glass composition chosen for this work is $Zr_{48}Cu_{45}Al_7$, which has been reported to form glassy rod with 8 mm in diameter [64]. The master alloy was prepared by arc-melting mixtures of high purity metals in a Ti-gettered high-purity argon atmosphere. Each ingot was remelted at least five times in order to obtain chemical homogeneity. The ingots were then cast into rods (30 mm in length, 1.5 mm in diameter) by water-cooled copper mold suction casting.

The fully amorphous nature of as-cast sample was confirmed by both the X-ray diffraction (XRD) scan and scanning electronic microscopy (SEM).

The test specimens were about 3 mm in length and 1.5 mm in diameter, providing a nominal aspect ratio of ~2:1 as recommended by ASTM E9-89a (2000) for testing high strength materials. With a custom-made specimen jig, samples were shaped into three different geometries as shown in **Figure 4. 1**. For simplicity, in the remainder of this article we shall refer to the first one as "*orthogonal*" sample, in which the two base planes are perpendicular to the axis; the second one as "*monoclinic*" sample, in which the two base planes intersect the axis obliquely with an angle of 85 degrees; the third one as "*transitional*" sample since it can be regarded as a transitional geometry between the above two geometries, in which one base plane is perpendicular while the other oblique to the axis with an angle of 85 degrees. Note that all of the tested samples in the current work are of an aspect ratio of 2.

Compression testing was conducted at room temperature with a constant engineering strain rate of 10^{-4} s^{-1}. It was noted that except for the orthogonal sample, the other two samples are incapable of sustaining a uniaxial compressive state of stress. As the deformation in these non-orthogonal samples could be quite inhomogeneous, we use load-displacement curve to compare the different mechanical responses of $Zr_{48}Cu_{45}Al_7$ BMG with three geometries instead of using conventional stress-strain curve.

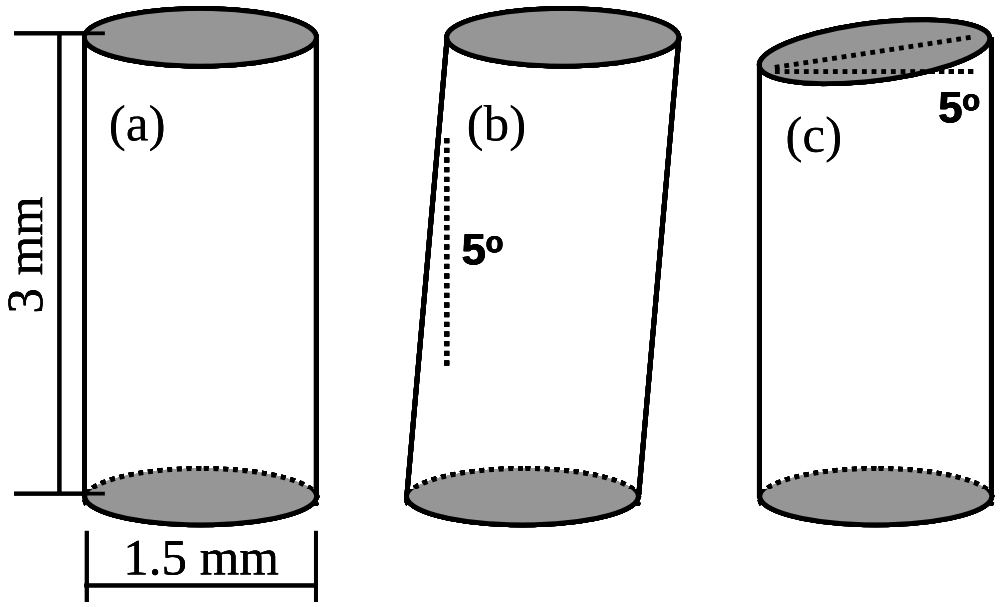

Figure 4. 1 BMG samples with three designed geometries (a) orthogonal, (b) monoclinic, and (c) transitional.

4.3 Results

Figure 4. 2 shows a typical compressive load-displacement curve of $Zr_{48}Cu_{45}Al_7$ BMG with orthogonal geometry under uniaxial compressive loading.

Similar to what reported in the literature [66], the sample failed by one dominant shear band with displacement of only 0.11 mm (plastic strain of 1.3%). Note that the fractured sample shown in the inset remains orthogonal in shape with only a very few shear bands observed (inset of **Figure 4. 2**).

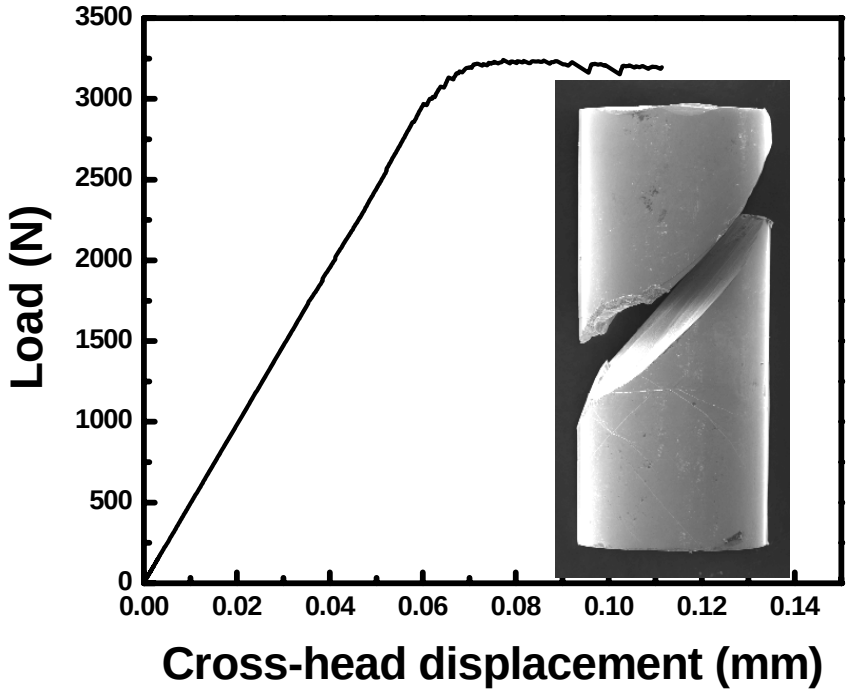

Figure 4. 2 The representative compressive load-displacement curve of $Zr_{48}Cu_{45}Al_7$ BMG with the orthogonal geometry. The inset shows the fractured specimen after very limited plastic deformation (1.3%).

Figure 4. 3 shows the load-displacement curve of the sample with monoclinic geometry. The pop-in typed serrations (inset of **Figure 4. 3**) were not so evident, which is an indication of simultaneous operation of multiple shear bands rather than a discrete shear band nucleation event [87, 197]. It should be noted that the sample during test was gradually tilted from its original geometry (inset of **Figure 4. 3**). The sample did not fracture and the test was stopped at a displacement of 0.48 mm when the tilting induced instability occurred. A number of shear bands were found to be highly localized only on the two corners (indicated as A and B in **Figure 4. 3**).

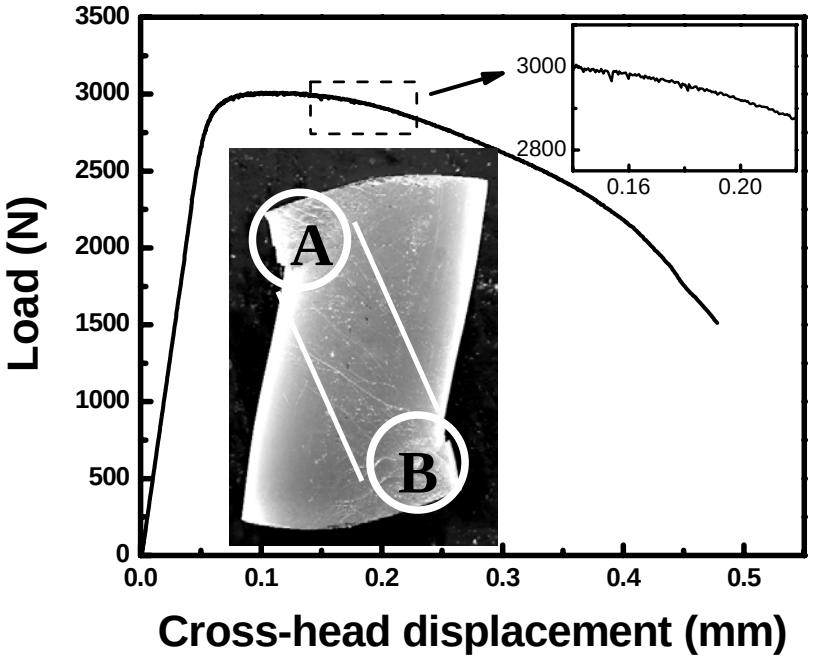

Figure 4. 3 The representative compressive load-displacement curve of $Zr_{48}Cu_{45}Al_7$ BMG with the monoclinic geometry. The inset shows the specimen after deformation. The enlarged area shows slight serrations in the stress strain curve.

Different from the sample with monoclinic geometry which can be considered as symmetric around its center, the sample with transitional geometry which is non-symmetric showed a distinct mechanical response. The sample fractured at a displacement of 0.55 mm as shown in **Figure 4. 4**. A series of typical serrations were observed in the load-displacement curve (inset of **Figure 4. 4**), which indicates a more localized and discrete shear band nucleation event in contrast to the multiple one in the monoclinic sample [87, 197]. The sample fractured until the intense serrations cannot be accommodated further.

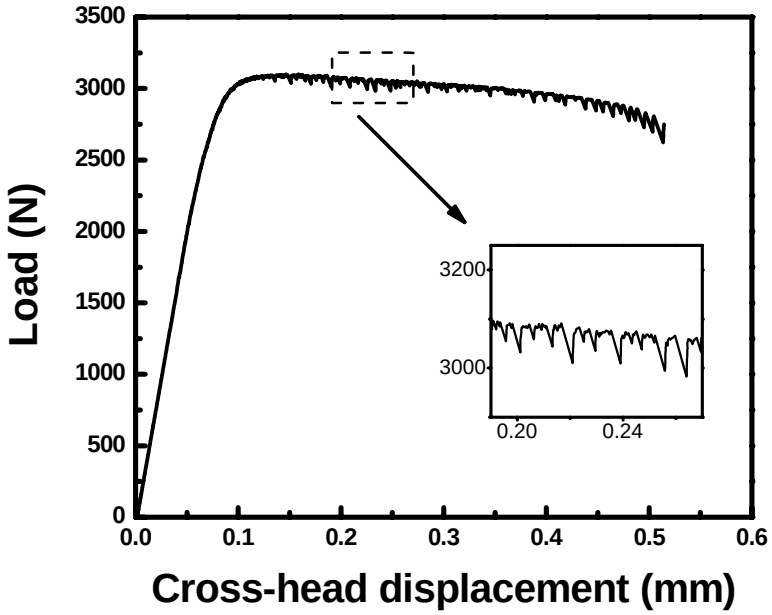

Figure 4. 4 The representative compressive load-displacement curve of $Zr_{48}Cu_{45}Al_7$ BMG sample with the transitional geometry. The enlarged area shows intense serrations in the stress strain curve.

The fractured sample was also tilted from its original geometry (**Figure 4. 5**). Dense shear bands were also observed in the two opposite corners A & B, similar to those of the monoclinic sample but more uniformly distributed. These multiple shear bands are observed with self-branching and cross-linking with each other as demonstrated with arrows in **Figure 4. 5**. Note that there is no shear band observed in the corner C, which indicates a non-uniform deformation for the BMG sample with such a geometry, similar to the monoclinic sample.

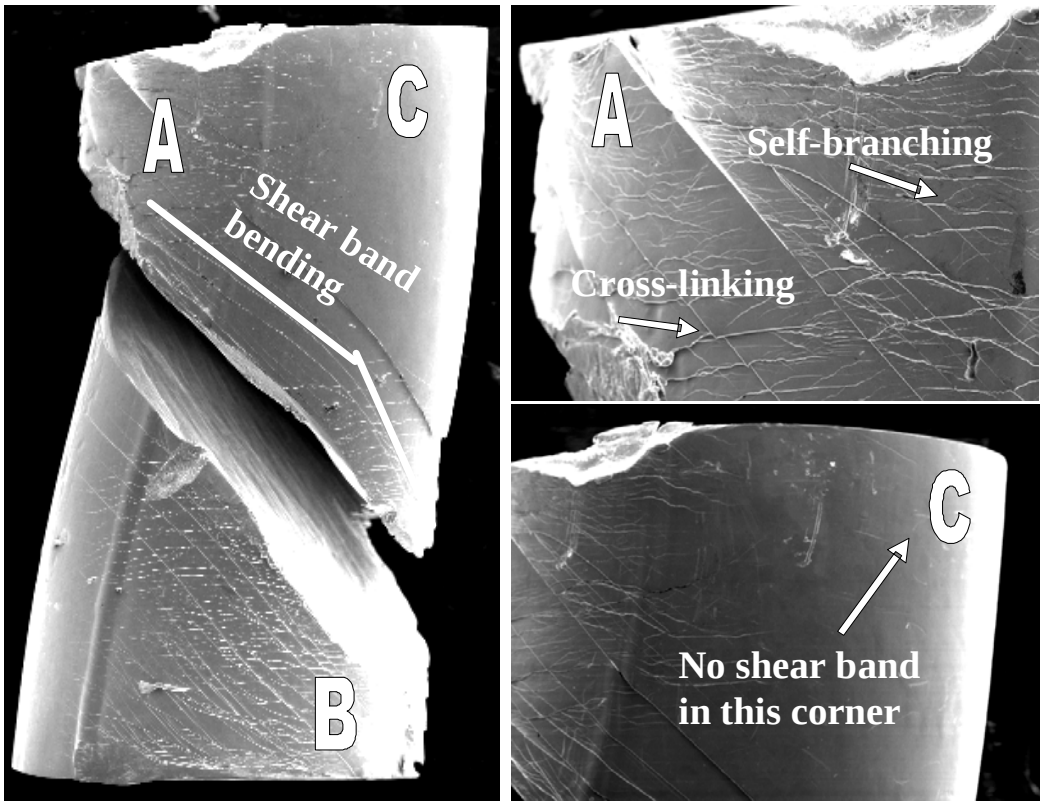

Figure 4. 5 The morphology of fractured $Zr_{48}Cu_{45}Al_7$ BMG specimen with the transitional geometry.

4.4 Discussion

4.4.1 Finite Element Analysis (FEA)†

Finite element analysis was performed to understand quantitatively the deformation mechanisms of the $Zr_{48}Cu_{45}Al_7$ BMG with the three designed

† This simulation part was done by Dr. Zhang ChunYu under Prof. Zhang YongWei's research group (Department of Materials Science & Engineering, NUS) through collaborative work. Permission has been obtained from the authors to allow putting in this thesis for a better illustration.

geometries. Thus far, several constitutive models have been proposed [198-201]. In the present study, the constitutive relation for metallic glasses was based on Spaepen's microscopic model [66] and the finite element (FE) method proposed by Gao [201].

In the constitutive relation, it was assumed that the total deformation can be divided into an elastic part and a (visco-) plastic part,

$$F = F^e \cdot F^p \tag{4.1}$$

where F is the total deformation gradient; F^e is the elastic part and F^p is the plastic part. Historically, additive strain rate decomposition was used,

$$\dot{\varepsilon} = \dot{\varepsilon}^e + \dot{\varepsilon}^p \tag{4.2}$$

where $\dot{\varepsilon}$ is the total strain rate, $\dot{\varepsilon}^e$ is the elastic strain rate and $\dot{\varepsilon}^p$ is the plastic strain rate. The elastic component follows a simple linear elastic equation,

$$\dot{\varepsilon}_{ij}^e = \frac{1+\nu}{E}\left(\dot{\sigma}_{ij} - \frac{\nu}{1+\nu}\dot{\sigma}_{kk}\delta_{ij}\right) \tag{4.3}$$

where E and ν are the Young's modulus and Poisson's ratio, respectively. The plastic component is described by generalizing Spaepen's free volume theory through the von-Mises stress,

$$\dot{\varepsilon}_{ij}^p = 2\upsilon \exp\left(-\frac{\Delta G^m}{kT}\right)\exp\left(-\frac{\overline{v}^*}{v_f}\right)\sinh\left(\frac{\sigma_e}{\sigma_0 + \mu\sigma_{kk}}\right)\frac{s_{ij}}{\sigma_e} \tag{4.4}$$

$$\dot{v}_f = v^* f \exp\left(-\frac{\overline{v}^*}{v_f}\right)\exp\left(-\frac{\Delta G^m}{kT}\right)\left\{\frac{2\alpha kT}{v_f}\frac{3(1-\nu)}{E}\left[\cosh\left(\frac{\sigma_e}{\sigma_0 + \mu\sigma_{kk}}\right) - 1\right] - \frac{1}{n_D}\right\} \tag{4.5}$$

where,

υ	The frequency of atomic vibration
ΔG^m	Activation energy
v_f	Free volume
$v^*, \bar{v}^*$	Effective hard-sphere size of an atom, normalized effective size
s_{ij}	Deviatoric stress, $s_{ij} = \sigma_{ij} - \sigma_{kk}\delta_{ij}/3$
σ_e	von-Mises stress, $\sigma_e = \sqrt{3s_{ij}s_{ij}/2}$
σ_0	Reference stress showing the resisting capability of material to plastic flow. It was defined as $2kT/\Omega$.
σ_{kk}	Summation of the normal stresses
μ	Internal friction coefficient
Ω	Atomic volume
kT	Product of Boltzmann constant and temperature
n_D	The number of diffusive jumps necessary to annihilate a free volume to v^* (1~10)

To account for the pressure-sensitivity of the yield strength of metallic glasses, an internal friction coefficient μ was incorporated into the constitutive law. The friction coefficient incorporates the influence of the hydro-static pressure p (Eqs 4.4 & 4.5) considering $p = -\sigma_{kk}/3$.

The above constitutive model was implemented by writing a user-defined subroutine (VUMAT) embedded into the general-purpose finite element code ABAQUS/Explicit v6.6 (Providence, RI). A plane-stress finite element model was used for simple illustration. It is found that a calibrated

plane-strain model or a three-dimensional model can also reproduce the salient features of the deformation behavior as discussed above. It should be pointed out that the modeling of the material damage was already incorporated in the constitutive model. Detailed modeling of the final fracturing process was not addressed here considering the emphasis of the study was to investigate the plasticity before the final fracture. The typical material parameters [66, 200] used in the calculations are listed in **Table 4. 1**.

Table 4. 1 Critical material parameters used in the FEA

Parameter	**Symbol**	**Value**
Young's modulus	E	100 GPa
Poisson's ratio	ν	0.30
Reference stress	σ_0	50 MPa
Internal friction coefficient	μ	0.01
Normalized initial free volume	$v_f / \bar{v}^*$	Randomly chosen between 0.03~0.04

Based on the constitutive model, finite element analysis on three types of specimens shown in **Figure 4. 1** under compressive loading was conducted. **Figure 4. 6** shows the compressive load-displacement curves of $Zr_{48}Cu_{45}Al_7$ BMG with three designed geometries calculated by FEA.

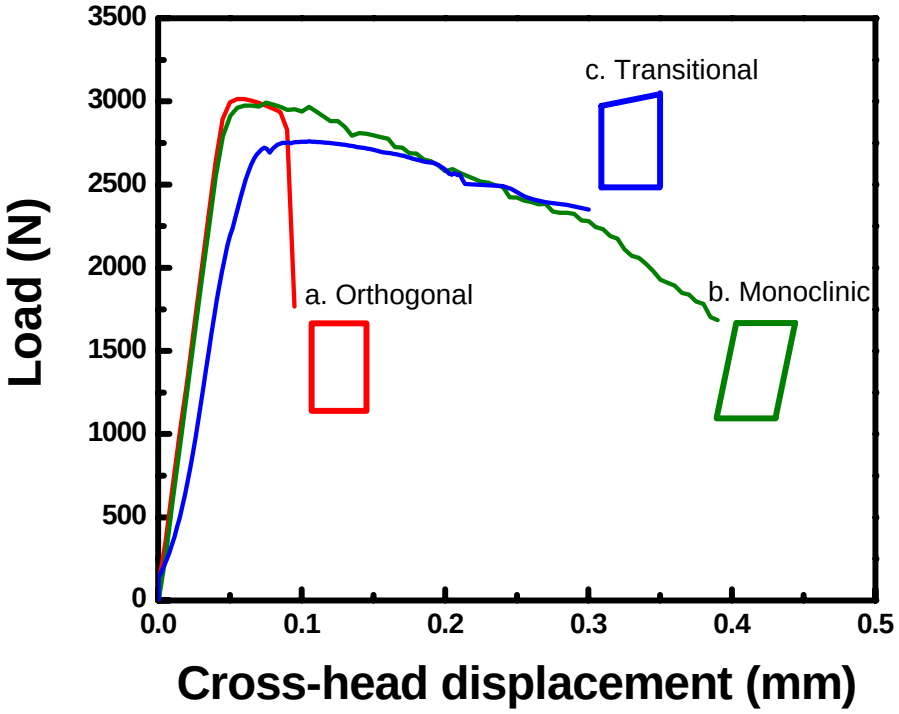

Figure 4. 6 Compressive load-displacement curves with three designed geometries simulated by FEA.

The orthogonal sample exhibited a typical brittle fracture with a displacement less than 0.1 mm. In great contrast, identical alloy with the other two geometries did show much larger displacement prior to failure: 0.39 mm for monoclinic sample and 0.30 mm for transitional sample. The simulation results agreed well with our experimental observations for all the three samples, indicating an adequate description of microscopic deformation and failure mechanism of BMGs by the free volume model and the current FE method.

Our constitutive model certainly has limitations and some of the materials parameters might not be precisely selected. For example, we have chosen a conservative value of 0.30 for the Poisson's ratio of $Zr_{48}Cu_{45}Al_7$ BMG. The real value was not measured and might be around or larger than the critical value of 0.31-0.32 [90] for a malleable glass considering it only has limited plastic strain. The effect of Poisson's ratio on the deformation behavior of the present three structures is yet to be studied. However, our simulation results have revealed that even with this conservative value, the BMG sample with monoclinic and transitional geometries do show much larger deformability (and multiple shear bands) conforming to the experimental observations. Hence it is reasonable to expect that with a higher Poisson's ratio this geometrical effect could be even more evident and beneficial.

4.4.2 Stress gradient in early stage

The distinct Mises stress distributions of sample with three different geometries *in early stage* (a total cross-head displacement of 0.03 mm) are shown in **Figure 4. 7**: nearly uniform stress for orthogonal sample, localized stress in two opposite corners A & B for monoclinic sample, and localized stress in only one corner B for transitional sample. Quantitatively, we

measured the Mises stress distribution along the sample width direction at the position of 0.5 mm away from the bottom surface (**Figure 4. 7**). The stress gradient was roughly estimated by the ratio of the stress variation to the mean stress. The normalized variations were about 1.3% for orthogonal sample, 15% for monoclinic sample, and 98% for transitional sample in this early stage (**Figure 4. 8**).

It is evident that the stress gradients of the monoclinic sample and the transitional sample are much larger than that of the orthogonal sample. On the other hand, a high strength uniformity of $Zr_{48}Cu_{45}Al_7$ BMG has been recently reported under both compressive (see Chapter 3) [202] and tensile [167] conditions. Under compression, for example, the yield strength variation of $Zr_{48}Cu_{45}Al_7$ BMG was only ~3%, which can be considered as the allowable stress variation for the initiation of shear band. With much larger stress gradient as in monoclinic and transitional samples, the initiation of shear bands and the subsequent propagation will be largely restricted, as will be revealed in the following analysis.

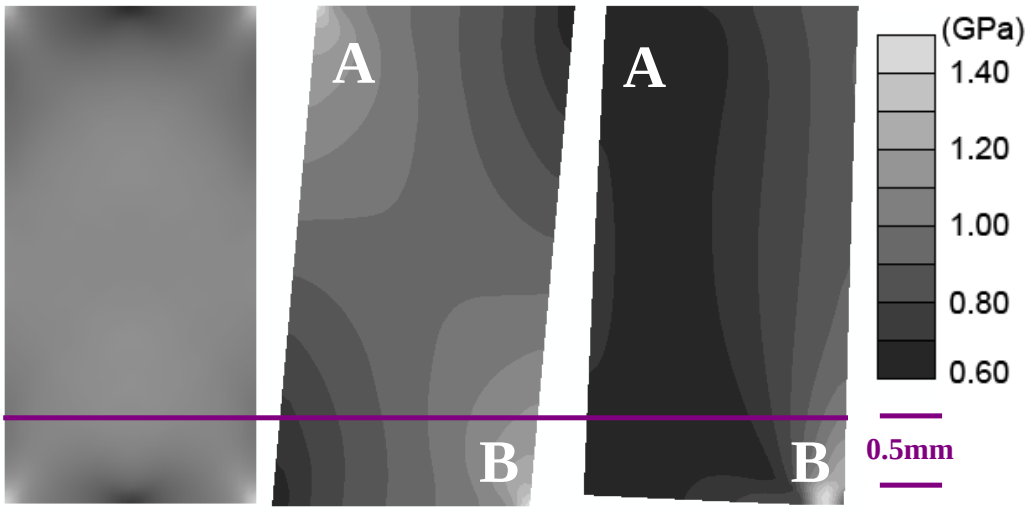

Figure 4. 7 The Mises stress distribution of sample under compression with different geometries at a total cross-head displacement of 0.03 mm.

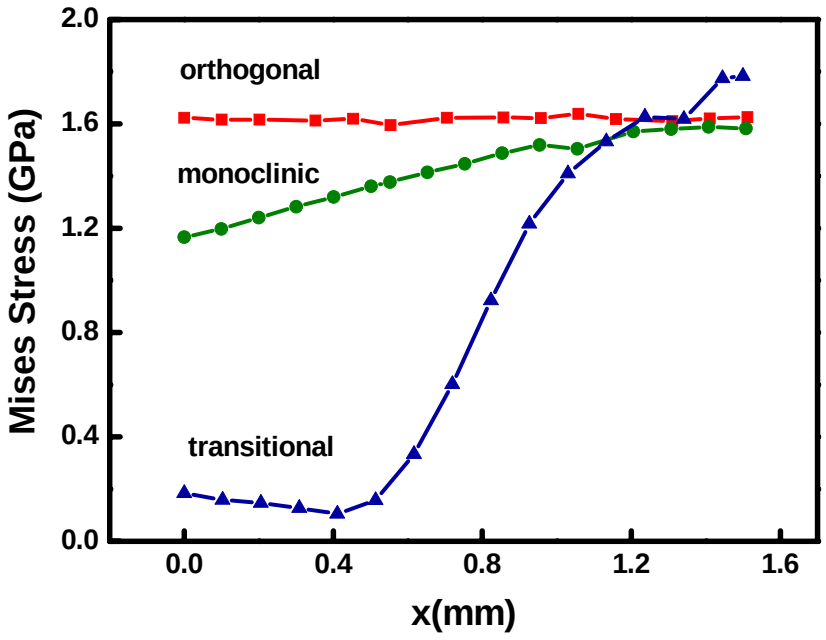

Figure 4. 8 The quantitative stress gradients along the sample width direction at the position 0.5 mm away from the bottom surface.

4.4.3 Shear band initiation and proliferation

4.4.3.1 Orthogonal geometry

Figure 4. 9 shows the shear bands evolution in the orthogonal sample predicted by the FEA. It has been observed that once the free volume exceeded a critical value, it increased abruptly and formed *shear localizations*[†] (dark region). Subsequently, the localized regions lost the bearing capability to form a shear band. Once formed, however, the shear band propagated very quickly through the whole section of sample in a self-catalyzed mode as a result of strain softening. With no such a mechanism to impede this process, the orthogonal sample exhibited a typical macroscopically brittle fracture.

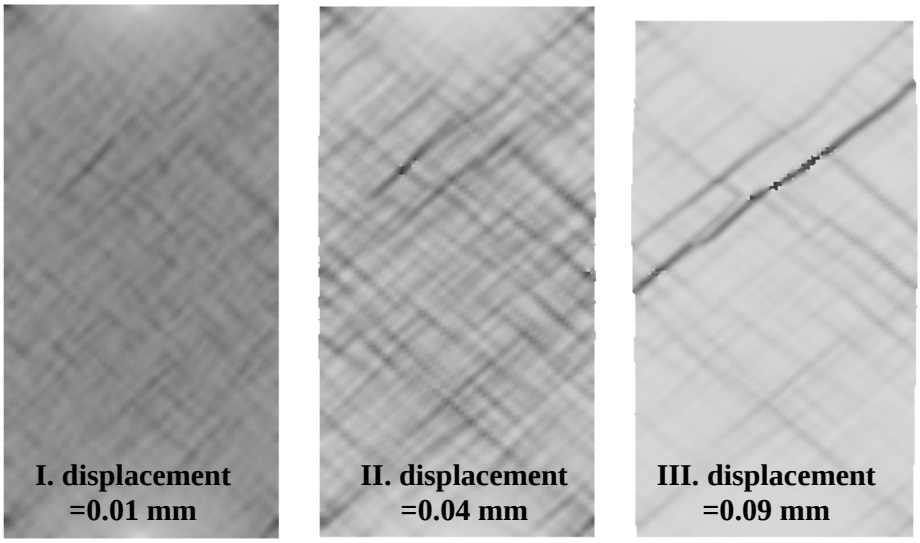

Figure 4. 9 shows the shear bands evolution in the orthogonal sample predicted by the FEA.

[†] We refer to "shear localizations" as severed deformed volume in which large shear strain exists. The shear localizations can be regarded as the precursor of a shear band.

4.4.3.2 Monoclinic geometry

Figure 4. 10 shows the shear band evolution in the monoclinic sample predicted by FEA.

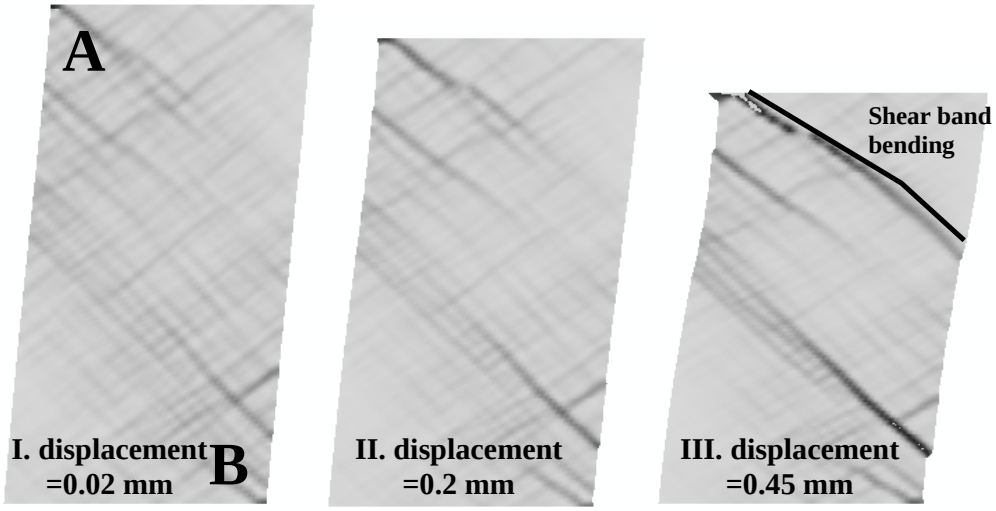

Figure 4. 10 shows the shear bands evolution in the monoclinic sample predicted by the FEA.

Unlike the orthogonal one, in which the uniform stress (**Figure 4. 8**) induced evenly-distributed shear localizations (**Figure 4. 9**), the shear localizations of the sample with monoclinic geometry were trapped in corners A & B (**Figure 4. 10**) due to the stress concentration in these regions (**Figure 4. 8**). With the stress gradient, the rapidly decreased stress in neighboring elastic regions (**Figure 4. 8**) prohibited the initiation of new shear band there and the rapid propagation of the existing shear bands throughout the whole sample as the BMG with orthogonal geometry did. To carry the further deformation,

new shear bands were forced to initiate. This is the reason why a high density of shear bands was observed only in the region A & B, consistent with the experimental observations (**Figure 4. 3**). It is clear that the shear off-sets created by multiple shear bands will tilt the sample during the loading, and the tilting will change the deformation to a more localized condition in corner A and B. This will in turn promote the shear band nucleation in these areas and prevent the shear band propagation which leads to the catastrophic failure. At the final stage due to the large tilting from orthogonality, the sample cannot keep balance anymore and this structural instability made it lean to the platens without fracture. It was noted that the results are highly repeatable. We have prepared more than five identical samples and they all showed a very large displacement without failure.

4.4.3.3 Transitional geometry

Figure 4. 11 shows the predicted shear bands evolution in the sample with transitional geometry. With this non-symmetric geometry, the formed shear bands were highly localized only in the corner B in the early stage (**Figure 4. 11** I) and propagated gradually toward the opposite corner A (**Figure 4. 11** II). The distribution of shear localizations were between the above two cases (i.e., uniform distribution for orthogonal geometry, and symmetrical localization

in region A & B for monoclinic geometry). Again, the stress gradient shown in **Figure 4. 8**, from region B to A in this case, imposed a constraint to against the initiation of new shear band where the yielding stress was not reached and the rapid propagation of existing shear bands thus arresting the sudden failure.

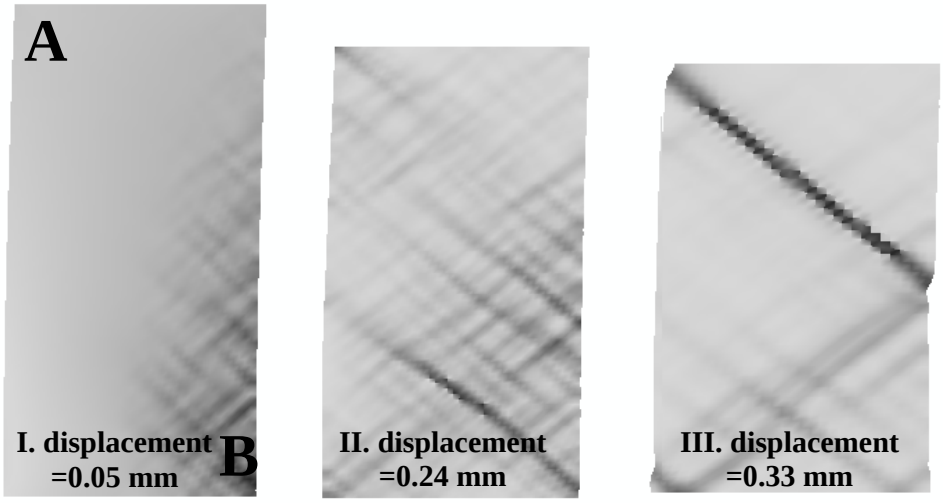

Figure 4. 11 shows the shear bands evolution in the transitional sample predicted by the FEA.

We have also noticed both experimentally and numerically that, with this transitional geometry, the deformation of BMG is sensitive to the initial configurations such as the angle between the sample and the platen. Different failure modes may appear depending on this configuration. The sample corner in contact with the platen failed easily and this may influence the subsequent deformation of the whole body. Thus only one in five samples

showed such a large displacement prior to failure while others failed catastrophically similar to that of orthogonal sample.

The above results revealed that owing to the unique shear banding event and high strength uniformity of BMG, multiple shear bands can be generated in a monolithic BMG by introducing an internal stress gradient which could be geometry-dependent. As multiple shear bands have been widely appreciated as the key to toughen BMGs, we proposed herein the concept of "stress gradient enhanced plasticity" for alleviation of the catastrophic failure of BMGs by specially designing structures or components in which a large stress gradient exists. A recent report [203] on shot-peening induced residual compressive stress to toughen metallic glass can be regarded as another example. We further note that this concept should not be limited to the two non-orthogonal geometries, namely "monoclinic" and "transitional" as in the present work. In addition, the desired stress gradient can also be obtained by loading mode such as bending and indentation. It is often observed that, the shear bands were arrested near the neutral axis during bending [74, 204]. Under the bending load, the stress would reach the maximum at both the tensile and compressive sides, and decrease linearly along the thickness direction from surface to the neutral axis. Therefore, a large stress gradient was present and symmetrically located at the both sides of neutral axis. As expected, the shear bands originated from the surface and were arrested near the neutral axis, as noticed by Conner *et al.* [74, 204]. In

some sense, the currently reported multiple shear bands in the non-orthogonal samples can be regarded as a consequence of confinement in terms of non-uniform deformation. However, our method/concept is distinguished from other confined tests [72, 85, 86, 183, 196]. These samples have low aspect ratio whereas our samples have a normal aspect ratio of 2, offering more practical significances.

Unlike crystalline metals, the BMGs do not exhibit strain hardening. Instead, they show a tendency of strain softening [86]. Once the shear band formed often from a weak point, it will propagate through the whole body very quickly and leads to the catastrophic fracture. If this propagation process was slowed down or prohibited, the catastrophic failure can be alleviated or even avoided. To introduce a ductile crystalline phase to combat with the brittleness of BMGs has thus been of great success. Similarly, to vary the stress distribution in order to evoke a large stress gradient in the whole sample volume could be another effective method as established in this work. However, the former method usually sacrificed more or less the yield strength for the plasticity due to the intervention of soft crystalline phases [99, 188], while our method can help maintain the high strength of BMG sample. What is more, this "stress gradient enhanced plasticity" concept should be independent of alloy systems. As long as the material failed by this shear banding process, it should be applicable although a varied degree of benefit may depend on the intrinsic malleability of this material [202]. Further, for an

inherently malleable glass, where shear localization precedes cracking [76], it seems reasonable to speculate that this method could also help in tension similar to the case of compression.

4.4.4 Curved Shear band path and interaction of shear bands

Owing to the tilting of the monoclinic and the transitional samples during deformation, the direction of the stress as well as the stress gradient keeps changing. As a result, the shear band was developed along a curved path (**Figure 4. 5** and **Figure 4. 10**). Considering the curved path extended the crack propagation distance, the final failure of the sample was thus delayed. On the other hand, the complex stress state of the monoclinic and the transitional samples may lead to shear band branching and cross-linking (**Figure 4. 5**). The branched and cross-linked shear bands prohibited the rapid propagation of the one dominant shear band. Therefore, besides the stress gradient, both the curved shear band path and the interaction of shear bands may also contribute to the enhanced plasticity.

On the other hand, this curved shear band path could be promoted by the bending stress, which is induced by the shear offsetting. As is widely appreciated during the testing of single crystals oriented for single slip,

deformation on a plane leads to a loss of symmetry and as a result, bending load can be developed after some amount of plastic strain has developed. Such effects have been noted explicitly by Sergueeva *et al.* in the case of BMGs [205]. In the present experiments we did use lubricant to facilitate the lateral sliding along the compression platen surfaces to minimize this effect. However, we did not employ a spherical seat capable of permitting additional translation. Therefore, especially in monoclinic and transitional samples, it is anticipated that the unreleased bending stress should contribute to the bending of existing shear bands as well as the change in direction of newly initiated shear bands, although this effect could be minor.

4.4.5 Application of stress gradient strategy in a brittle BMG

Another feasible sample geometry to evoke such a stress gradient is the pyramid structure. We have adopted this strategy in an intrinsically brittle $(Zr_{48}Cu_{45}Al_7)_{98}Y_2$ glass, which exhibited no macroscopic plasticity under compression with normal aspect ratio of 2 (**Figure 4. 12**) [202].

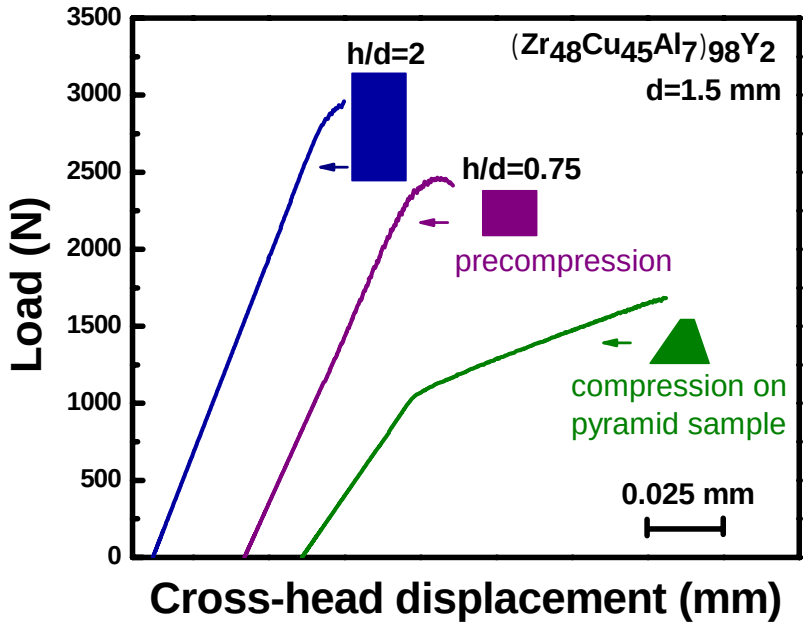

Figure 4. 12 The typically brittle $(Zr_{48}Cu_{45}Al_7)_{98}Y_2$ BMG with a pyramid geometry shows good deformability after yielding. The load-displacement profiles of the orthogonal BMG sample with aspect ratio of 0.75 and 2 are also plotted for comparison.

The pyramid structure was produced by fracturing off the two corners of the orthogonal sample with aspect ratio of 0.75 through precompression (**Figure 4. 13** (a)). This pyramid sample was then loaded in the compression apparatus. A much larger displacement prior to failure was observed in its load-displacement curve (**Figure 4. 12**). The large permanent deformation can also be evidenced by comparing the sample morphology before and after test (**Figure 4. 13** (a) and (b)). A large number of shear bands with semicircular

path were observed on the top of the sample surface, while no shear bands on the bottom (**Figure 4. 13** (b) and (c)).

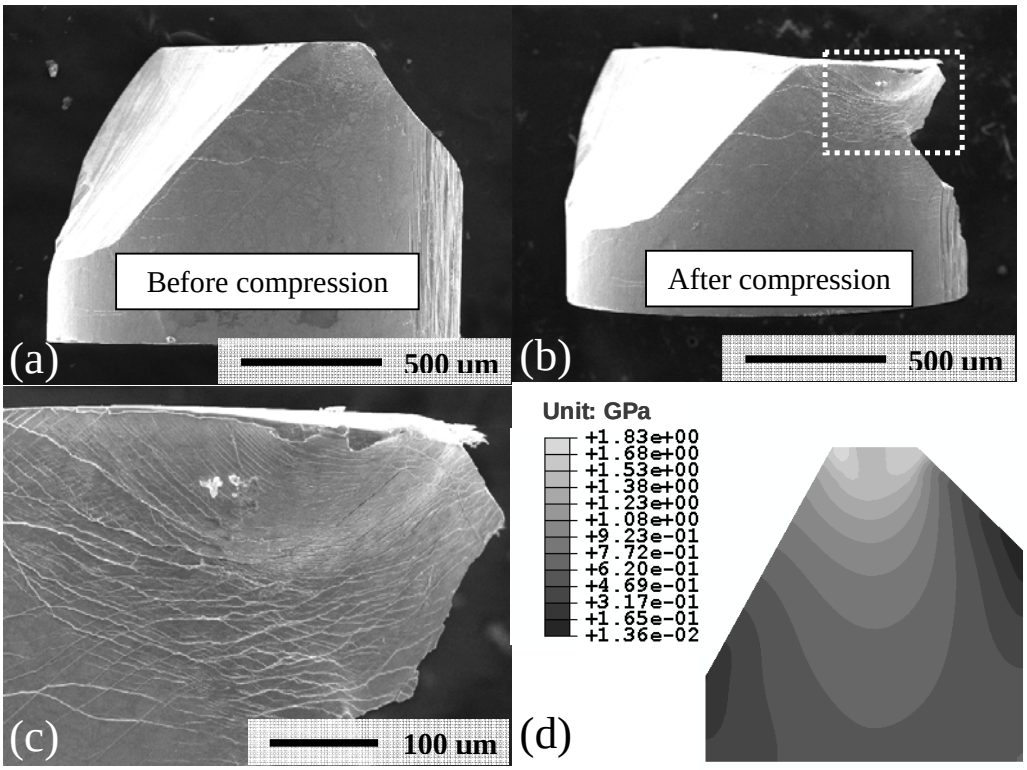

Figure 4. 13 The morphology of pyramid $(Zr_{48}Cu_{45}Al_7)_{98}Y_2$ BMG sample before (a) and after (b) compression. Multiple shear bands with semicircular trajectories were observed in the top of the deformed pyramid sample surface (b), as shown at high magnification in (c). The FEA results suggest that the stress gradient (d) present in the pyramid sample accounts for the enhanced plasticity in this otherwise brittle glass.

This improved plasticity as well as the semicircular path of shear bands should be attributed to the stress gradient, which is present in the pyramid sample. As shown in **Figure 4. 13** (d), the Mises stress distribution in this pyramid sample was found to be characterized with a semicircular contour

map. As discussed earlier, due to the high strength uniformity of BMG, the initiation and propagation of shear bands were largely constrained by the stress gradient. Therefore, even the "brittle" Y-contained BMG can undergo such a large displacement without catastrophic failure. These results further illustrate the concept of "stress gradient enhanced plasticity" in BMGs.

4.4.6 Geometry-sensitive plasticity of BMGs

The current work suggested that the deformation of BMG was highly sensitive to the sample geometry. It was noted that the samples with the monoclinic and transitional geometries were easily to be shaped during the sample preparation especially when the sample was in small dimensions. We have also identified several examples [190, 206, 207] on the deformation of BMG composites in the literature that the features of stress-strain curves (or load-displacement curves) and sample morphology after testing are very similar to those of monoclinic and transitional geometry samples observed in the present work. Thus, it is suggested that special care should be taken in sample preparation and alignment in testing to avoid otherwise misinterpretation of inherent plasticity, as implicitly pointed out in our earlier work [202]. To obtain extensive plasticity in an orthogonal BMG sample is still a challenge in this stage.

4.5 Conclusions

The geometry dependence of deformation in BMGs has been systematically investigated, both by experiments and simulation. The most salient conclusions have been drawn as follows:

(1) The present work revealed that owing to the unique shear banding event and the high strength uniformity, multiple shear bands can be formed in a monolithic BMG by introducing an internal stress gradient, which could be geometry-dependent. The "stress gradient enhanced plasticity" concept was proposed and illustrated using non-orthogonal samples (monoclinic, transitional, and pyramid structures). But it should not be limited to these non-stable structures only. It has been revealed that *non-uniform* deformation induced by the stress gradient affects the nucleation and restricts the propagation of shear bands. Our results suggest that by specially designing component geometry, the monolithic glassy alloys could be deformed plastically, which will alleviate the concern of catastrophic failure of BMG as an engineering material.

(2) The deformation of BMGs was found to be highly sensitive to the sample geometry and the initial configuration of testing. With a standard orthogonal geometry the Zr-based BMG typically fractured

catastrophically with a *single shear band*. In great contrast, by slightly modifying the sample geometry while maintaining the sample aspect ratio of 2, the BMG did show extensive misleading plastic strains with *multiple shear bands*. It is suggested that special care should be taken in sample preparation and alignment in testing to avoid any misinterpretation of inherent plasticity of BMGs.

(3) The finite element analysis based on the "free-volume" model was used to ratify, and more importantly, to quantify the degree of stress gradient and explain the highly geometry-sensitive plasticity of BMGs. The precise capture of the shear bands formation and the reproduction of the load-displacement profiles by FEA have suggested an adequate description of microscopic deformation and failure mechanism of BMGs.

Chapter 5

Size-dependent "malleable-to-brittle" transition in a BMG

5.1 Introduction

Bulk metallic glasses (BMGs) are of interests owing to their great potential for engineering applications [94, 123, 168, 202, 208]. The as-cast glassy structure should be characteristic of a given cooling rate [56, 209], which is inherently distinct for different sized BMG samples. In general, a smaller sample size with a corresponding higher cooling rate will induce more free volume and a

larger degree of structural disordering in the as-quenched amorphous alloys [210, 211]. As a consequence, smaller samples should have higher malleability [112, 113]. For instance, Huang *et al.* have recently reported a "smaller is softer" trend in Ti-based BMGs [113]. Their interpretation was in accordance with the annealing induced embrittlement in metallic glasses [212-214]. The "size effect" described above is basically structural in nature. On the other hand, the intrinsic structural length scale in a monolithic BMG is generally believed to be of atomic dimensions or sub-nano scale associated with short- and medium-range orders or free volume. For most mechanical tests (e.g. tension, compression and bending) however, the sample sizes are much larger than this scale therefore the size dependence of mechanical properties in BMGs is not expected [76].

Further, from engineering consideration in which larger component is desirable, it is therefore essential to understand the mechanical properties of larger sized BMGs. Owing to the inherently different cooling history, the latent structural effect could make it unreliable to describe the mechanical behavior of large specimens with those obtained from small specimens.

In this chapter, we address the above mentioned sample size effect issues on strength and malleability by carrying out a series of compression tests on a Zr-based BMG with various sample sizes. Especially, with low temperature annealing to minimize the free volume differences among different sized BMG samples, we discovered a sample size-dependent

"malleable-to-brittle" transition in a Zr-based BMG. We attribute this transition mainly to the geometrical size effect rather than the structural effect. Accompanied with this transition, the strength of BMG also exhibited a sample size dependence, which will be discussed by both the flaw sensitivity and free volume effects. Our results point out the needs to identify the critical sample size for the "malleable-to-brittle" transition in BMGs, especially under engineering consideration.

5.2 Experimental procedure

The composition chosen for this work is $Zr_{48}Cu_{45}Al_7$ [64]. The ingots with size from 1.5 mm to 4 mm in diameter were prepared by copper mold casting method. A large number of specimens were prepared in order to ensure a reliable statistical analysis [158]. Low temperature annealing, also known as structural relaxation was performed to bring the quenched glass approaching the equilibrium glassy state with annihilation of the excess free volume [209]. To avoid any possible crystallization, the annealing treatments were conducted for 30 min at temperature of 673 K (which is lower than their glass transition temperatures, T_g). The annealing was performed in a furnace after placing the samples inside a vacuum-sealed silicate tube. The thermal

properties were measured by differential scanning calorimetry (DSC) at a heating rate of 0.33 Ks^{-1}. **Figure 5. 1** shows the glass transition part of the typical DSC scans of the BMG samples with 1.5 and 4 mm in diameter under as-cast and annealed states. The corresponding thermal analysis data is listed in **Table 5. 1**.

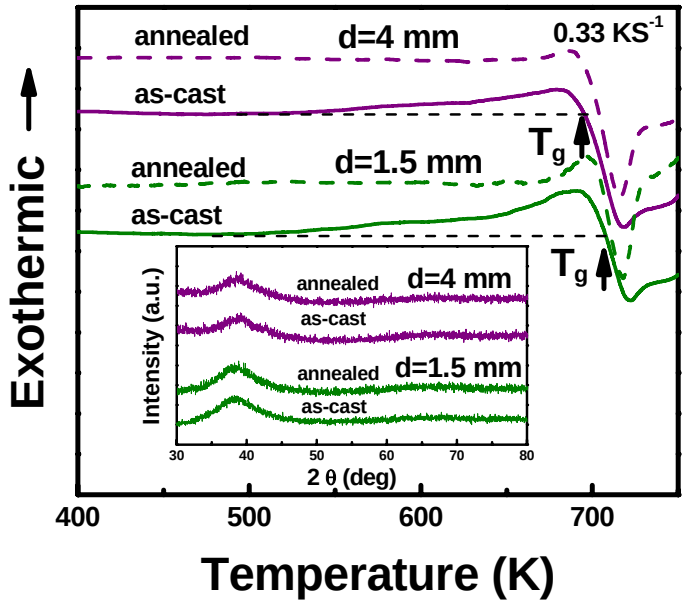

Figure 5. 1 Part of DSC traces of representative $Zr_{48}Cu_{45}Al_7$ rods under as-cast and annealed states. The XRD patterns shown in the inset verified the fully amorphous structure of samples studied.

Table 5. 1 Thermal properties of the representative $Zr_{48}Cu_{45}Al_7$ as-cast and annealed rods obtained from their DSC measurements. ΔH_r denotes the exothermic heat for structural relaxation.

Sample size (mm)	ΔHr as-cast (Jg^{-1})	ΔHr annealed (Jg^{-1})	Tg (K)
d = 1.5	5.8	0.9	706
d = 4	3.4	0.5	695

It has been proposed that the enthalpy obtained by integrating the heat flow ΔH_r just before the glass transition region is proportional to the annihilation of excess free volume ΔV_f [215]. The ΔH_r was 5.8 and 3.4 Jg^{-1} for 1.5 mm and 4 mm samples, respectively. This indicates quantitatively that the smaller sample contained more free volume than that of the larger one in the as-cast state. After annealing, the ΔH_r was 0.9 and 0.5 Jg^{-1} for 1.5 mm and 4 mm samples, respectively, suggesting a substantial reduction in the free volume concentration in both annealed samples. The fully glassy structure of all the samples was ascertained by X-ray diffraction (XRD) as shown in the inset of **Figure 5. 1**. Uniaxial compression testing was conducted at room temperature with a constant engineering strain rate of 10^{-4} s^{-1}. The test specimens were prepared to achieve a nominal aspect ratio of ~2:1.

5.3 Results and Discussion

5.3.1 "Malleable-to-brittle" transition

The representative stress-strain curves of as-cast samples with diameters from 1 to 4 mm are shown in **Figure 5. 2** (a).

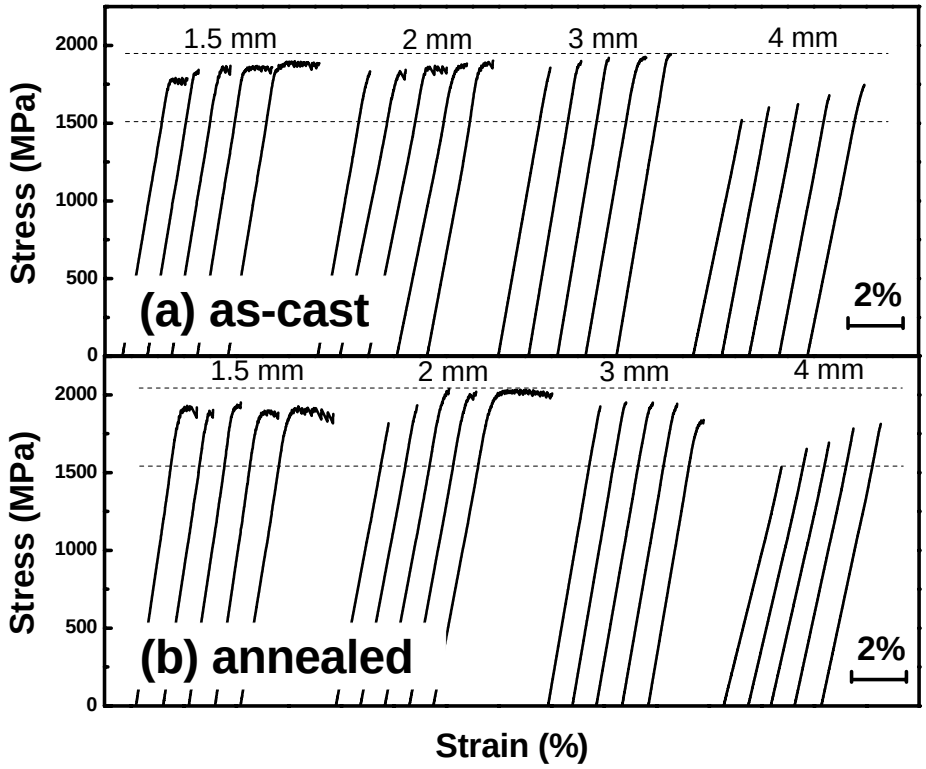

Figure 5. 2 Representative stress-strain curves of $Zr_{48}Cu_{45}Al_7$ (a) as-cast and (b) annealed samples with different sizes under compression. An evident "malleable-to-brittle" transition was observed in both states.

A distinguished sample size-dependent trend was observed on the *malleability* [202], which was generally increasing with decreasing sample size. As seen in **Figure 5. 2** (a), all of the 4 mm samples failed without any plastic strain and yet obvious yielding started to be detected at 3 mm samples and most of 1.5 mm samples exhibited certain degree of plastic strain (less than 2%) before failure. These results clearly demonstrate that there is a *"malleable-to-brittle" transition* with a critical sample size D_c at 3 mm, below which the BMG yields without premature brittle failure.

The same “malleable-to-brittle” transition has also been observed in the annealed samples (**Figure 5. 2** (b)) despite an increase in the average strength for the corresponding sized samples which was due to the reduction in the free volume concentration caused by annealing. Contrary to the annealing induced embrittlement in the literature [212-214], it is observed that there was no significant reduction in the malleability of annealed BMG samples in this work even there were substantially reduction in free volume concentration (**Figure 5. 1**). It is worthy of noting that, with much less free volume (**Table 5. 1**) the 1.5 mm annealed samples were still much malleable, as same as the as-cast samples, while the 4 mm samples remained brittle. Thus, it was concluded that the “malleable-to-brittle” transition was due to sample size difference itself rather than the free volume differences.

One possible explanation of this “sample size effect” was provided by Ashby and Greer [216]: if the sample size is large than the material’s plastic zone size, brittle fracture will overwhelm the plastic flow. For a Zr-based BMG, the plastic zone size was estimated to be around 1 mm [216], which is comparable to the present critical sample size of 3 mm. This relatively large plastic zone size (cf. 10-100 μm for Mg-based BMGs) accounts for the *macroscopic* “malleable-to-brittle” transition. The sample size effect can also be understood from the driving force perspective [217]. As an analogue to the cracking in crystalline materials by Griffith’s energy balance theory[218], the

shear band propagation has been proposed to be a competition process between the stored elastic strain energy (E_e) and the energy of forming newly created surfaces and/or shear bands (γ) [217, 219-221]. Since the E_e scales with sample volume, and γ scales with sample cross-sectional area, an equilibrium condition should be reached at a critical sample size. Note that the critical size in current work is responsible for the "malleable-to-brittle" transition (depending on whether the yielding has occurred), and should be differentiated from that of the homogeneous-to-inhomogeneous transition (depending on whether uniform deformation has occurred) as observed in metallic glass micro pillars [219] recently. The latter transition was apparently accompanied with a much smaller critical sample size.

5.3.2 Size dependence of strength

The second observed trend was in the strength of the samples. In the brittle region ($D > D_c$), the fracture strength of the samples were noticeably lower and more scattered. For example, the strength of 4 mm as-cast sample ranged from 1520 to 1750 MPa with a scattering of ±3 % about the mean value. However in the malleable region ($D \leq D_c$), the strength of BMG samples increased to a higher level with a much smaller scattering. For example, the

strength of 1.5 mm as-cast samples was around 1850MPa with a much smaller scattering of ±1.5 %. In some sense, one can assume that in the malleable region where the yielding occurs, the strength of the BMG maintains a constant like the yielding phenomenon in the crystalline alloys. This suggests a high reliability in the strength of BMGs so long as the sample size is below D_c.

In the brittle region where the samples typically fractured prematurely before yielding, the fracture of BMG can be regarded as "flaw-sensitive" (see Chapter 3) [202], where the size of the "flaw" in a homogeneous glass can be in the conventional micron range (as for a pore or inclusion), or may even be intrinsic to the glass structure on the sub-nanometre range. In an unconstrained geometry, once shear localization has begun, the shear softening nature of the glass accelerates deformation through very large strains, and ultimately, failure, particularly under tension. Any flaw in the glass volume (or on its surface) can in principle serve as a facilitator to the process of shear band nucleation event, leading to the subsequent runaway shear failure. Such strength-limiting flaws may include any stress-concentrators (i.e. voids, inclusions, surface irregularities), or possibly local fluctuations in the chemistry or density (free volume) of the glass structure itself. Generally, a smaller specimen has intrinsically a higher average strength considering that there is a lower probability of finding such a critical flaw compared to the larger one [222]. This is why the 4 mm sample has a

much lower strength than that of the 3 mm one. Weibull has proposed the following equation to quantitatively describe the size effect on the strength of brittle materials [152, 153]:

$$\frac{V_1}{V_2} = \left(\frac{\sigma_2}{\sigma_1} \right)^m \tag{5.1}$$

here, V represents the specimen volume, σ the strength and m the Weibull modulus. However, we also noticed that, the close correlation between the malleability and Weibull modulus, which was demonstrated previously in Chapter 3, has made it not trivial to verify the size effect by the Equation 5.1 since different m may be obtained for different sized BMG samples.

On the other hand, in the malleable region where yielding occurred, the strengths of BMG were more or less constant. Furthermore, the *slight* strength differences in this region can be explained by the free volume concept. A smaller sized sample associated with a corresponding higher cooling rate possesses more free volume than the larger one [210, 211]. The excess free volume enhances the flux and mobility of atoms and thus would lower the strength of BMG [112, 149]. In this regard, the smaller sized BMG specimen should be "weaker" with respect to the larger one (**Figure 5. 3**).

As a consequence, the strength of BMG exhibited a sample size dependence. When the sample size is small i.e. within the malleable region, the effect of free volume is dominant due to the fact that smaller sample contains more free volume and its deformation is less flaw-sensitive. On the

other hand, the effect of flaw sensitivity becomes dominant for larger sample, which is brittle and thus much flaw-sensitive. This explains why the strength of BMG samples did not follow a monotonically increasing trend as sample size decreased but leveled off at the critical size D_c.

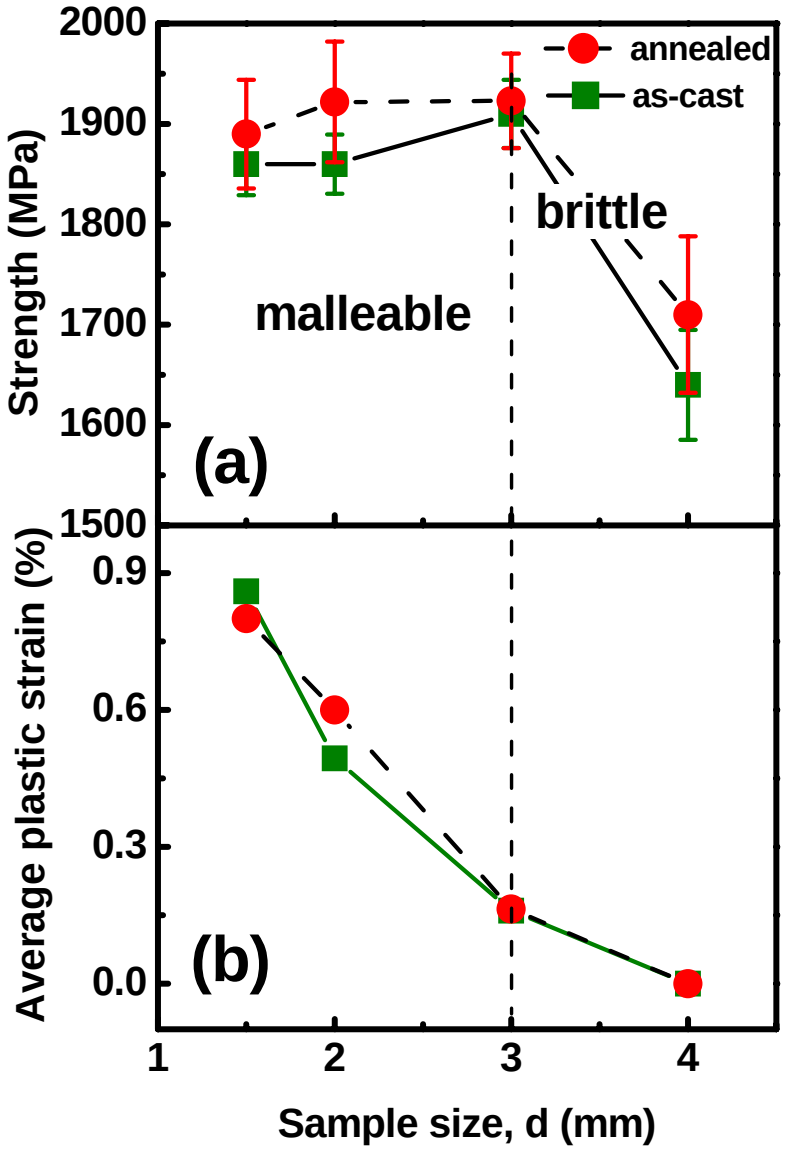

Figure 5. 3 The sample size dependence of (a) strength and (b) average plastic strain in $Zr_{48}Cu_{45}Al_7$ BMG.

5.3.3 Fractography

The above results have revealed that due to the geometrical size effect, the smaller sized BMG is more malleable than the larger one. In this section, we explore this characteristic from the fractography viewpoint.

Figure 5. 4 shows a typical fracture surface of 1.5 mm as-cast sample, where well developed vein patterns (region B) dominate the whole cross section with the remaining small area occupied by river patterns (region A), which signifie that a tensile component may have been applied at this region [182, 223]. The uniform arrangements of the veins indicate that the shear flow was initiated from the upper right corner and ended at lower left corner (i.e. from A to B).

The local melting was only observed in the lower left part of sample, which is an evidence of extensive shear deformation and believed to correspond to the final stage of shearing. The side view of fractured sample in **Figure 5. 4** (d) shows a flat fracture surface, indicates a purely shearing mode of fracture in 1.5 mm sized sample. In addition, there are several shear bands observed on the sample surface despite that the sample fractured along one dominant shear band.

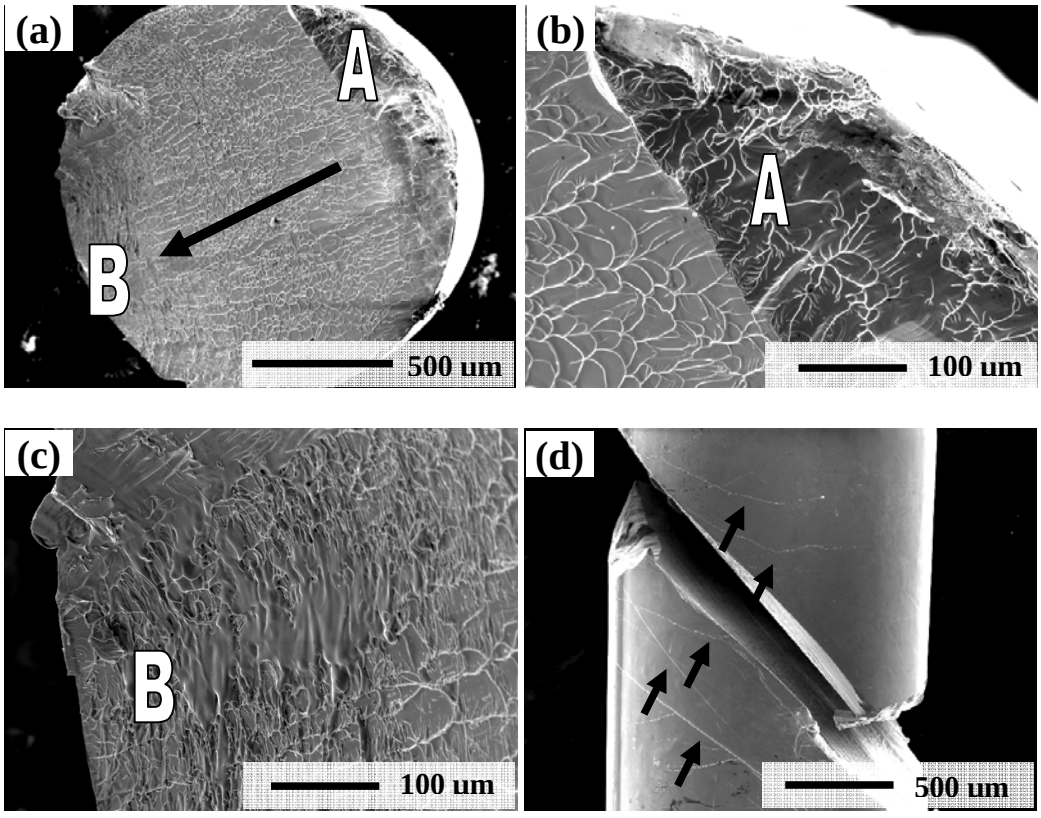

Figure 5. 4 (a) Fractography observation of 1.5 mm sized $Zr_{48}Cu_{45}Al_7$ as-cast BMG. The black arrow in (a) shows the direction of shearing deformation. Magnified views of the region A, and B indicated in (a) are shown in (b), and (c), respectively. The side view of the sample shown in (d) suggests a purely shearing mode of fracture.

In a great contrast, the fractography for 4 mm as-cast sample is much different. As seen in **Figure 5. 5** (a), in the fracture surface of 4 mm sample the vein patterns only covered about 30% of the cross section area (region A in **Figure 5. 5** (b)). The remained 70% was filled with the intermittent veins separated by steps or facets at different levels causing an extremely rough surface (region B in **Figure 5. 5** (c)). Unlike the vein patterns that are representatives of plastic deformation, these steps or facets manifest a typical

brittle mode of fracture. Therefore, the fractography study shows that in the 4 mm sample there were two mixed fracture modes (plastic & brittle), which were further confirmed by the rough side view of the fracture surface in **Figure 5. 5** (d).

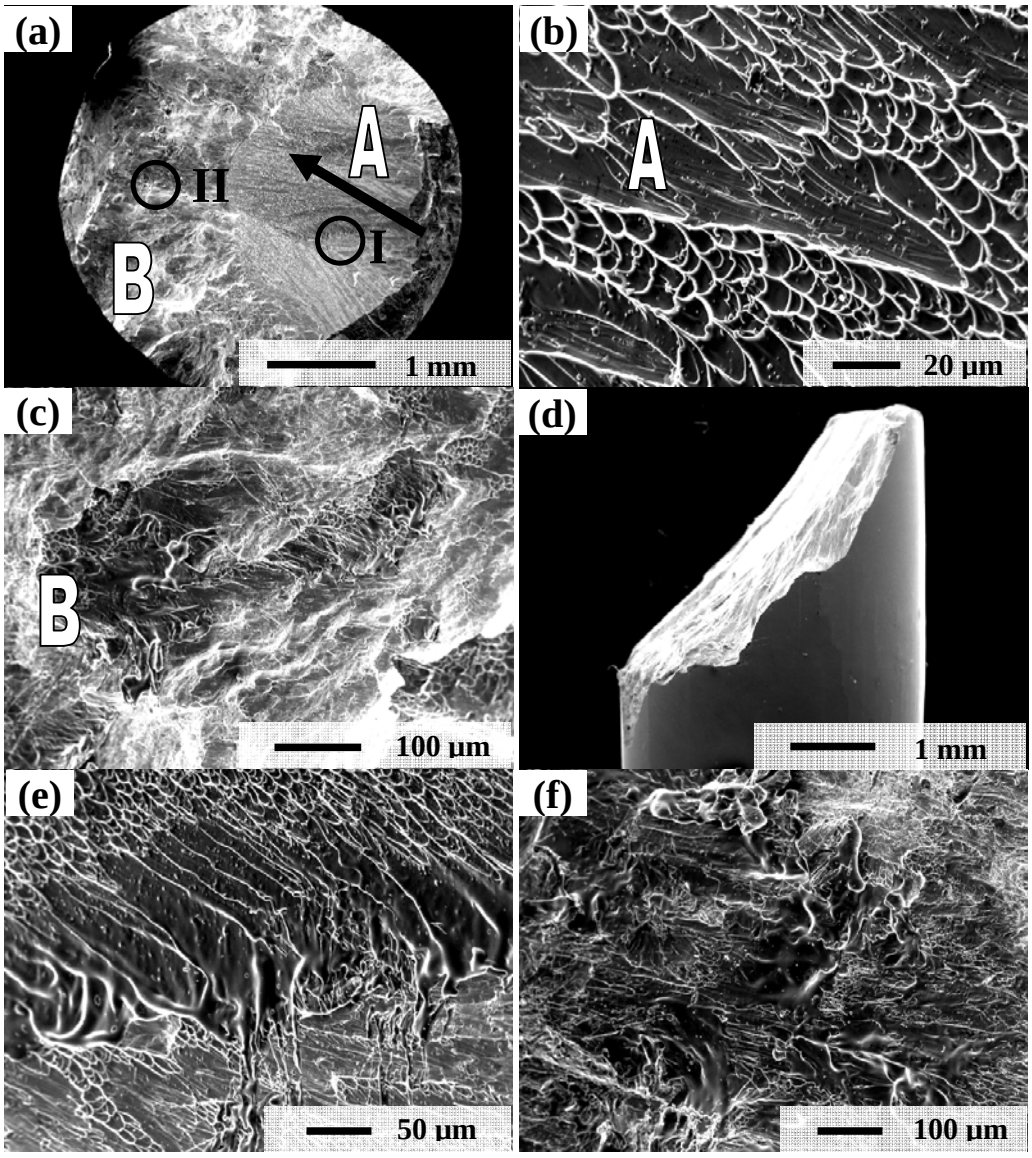

Figure 5. 5 (a) Fractography observation of 4 mm sized as-cast $Zr_{48}Cu_{45}Al_7$ BMG. The black arrow in (a) shows the shear direction. The typical morphologies in region A and B of (a) are shown in (b) and (c), respectively. The side view is shown in (d). Local melting was frequently observed in the fracture surface as circled in (a), the magnified views of circle I and II are shown in (e), and (f), respectively.

Furthermore, besides the dominant shear band associated with the final fracture, no additional shear band was observed on the 4 mm sized sample surface. Local melting has also been observed to locate in various sites. Among them two typical areas were labeled by circle I and II in **Figure 5. 5** (a) and their magnified views were shown in **Figure 5. 5** (e) and (f), respectively. These local melting seems to tend to take place at the boundaries between two shear planes (circle I) or two steps or facets (circle II). The possible reason is that, as the simultaneous instability (evidenced by many steps in the fracture surface) happens, the shearing stops suddenly at the boundary between steps and different shear planes; the heat must be released locally to accommodate the deformation.

The above results show that, there exists a sample size dependent "malleable-to-brittle" transition in the present Zr-based BMG. We further speculate that this transition might be independent of alloy system but with an individual critical size, below which *any* BMG sample is free of premature brittle failure without yielding. This critical size might vary depending on the material's intrinsic malleability. Considering the tension-compression asymmetry [180, 181, 183], this transition for BMGs might even exist under tension but with a smaller critical size.

Understanding of this "malleable-to-brittle" transition in BMGs also has some important practical implications. For example, the constant strength

in the malleable region of a BMG indicates that the material is mechanically reliable so long as the sample size is below the critical size. Such reliability is thus encouraging for the potential use of BMGs as engineering materials. What is more, most of the BMGs that are exposed to mechanical tests in the literature are in small dimensions typically below 3 mm in diameter [88, 89, 94, 203]. However, the present results offer strong evidence that the mechanical behavior of larger sized BMGs samples may not be fully represented by that derived from those smaller ones, evoking the needs for cautious consideration of the sample size effect in BMGs regarding their practical applications. Our work is consistent with a recent parallel work by Xie et al. [224] in which the sample size dependence of plasticity has been attributed to the spring-back effect from testing machine. However, we understand this size effect both in plasticity and strength differently and in our beliefs it should be a universal rule for BMGs even tested with different machines.

5.4 Conclusions

The sample size effect on the mechanical properties of a Zr-based BMG under both as-cast and annealed states has been systematically investigated. The most salient conclusions have been drawn as follows:

(1) Under both as-cast and annealed states, the $Zr_{48}Cu_{45}Al_7$ BMG exhibited a “malleable-to-brittle” transition with a critical sample size of 3 mm in diameter, below which the sample yielded with a consistent strength and above which the sample prematurely fractured in a brittle manner with decreasing strength.

(2) With minimization of the free volume effect by annealing, it was ascertained that this transition was due to the geometrical size effect rather than the free volume effect. Interestingly, it was observed that there is no significant deterioration of malleability in smaller sized BMG sample after annealing, which is in contrast to the annealing induced embrittlement phenomenon commonly reported in the literature.

(3) Accompanied with the “malleable-to-brittle” transition, the strength of BMG also showed sample size dependence, which is governed by the compromise of flaw sensitivity and free volume effects. As a result, the strength can be regarded as a constant in the malleable region, while decreased much in the brittle region. Understanding this “malleable-to-brittle” transition as well as the size-dependent strength in BMGs has important implications and guidance in the future engineering design.

Chapter 6

Concluding remarks

6.1 Summary of results

This dissertation explored the unique formation and mechanical behavior of Zr-Cu-based BMGs. The major results were summarized as follows:

(1) In contrary to the conventional belief that metallic glass is either formed near deep-eutectics through liquid quenching or near the centre of phase diagram by solid-state reaction, we discovered a completely new group of glass ("intermetallic glass") formation close to intermetallic composition in the Zr-Cu binary system through liquid

quenching. Such unique glass formation becomes feasible with both the kinetic and thermodynamic conditions for the amorphous formation being favored. The so-called "intermetallic glasses" were located in a pair and close to but separated by the intermetallic compound in the centre of the phase diagram. This finding opens an otherwise overlooked arena for finding a new host of metallic glasses (systems) that have potentials for application.

(2) Despite the fact that BMGs exhibit little or no macroscopic plasticity prior to failure (similar to other brittle materials), we observe surprisingly high uniformity in their compressive strengths. Weibull analysis was employed to study the statistical dispersion in strength, giving very high Weibull moduli of about 25 for an intrinsically brittle glass $(Zr_{48}Cu_{45}Al_7)_{98}Y_2$, and near 75 and 112 for two intrinsically malleable glass $Zr_{48}Cu_{45}Al_7$ and $Zr_{51}Cu_{49}$. This high uniformity is encouraging for the use of BMGs in structural applications. The results also showed close correlations between the Weibull modulus, malleability and GFA of as-cast Zr-Cu-based alloys.

(3) Owing to the unique shear banding event and the high strength uniformity, the brittle monolithic $(Zr_{48}Cu_{45}Al_7)_{98}Y_2$ BMG has shown enhanced compressive deformability with multiple shear bands being consistently observed by introducing stress gradient. The "stress gradient enhanced plasticity" concept was proposed using non-

orthogonal samples (e.g. monoclinic, transitional, and pyramid structures) for illustration. It was revealed that the stress gradient induced *non-uniform* deformation in BMG, affected the nucleation of new shear bands, and restricted the propagation of existing shear bands. The results suggest that by specially designing component geometry, the monolithic glassy alloys could be deformed plastically, which will alleviate the concern of catastrophic failure of BMG as an engineering material. On the other hand, the results suggested that the deformation of BMGs was highly sensitive to the sample geometry.

(4) Under both as-cast and annealed states, the $Zr_{48}Cu_{45}Al_7$ BMG exhibited a "malleable-to-brittle" transition at a critical sample size of 3 mm in diameter, below which the sample yielded with a consistent strength and above which the sample prematurely fractured in a brittle manner with decreasing strength. With minimization of the free volume effect by annealing, it was ascertained that this transition was due to the geometrical size effect rather than the free volume effect. Interestingly, it was observed that there was no significant deterioration of malleability in smaller sized BMG sample after annealing, which is in contrast to the annealing induced embrittlement commonly reported in the literature. Understanding this "malleable-to-brittle" transition as well as the size-dependent strength in BMGs has important implications and guidance in the future engineering design.

6.2 Future work

During the past decades, the research on bulk metallic glasses has been carried out extensively, and the present research has contributed several new crucial insights in the formation and mechanical behavior of BMGs. To have a more complete picture of the current research focus, the following points were raised for the future concern:

(1) The unique formation of intermetallic glass was discovered in Zr-Cu binary system in this thesis. Many more possible alloy systems with similar feature of phase diagram and/or constituent elements characteristics (e.g. heat of mixing, atomic size mismatch, etc.) should be investigated in detail. In addition, the structure, mechanical properties as well as other physical properties should be addressed systematically to have a clearer view of the new group of glass.

(2) The present study on mechanical properties of BMGs addressed three main subjects i.e. *strength variation*, *plasticity enhancement* and *sample size dependence of deformation* under compressive loading, in which only mode II fracture takes place. The same subjects under other loading modes such as tension and bending should be much more complicated as the mode I fracture intervenes. It seems possible that the results may exhibit asymmetry to some extent, but basically with similar features.

Bibliography

[1] Johnson WL. MRS Bull. 1999;24:42.

[2] Liquidmetal Technologies Home Page. http://www.liquidmetal.com (Accessed: July, 2008)

[3] Luborsky FE. Amorphous Metallic Alloys London: Butterworths, 1983.

[4] Klement W, Willens RH, Duwez P. Nature 1960;187:869.

[5] Chen HS. Acta Metall. 1974;22:1505.

[6] Inoue A, Zhang T, Masumoto T. Mater. Trans. JIM 1990;31:425.

[7] Inoue A. Acta Mater. 2000;48:279.

[8] Guo FQ, Poon SJ, Shiflet GJ. Appl. Phys. Lett. 2003;83:2575.

[9] Park ES, Kim DH. Appl. Phys. Lett. 2005;86:201912.

[10] Schroers J, Lohwongwatana B, Johnson WL, Peker A. Appl. Phys. Lett. 2005;87:061912.

[11] Zhang B, Zhao DQ, Pan MX, Wang WH, Greer AL. Phys. Rev. Lett. 2005;94:205502.

[12] Inoue A, Nishiyama N, Kimura H. Mater. Trans. JIM 1997;38:179.

[13] Drehman AJ, Greer AL, Turnbull D. Appl. Phys. Lett. 1982;41:716.

[14] Inoue A, Kato A, Zhang T, Kim SG, Masumoto T. Mater. Trans. JIM 1991;32:609.

[15] Peker A, Johnson WL. Appl. Phys. Lett. 1993;63:2342.

[16] Inoue A, Zhang T, Nishiyama N, Ohba K, Masumoto T. Mater. Trans. JIM 1993;34:1234.

[17] Lin XH, Johnson WL. J. Appl. Phys. 1995;78:6514.

[18] Inoue A, Shinohara Y, Gook JS. Mater. Trans. JIM 1995;36:1427.

[19] Inoue A, Zhang T. Mater. Sci. Eng. A 1997;226:393.

[20] Zhang T, Inoue A. Mater. Trans. JIM 1998;39:1001.

[21] Wang XM, Yoshii I, Inoue A, Kim YH, Kim IB. Mater. Trans. JIM 1999;40:1130.

[22] Inoue A, Zhang W, Zhang T, Kurosaka K. Acta Mater. 2001;49:2645.

[23] Pang SJ, Zhang T, Asami K, Inoue A. Acta Mater. 2002;50:489.

[24] Inoue A, Shen BL, Koshiba H, Kato H, Yavari AR. Nat. Mater. 2003;2:661.

[25] Xu DH, Duan G, Johnson WL, Garland C. Acta Mater. 2004;52:3493.

[26] Xu DH, Duan G, Johnson WL. Phys. Rev. Lett. 2004;92:245504.

[27] Xu DH, Lohwongwatana B, Duan G, Johnson WL, Garland C. Acta Mater. 2004;52:2621.

[28] Wang D, Li Y, Sun BB, Sui ML, Lu K, Ma E. Appl. Phys. Lett. 2004;84:4029.

[29] Tang MB, Zhao DQ, Pan MX, Wang WH. Chin. Phys. Lett. 2004;21:901.

[30] Shen J, Chen QJ, Sun JF, Fan HB, Wang G. Appl. Phys. Lett. 2005;86:151907.

[31] Ma H, Shi LL, Xu J, Li Y, Ma E. Appl. Phys. Lett. 2005;87:181915.

[32] Ponnambalam V, Poon SJ, Shiflet GJ. J. Mater. Res. 2004;19:1320.

[33] Amiya K, Inoue A. Mater. Trans. 2006;47:1615.

[34] Zeng YQ, Nishiyama N, Inoue A. Mater. Trans. 2007;48:1355.

[35] Zhang QS, Zhang W, Inoue A. Scripta Mater. 2006;55:711.

[36] Conner RD, Dandliker RB, Johnson WL. Acta Mater. 1998;46:6089.

[37] Johnson WL, Lu J, Demetriou MD. Intermetallics 2002;10:1039.

[38] Busch R, Kim YJ, Johnson WL. J. Appl. Phys. 1995;77:4039.

[39] Busch R, Liu W, Johnson WL. J. Appl. Phys. 1998;83:4134.

[40] Busch R, Schroers J, Wang WH. MRS Bull. 2007;32:620.

[41] Busch R. Jom-Journal of the Minerals Metals & Materials Society 2000;52:39.

[42] Heilmaier M, Eckert J. Jom-Journal of the Minerals Metals & Materials Society 2000;52:43.

[43] Angell CA. Science 1995;267:1924.

[44] Iida T, Guthrie RIL. The Physical Properties of Liquid Metals. Oxford: Claredon, 1988

[45] Shadowspeaker L, Busch R. Appl. Phys. Lett. 2004;85:2508.

[46] Mukherjee S, Schroers J, Johnson WL, Rhim WK. Phys. Rev. Lett. 2005;94:245501.

[47] Li Y, Jones H, Davies HA. Scripta Metall. Mater. 1992;26:1371.

[48] Boettinger W. In: Kear B, Giessen B, Cohen M, editors. Rapidly Solidified Amorphous and Crystalline Alloys,. New York: Elsevier Science Publishing, 1982. p.15.

[49] Li Y, Liu HY, Jones H. J. Mate. Sci. 1996;31:1857.

[50] Inoue A, Zhang T, Masumoto T. J. Non-Cryst. Solids 1993;156:473.

[51] Kim YJ, Busch R, Johnson WL, Rulison AJ, Rhim WK. Appl. Phys. Lett. 1994;65:2136.

[52] Li Y, Liu HY, Davies HA, Jones H. Mater. Sci. Eng. A 1994;179:628.

[53] Yokoyama Y, Inoue A. Mater. Trans. JIM 1995;36:1398.

[54] Uhlmann DR. J. Non-Cryst. Solids 1972;7:337.

[55] Turnbull D. Contemp. Phys. 1969;10:473.

[56] Chen HS. Rep. Prog. Phys. 1980;43:353.

[57] Tan H, Zhang Y, Ma D, Feng YP, Li Y. Acta Mater. 2003;51:4551.

[58] Zhang T, Inoue A, Masumoto T. Mater. Trans. JIM 1991;32:1005.

[59] Ma D, Tan H, Wang D, Li Y, Ma E. Appl. Phys. Lett. 2005;86:191906.

[60] Inoue A, Zhang T, Masumoto T. Mater. Trans. JIM 1989;30:965.

[61] Kim SG, Inoue A, Masumoto T. Mater. Trans. JIM 1990;31:929.

[62] Inoue A, Zhang T, Masumoto T. Mater. Trans. JIM 1990;31:177.

[63] Kurz W, Fisher DJ. Int. Met. Rev. 1979;5-6:177.

[64] Wang D, Tan H, Li Y. Acta Mater. 2005;53:2969.

[65] Zhang J, Tan H, Feng YP, Li Y. Scripta Mater. 2005;53:183.

[66] Spaepen F. Acta Metall. 1977;25:407.

[67] Argon AS. Acta Metall. 1979;27:47.

[68] Megusar J, Argon AS, Grant NJ. Mater. Sci. Eng. 1979;38:63.

[69] Lu J, Ravichandran G, Johnson WL. Acta Mater. 2003;51:3429.

[70] Schuh CA, Lund AC, Nieh TG. Acta Mater. 2004;52:5879.

[71] Inoue A, Nakamura T, Nishiyama N, Masumoto T. Mater. Trans. JIM 1992;33:937.

[72] Bruck HA, Christman T, Rosakis AJ, Johnson WL. Scripta Metall. Mater. 1994;30:429.

[73] Kimura H, Masumoto T. Acta Metall. 1983;31:231.

[74] Conner RD, Johnson WL, Paton NE, Nix WD. J. Appl. Phys. 2003;94:904.

[75] Jiang WH, Liu F, Qiao DC, Choo H, Liaw PK. J. Mater. Res. 2006;21:1570.

[76] Schuh CA, Hufnagel TC, Ramamurty U. Acta Mater. 2007;55:4067.

[77] Schuh CA, Nieh TG. J. Mater. Res. 2004;19:46.

[78] Lowhaphandu P, Lewandowski JJ. Scr. Mater. 1998;38:1811.

[79] Flores KM, Dauskardt RH. Scr. Mater. 1999;41:937.

[80] Bae DH, Lim HK, Kim SH, Kim DH, Kim WT. Acta Mater. 2002;50:1749.

[81] Kimura H, Masumoto T. Acta Metallurgica 1980;28:1663.

[82] Kimura H, Masumoto T. Philos. Mag. A-Phys. Condens. Matter Struct. Defect Mech. Prop. 1981;44:1021.

[83] Chiang CL, Chu JP, Lo CT, Nieh TG, Wang ZX, Wang WH. Intermetallics 2004;12:1057.

[84] Pampillo CA, Chen HS. Mater. Sci. Eng. 1974;13:181.

[85] Zhang ZF, Zhang H, Pan XF, Das J, Eckert J. Philos. Mag. Lett. 2005;85:513.

[86] Bei H, Xie S, George EP. Phys. Rev. Lett. 2006;96:105503.

[87] Schuh CA, Nieh TG. Acta Mater. 2003;51:87.

[88] Das J, Tang MB, Kim KB, Theissmann R, Baier F, Wang WH, Eckert J. Phys. Rev. Lett. 2005;94:205501.

[89] Schroers J, Johnson WL. Phys. Rev. Lett. 2004;93:255506.

[90] Lewandowski JJ, Wang WH, Greer AL. Philos. Mag. Lett. 2005;85:77.

[91] Yao KF, Ruan F, Yang YQ, Chen N. Appl. Phys. Lett. 2006;88:122106.

[92] Gu XJ, McDermott AG, Poon SJ, Shiflet GJ. Appl. Phys. Lett. 2006;88:211905.

[93] Yao KF, Zhang CQ. Appl. Phys. Lett. 2007;90:061901.

[94] Liu YH, Wang G, Wang RJ, Zhao DQ, Pan MX, Wang WH. Science 2007;315:1385.

[95] Kelly A, Tyson WR, Cottrell AH. Philos. Mag. 1967;15:567.

[96] Pugh SF. Philos. Mag. 1954;45:823.

[97] Wang WH. J. Appl. Phys. 2006;99:093506.

[98] Argon AS, Kuo HY. Materials Science and Engineering 1979;39:101.

[99] Lee ML, Li Y, Schuh CA. Acta Mater. 2004;52:4121.

[100] Argon AS, Shi LT. Acta Metallurgica 1983;31:499.

[101] Srolovitz D, Vitek V, Egami T. Acta Metallurgica 1983;31:335.

[102] Lund AC, Schuh CA. Acta Mater. 2003;51:5399.

[103] Albano F, Lacevic N, Falk ML, Glotzer SC. Mater. Sci. Eng. A 2004;375-77:671.

[104] Falk ML. Phys. Rev. B 1999;60:7062.

[105] Mayr SG. Phys. Rev. Lett. 2006;97:195501.

[106] Cohen MH, Turnbull D. J. Chem. Phys. 1959;31:1164.

[107] Duine PA, Sietsma J, Vandenbeukel A. Acta Metall. Mater. 1992;40:743.

[108] Daniel BSS, Reger-Leonhard A, Heilmaier M, Eckert J, Schultz L. Mech. Time-Depend. Mater. 2002;6:193.

[109] Wright WJ, Hufnagel TC, Nix WD. J. Appl. Phys. 2003;93:1432.

[110] Jiang WH, Fan GJ, Liu FX, Wang GY, Choo H, Liaw PK. J. Mater. Res. 2006;21:2164.

[111] Chen LY, Fu ZD, Zhang GQ, Hao XP, Jiang QK, Wang XD, Cao QP, Franz H, Liu YG, Xie HS, Zhang SL, Wang BY, Zeng YW, Jiang JZ. Phys. Rev. Lett. 2008;1:075501.

[112] Liu Y, Bei H, Liu CT, George EP. Appl. Phys. Lett. 2007;90:071909.

[113] Huang YJ, Shen J, Shun JF. Appl. Phys. Lett. 2007;90:081919.

[114] Choi-Yim H, Busch R, Koster U, Johnson WL. Acta Mater. 1999;47:2455.

[115] Choi-Yim H, Johnson WL. Appl. Phys. Lett. 1997;71:3808.

[116] Kim CP, Busch R, Masuhr A, Choi-Yim H, Johnson WL. Appl. Phys. Lett. 2001;79:1456.

[117] Xu YK, Xu J. Scripta Mater. 2003;49:843.

[118] Inoue A, Zhang T, Chen MW, Sakurai T, Saida J, Matsushita M. J. Mater. Res. 2000;15:2195.

[119] Johnson WL. Mater. Sci. Forum 1996;225:35.

[120] Leonhard A, Xing LQ, Heilmaier M, Gebert A, Eckert J, Schultz L. Nanostruct. Mater. 1998;10:805.

[121] Lee JC, Kim YC, Ahn JP, Kim HS. Acta Mater. 2005;53:129.

[122] Hays CC, Kim CP, Johnson WL. Phys. Rev. Lett. 2000;84:2901.

[123] Hofmann DC, Suh JY, Wiest A, Duan G, Lind ML, Demetriou MD, Johnson WL. Nature 2008;451:1085.

[124] Cohen MH, Turnbull D. Nature 1961;189:131.

[125] Lu ZP, Tan H, Li Y, Ng SC. Scripta Mater. 2000;42:667.

[126] Schwarz RB, Johnson WL. Phys. Rev. Lett. 1983;51:415.

[127] Yeh XL, Samwer K, Johnson WL. Appl. Phys. Lett. 1983;42:242.

[128] Koch CC, Cavin OB, McKamey CG, Scarbrough JO. Appl. Phys. Lett. 1983;43:1017.

[129] Schwarz RB, Petrich RR, Saw CK. J. Non-Cryst. Solids 1985;76:281.

[130] Carvalho EM, Harris IR. J. Mater. Sci. 1980;15:1224.

[131] Nicholls AW, Harris IR, Mangen W. J. Mater. Sci. Lett. 1986;5:217.

[132] Zhalkotitarenko AV, Yevlashina ML, Antonov VN, Yavorskii BY, Koval YN, Firstov GS. Phys. Status Solidi B-Basic Res. 1994;184:121.

[133] Li Y, Guo Q, Kalb JA, Thompson CV. to be published.

[134] Inoue A, Zhang W. Mater. Trans. 2004;45:584.

[135] Hellstern E, Schultz L. Philos. Mag. B 1987;56:443.

[136] Atzmon M, Verhoeven JD, Gibson ED, Johnson WL. Appl. Phys. Lett. 1984;45:1052.

[137] Takeuchi A, Inoue A. Mater. Trans. 2005;46:2817.

[138] Bernal JD. Nature 1960;185:68.

[139] Miracle DB. Nat. Mater. 2004;3:697.

[140] Schultz L. J. Less-Common Met. 1988;145:233.

[141] Sun YF, Wei BC, Wang YR, Li WH, Cheung TL, Shek CH. Appl. Phys. Lett. 2005;87:051905.

[142] Inoue A, Zhang W, Tsurui T, Yavari AR, Greer AL. Phil. Mag. Lett. 2005;85:221.

[143] Zhu ZW, Zhang HF, Sun WS, Ding BZ, Hu ZQ. Scripta Mater. 2006;54:1145.

[144] Greer AL. Nature 1993;366:303.

[145] Das J, Pauly S, Duhamel C, Wei BC, Eckert J. J. Mater. Res. 2007;22:326.

[146] Jiang F, Zhang ZB, He L, Sun J, Zhang H, Zhang ZF. J. Mater. Res. 2006;21:2638.

[147] Zhang QS, Zhang W, Xie GQ, Nakayama KS, Kimura H, Inoue A. J. Alloys Compd. 2007;431:236.

[148] Hofmann DC, Duan G, Johnson WL. Scr. Mater. 2006;54:1117.

[149] Steif PS, Spaepen F, Hutchinson JW. Acta Metall. 1982;30:447.

[150] Tang CG, Li Y, Zeng KY. Mater. Sci. Eng. A 2004;384:215.

[151] Bhowmick R, Raghavan R, Chattopadhyay K, Ramamurty U. Acta Mater. 2006;54:4221.

[152] Weibull W. J. Appl. Mech. 1951;18:293.

[153] Weibull W. Appl. Mech. Rev. 1952;5:449.

[154] Ocelik V, Bengus VZ, Diko P, Hudak O. J. Mate. Sci. Lett. 1987;6:1333.

[155] Calvo M. J. Mate. Sci. 1989;24:1801.

[156] Ocelik V, Bengus VZ, Korolkova EB, Tabachnikova ED, Csach K, Duhaj P. J. Mate. Sci. Lett. 1990;9:529.

[157] Ocelik V, Bengus VZ, Korolkova EB, Csach K, Miskuf J, Duhaj P. J. Mater. Sci. 1991;26:6699.

[158] Khalili A, Kromp K. J. Mater. Sci. 1991;26:6741.

[159] Sullivan JD, Lauzon PH. J. Mater. Sci. 1985;5:1245.

[160] Trustrum K, Jayatilaka AD. J. Mater. Sci. 1979;14:1080.

[161] Bergman B. J. Mater. Sci. Lett. 1984;3:689.

[162] Askeland DR. Science and Engineering of Materials. Boston: PWS Publishing, 1994.

[163] Griffiths WD, Cox M, Campbell J, Scholl G. Materials Science and Technology 2007;23:137.

[164] Ashby MF, Jones RH. Engineering materials 2: An introduction to microstructures, processing and design. Oxford, U.K.: Butterworth-Heinemann, 1998.

[165] Biery N, De Graef M, Beuth J, Raban R, Elliott A, Austin C, Pollock TM. Metallurgical and Materials Transactions a-Physical Metallurgy and Materials Science 2002;33:3127.

[166] Zhao YY, Ma E, Xu J. Scripta Mater. 2008;58:496.

[167] Yao JH, Wang JQ, Lu L, Li Y. Appl. Phys. Lett. 2008;92:041905.

[168] Lee CJ, Huang JC, Nieh TG. Appl. Phys. Lett. 2007;91:161913.

[169] Bao YW, Zhou YC, Zhang HB. J. Mate. Sci. 2007;42:4470.

[170] Tjandrawinata R, Irie M, Suzuki K. Dental Materials Journal 2007;26:589.

[171] McDowell GR, Bolton MD, Robertson D. Journal of the Mechanics and Physics of Solids 1996;44:2079.

[172] Zafeiropoulos NE, Baillie CA. Composites Part a-Applied Science and Manufacturing 2007;38:629.

[173] Takei M, Kusakabe O, Hayashi T. Soils and Foundations 2001;41:97.

[174] McDowell GR, Bolton MD. Geotechnique 1998;48:667.

[175] Lobo-Guerrero S, Vallejo LE. Journal of Geotechnical and Geoenvironmental Engineering 2006;132:786.

[176] Lim WL, McDowell GR, Collop AC. Granular Matter 2004;6:229.

[177] Pugno NM, Ruoff RS. J. Appl. Phys. 2006;99:024301.

[178] McDowell GR. Soils and Foundations 2002;42:139.

[179] McDowell GR, Humphreys A. Granular Matter 2002;4:1.

[180] Schuh CA, Lund AC. Nat. Mater. 2003;2:449.

[181] Zhang ZF, He G, Eckert J, Schultz L. Phys. Rev. Lett. 2003;91:045505.

[182] Zhang ZF, Eckert J, Schultz L. Acta Mater. 2003;51:1167.

[183] Lewandowski JJ, Lowhaphandu P. Phil. Mag. A 2002;82:3427.

[184] Xi XK, Zhao DQ, Pan MX, Wang WH, Wu Y, Lewandowski JJ. Phys. Rev. Lett. 2005;94:125510.

[185] Poon SJ, Shiflet GJ, Ponnambalam V, Keppens VM, Taylor R, Petculescu G. Synthesis and properties of high-manganese iron-based bulk amorphous metals as non-ferromagnetic amorphous steel alloys. In: Egami T, Greer AL, Inoue A, Ranganathan S, editors. Supercooled Liquids, Glass Transition and Bulk Metallic Glasses, vol. 754. 2003. p.167.

[186] Greer AL. Science 1995;267:1947.

[187] Fan C, Inoue A. Appl. Phys. Lett. 2000;77:46.

[188] Szuecs F, Kim CP, Johnson WL. Acta Mater. 2001;49:1507.

[189] Kuhn U, Eckert J, Mattern N, Schultz L. Appl. Phys. Lett. 2002;80:2478.

[190] Fan C, Ott RT, Hufnagel TC. Appl. Phys. Lett. 2002;81:1020.

[191] Bian Z, Pan MX, Zhang Y, Wang WH. Appl. Phys. Lett. 2002;81:4739.

[192] Ma H, Xu J, Ma E. Appl. Phys. Lett. 2003;83:2793.

[193] Lee JC, Kim YC, Ahn JP, Kim HS, Lee SH, Lee BJ. Acta Mater. 2004;52:1525.

[194] Sun GY, Chen G, Liu CT, Chen GL. Scripta Mater. 2006;55:375.

[195] Hui X, Dong W, Chen GL, Yao KF. Acta Mater. 2007;55:907.

[196] Lu J, Ravichandran G. J. Mater. Res. 2003;18:2039.

[197] Nieh TG, Schuh C, Wadsworth J, Li Y. Intermetallics 2002;10:1177.

[198] Anand L, Su C. J. Mech. Phys. Solids 2005;53:1362.

[199] Thamburaja P, Ekambaram R. J. Mech. Phys. Solids 2007;55:1236.

[200] Yang Q, Mota A, Ortiz M. Comput. Mech. 2006;37:194.

[201] Gao YF. Modelling Simul. Mater. Sci. Eng. 2006;14:1329.

[202] Wu WF, Li Y, Schuh CA. Philos. Mag. 2008;88:71.

[203] Zhang Y, Wang WH, Greer AL. Nat. Mater. 2006;5:857.

[204] Conner RD, Li Y, Nix WD, Johnson WL. Acta Mater. 2004;52:2429.

[205] Sergueeva AV, Mara NA, Kuntz JD, Lavernia EJ, Mukherjee AK. Philos. Mag. 2005;85:2671.

[206] Choi-Yim H, Conner RD, Szuecs F, Johnson WL. Acta Mater. 2002;50:2737.

[207] Wada T, Inoue A, Greer AL. Appl. Phys. Lett. 2005;86:251907.

[208] Lewandowski JJ, Gu XJ, Nouri AS, Poon SJ, Shiflet GJ. Appl. Phys. Lett. 2008;92:091918.

[209] Greer AL. Structural Relaxation and Atomic Transport in Amorphous Alloys. In: Liebermann HH, editor. Rapidly solidified alloys : processes, structures, properties, applications. New York: M. Dekker, 1993. p.272.

[210] Spaepen F. Scr. Mater. 2006;54:363.

[211] Jiang WH, Liu FX, Wang YD, Zhang HF, Choo H, Liaw PK. Mater. Sci. Eng. A 2006;430:350.

[212] Mulder AL, Vanderzwaag S, Vandenbeukel A. Scripta Metallurgica 1983;17:1399.

[213] Niikura A, Tsai AP, Inoue A, Masumoto T. J. Non-Cryst. Solids 1993;159:229.

[214] Ramamurty U, Lee ML, Basu J, Li Y. Scr. Mater. 2002;47:107.

[215] Slipenyuk A, Eckert J. Scr. Mater. 2004;50:39.

[216] Ashby MF, Greer AL. Scr. Mater. 2006;54:321.

[217] Guo H, Yan PF, Wang YB, Tan J, Zhang ZF, Sui ML, Ma E. Nat. Mater. 2007;6:735.

[218] Griffith AA. Philos. Trans. R. Soc. 1920;Ser. A 221:163.

[219] Volkert CA, Donohue A, Spaepen F. J. Appl. Phys. 2008;103:083539.

[220] Zhang ZF, Zhang H, Shen BL, Inoue A, Eckert J. Philos. Mag. Lett. 2006;86:643.

[221] Zheng Q, Cheng S, Strader JH, Ma E, Xu J. Scr. Mater. 2007;56:161.

[222] Lawn BR. Fracture of brittle solids. Cambridge: Cambridge University Press, 1993.

[223] Spaepen F. Acta Metall. 1975;23:615.

[224] Xie S, George EP. Intermetallics 2008;16:485.